A New Approach to 3-Dimensional Super-Resolution Microscopy

Marco David Howard

A dissertation
submitted in partial fulfillment of the
requirements for the degree of

Doctor of Philosophy

University of Washington
Year 2019

Reading Committee:
Joshua Vaughan, Chair
Daniel Chiu
Bruce Robinson

Program Authorized to Offer Degree:
Chemistry

University of Washington

Abstract

A New Approach to 3-Dimensional Super-Resolution Microscopy

Marco Howard

Chair of the Supervisory Committee:
Assistant Professor of Chemistry Joshua Vaughan
Department of Chemistry

Super-Resolution microscopy has transformed our ability to image biological specimens at the nanoscale with high contrast and molecular specificity. However, acquiring 3-dimensional images over large volumes remains a challenge because the imaging process causes fluorophores outside the focal volume to photobleach before they can be imaged. Additionally, acquiring highly multiplexed images is challenging due to a lack of spectrally distinct fluorophores which possess the required photophysical properties for super-resolution imaging.

Here I present my work which specifically addresses these issues. In chapter 2 I first discuss the importance of sample preparation for super-resolution imaging. In chapter 3 I introduce a novel labeling scheme called probe-refresh STORM (prSTORM) which enables practitioners obtain multiplexed, extended-depth super-resolution images with a single dye, and in chapter 4 I show the importance of hardware for super-resolution microscopy.

TABLE OF CONTENTS

List of Figures v

List of Tables vii

Chapter 1. Introduction 12

1.1 A Brief Overview 12

1.2 Fluorescence Microscopy and the Diffraction Limit 13

1.3 Diffraction-Limited Fluorescence Microscopy 16

1.4 Structured Illumination Microscopy (SIM) 18

1.5 Stimulated emission depletion microscopy (STED) 19

1.6 Single Molecule Localization Microscopy (SMLM) 22

1.7 Use of fluorescent proteins in SMLM: 24

1.8 Use of organic fluorophores for SMLM 25

1.9 Challenges for organic fluorophores 27

1.10 Use of DNA Conjugated Fluorophores for SMLM 28

1.11 Summary 29

1.12 References 30

Chapter 2. ‘Point by point’: An introductory Guide to Sample Preparation for Single-Molecule Super-Resolution Fluorescence Microscopy 35

2.1 Preface 35

2.2 Abstract 36

2.3 Introduction 36

2.4 Strategic Planning 39

2.5 Protocol: Immunostaining of Cultured Cells 42

2.5.1 Seeding Cells and Coverglass Chamber 45

2.5.2 Extraction 45

2.5.3 Fixation 45

2.5.4 Immunostaining 46

2.5.5 Postfixation and Storage 47

2.6 Support Protocol 1: Secondary Antibody Labeling with NHS Fluorophores 47

2.6.1 Labeling Reaction 48

2.6.2 Dye Purification and ratio determination 49

2.7 Support Protocol 2: Thiol Imaging Cocktail for Alexa Fluor 647/Cy5/Cy3B/Atto 488 50

2.7.1 Oxygen Scavenger stock solution (GLOX) preparation 51

2.7.2 Imaging Cocktail 51

2.7.3 Imaging Conditions 52

2.7.4 Storage 52

2.8 Support Protocol 3: TCEP Imaging Cocktail for Alexa 750/Cy7 52

2.8.1 Imaging Cocktail 53

2.8.2 TCEP Addition 53

2.8.3 Imaging Conditions 54

2.9 Commentary 58

2.9.1 Background info 58

2.9.2 Critical Parameters 60

2.9.3 Troubleshooting 65

2.9.4 Anticipated Results 65

2.9.5 Time Considerations 67

2.10 References 68

Chapter 3. Extended-Depth 3D Super-Resolution Imaging using probe-Refresh storm 71

3.1 Preface 71

3.2 Abstract 73

3.3 Introduction 74

3.4 Results 76

3.5 Discussion 82

3.6 Conclusion 86

3.7 Author Contributions 86

3.8 Acknowledgments 86

3.9 Supporting Citations 87

3.10 Supporting Information Materials And Methods 87

3.10.1 Reagents 87

3.10.2 Secondary Antibody Conjugation to Alexa Fluor 647 for standard immunohistochemistry (no DNA) 89

3.10.3 Preparation of DNA-Antibody Conjugates 89

3.10.4 Cell Culture and Transfection 94

3.10.5 Cell Fixation 94
3.10.6 Immunostaining 95
3.10.7 STORM setup and imaging 95
3.10.8 Data Analysis 96
3.10.9 Supporting References 97
3.10.10 Supporting Figures And Tables 99
3.11 References 107
Chapter 4. Hardware for Microscopy 111
4.1 Preface 111
4.2 Total Internal Reflection Microscopy (TIRFM) 112
4.2.1 Principles of TIRFM 112
4.2.2 Construction of a TIRF Microscope 115
4.2.3 Use of TIR for Observing Single-Molecule Redox Events 120
4.3 Confocal Microscopy 122
4.3.1 Introduction to Confocal Microscopy 122
4.3.2 Principles of SDCM 125
4.3.3 Home-Built SDCM Characterization 128
4.3.4 Disc Design 130
4.3.5 Measurement of Confocal PSF Size 130
4.3.6 Future Outlook 132
4.4 References 133

LIST OF FIGURES

Figure 1.1 14
Figure 1.2 15
Figure 1.3 16
Figure 1.4 17
Figure 1.5. 19
Figure 1.6. 21
Figure 1.7. 22
Figure 1.8 23
Figure 1.9 27
Figure 2.1. 38
Figure 2.2 40
Figure 2.3. 57
Figure 2.4 58
Figure 3.1 77
Figure 3.2 80
Figure 3.3 82
Figure 3.4. 85
Figure 3.5 101
Figure 3.6 102
Figure 3.7 103
Figure 3.8 104
Figure 3.9. 105
Figure 3.10. 106
Figure 4.1 115
Figure 4.2 116
Figure 4.3 118

Figure 4.4 119
Figure 4.5 121
Figure 4.6 124
Figure 4.7 129
Figure 4.8 132

LIST OF TABLES

Table 2-1 65
Table 3-1 DNA Sequences... 99
Table 3-2 Summary of sample preparation and imaging conditions. 100

ACKNOWLEDGEMENTS

I moved to the United States from Ecuador with big dreams, and a big goal of going to college. Now I have accomplished this by receiving a PhD in Chemistry from the University of Washington. I started my journey working in Ohio's strawberry fields. Next, I joined the United States Air Force (USAF), and finally I utilized my G.I. Bill to attend the University of Texas at Austin. I would like to take a moment to express my gratitude to some special people who have left an indelible mark on my life. Obtaining my PhD is the single most challenging thing I have ever done, filled with both highs and lows, and it would not have been possible without you.

First and foremost, this would not have been possible without the support of my mentor Joshua Vaughan, who is an extremely accomplished and intelligent scholar. My time in his lab opened my eyes two a whole new world inside of cells. I used to think biology was a boring subject filled with rote memorization, and now I understand that it truly is beautiful and marvelous. I was hooked the first day we stained some cells and placed them on the microscope stage. I had never seen anything quite like it! The nanoscopic world was alien, marvelous, complicated, highly organized, and very aesthetically pleasing. My time in his lab introduced me to a whole new perspective and way of seeing the world, and my time here will stay with me forever. Josh, thank you for giving me the opportunity to do something truly unique.

I also would like give a special thanks to Lauren Gagnon. She was my lab-partner and co-author on my main publication, and I definitely could not have done it without her. I came into the lab having performed a very limited number of wet lab experiments. She was very patient with me, taught me how to properly set up and maintain a lab-bench, and is responsible for teaching me virtually everything in the wet lab. I have the dexterity of Edward Scissor Hands, and many of our experiments required very dexterous pipetting. Thankfully, I had Lauren to come to the rescue and save me from my clumsiness. Lauren, thank you for sharing this experience with me, and you are the best coworker anyone could ever ask for!

I'd also like to acknowledge Dan Ying Lin, a visiting optical engineer from China. She played an indispensable role analyzing data, and showing me how to write code for Fourier based image registration. But perhaps most importantly, she taught me to just "be happy". I also really enjoyed the cultural exchange and the opportunity to learn about China. Dan Ying, I'll never forget eating chicken feet dim sum with you, and thank you for sharing your culture and science with me.

No dissertation from the Vaughan Lab would be complete without a super special thanks to Aaron Halpern. He is indispensable for the day-to-day operation of the lab, and always available to help and answer questions. One of the best parts of my experience at UW was working on a spinning disc confocal microscope he designed. While working with him, I learned more about the principles of microscopy and free-space optics than I ever thought possible. Aaron, thanks for teaching me so much, and always taking the time to answer my questions.

I'd also like to give a special thanks to Bruce Robinson. I took his LabView class when I first came to UW, and initially found it very frustrating. Now that several years have passed, I know this was among my most valuable experiences at UW. It exposed me to a whole new way of thinking about the world, and caused me to stand in awe of the Fourier transform. It truly is the gift that never stops giving, and I will marvel at it forever. Now I have the privilege of helping him teach this class, and I can confidently say it is one of the highlights of my time at UW. Furthermore, getting to know him as a person has been remarkable. Bruce, you the most humble, intelligent, caring, patient, and compassionate person I have ever met. You inspire me, and when I grow up, I want to be just like you.

I'd also like to extend my gratitude to the current and former members of the Vaughn group: Min Yen Lee, Honlin Lee, Heyon-Jin Kim, Sarah Parkhurst, Marcus Woodworth, Ethan Vo, Jonathan Perr, Leonard Shin, Zachariah Fincher, and Chenyi Mao. You guys have created one of the best work environments I could hope for and I am going to miss you. I also want to extend my thanks to the lab of Dr. Bo Zhang. It was a pleasure working with Yunshan Fan, Rui Hao, and Jin Lu to optically detect single redox events. It also has been a joy getting to know the younger members of the lab, Milomir Suvira and Zhuoyu Peng. Best of luck guys!

To Joe, Bernard, and Tausif: Thank you guys for being the best friends I've ever had. House music makes my heart beat and I can't think of a better squad of people to share that with. I hope we have many more late nights at the Monkey Loft and continue to host our Way Out Sound events.

My big brother Matthew is one of the best chefs I have ever met. Thank you so much for always inviting me over and feeding me, and letting me play with your boys. It has been an enormous pleasure to be part of their lives, and it brings me a ton of joy to play video games with them. Thank you, and I love you and your family to pieces.

Mom and Dad, I could never possibly express the depth my gratitude to you. You guys adopted me off the street in Ecuador, and loved me as your own. None of this would have been possible if it were not for your giant hearts and your love. I literally owe you guys everything, and I love you more than I can possibly express.

Last, but certainly not least I’d like to thank my housemate Ian Bryan. Ian, you are one of my best friends and you are like family to me. You are a joy to live with and we really make a great team! Thank you so much for putting up with me, for doing my dishes sometimes, and for tolerating my occasional messiness.

DEDICATION

This thesis is dedicated to John Digweed. Your music is the soundtrack to my life.

Chapter 1. INTRODUCTION

1.1 A BRIEF OVERVIEW

Cells are very beautiful, complex, and mysterious. Their nano-scale organization is visually stunning, and they are marvelously organized across many different length scales. For example, a single cell is bustling with activity as DNA is transcribed to RNA, which is then used to synthesize proteins, which are the functional basis of the cell (1)~~(1)~~. Sometimes cells can specialize their function and group together in interesting ways to form organs which all function in concert to give way to the mystery of complex life. In order to unravel this mystery, tools are needed that can study biological systems across length scales ranging from meters all the way down to nano-meters.

In theory, the answer to these questions is quite simple, and as Nobel laurate Richard Feynman said, “You just look at the thing” (2). In practice, however, this can be quite challenging because cells are densely packed and organized at the nanoscale, and traditional fluorescence microscopy techniques are limited by the diffraction of light which obscures a wealth of information. While <10 nm resolution can be achieved by electron microscopy and atomic force microscopy,(3–5) these techniques lack the high contrast and specificity necessary to understand the relationships between individual molecules. This thesis addresses next-generation super-resolution microscopy techniques which now permit researchers to study biological systems with molecular specificity at resolutions < 250 nm (6–13). In particular, a special emphasis is put on developments in single molecule localization microscopy (SMLM).

Additionally, this thesis gives a glimpse into the use of SMLM to observe individual redox events at the single molecule level to give fundamental electro-chemical insight.

1.2 FLUORESCENCE MICROSCOPY AND THE DIFFRACTION LIMIT

Traditional Fluorescence microscopy techniques are fundamentally limited because light emitted by a point cannot be focused down to an infinitesimally small spot. This occurs because light passing through an aperture diffracts and interferes with itself, forming an image of an Airy Disc-which is known as the point spread function (PSF). In other words, the PSF is the optical system's response to a point-source emitter(14) (**Figure 1.1**), which means it can be calculated by taking the Fourier transform of the aperture function.

$$PSF(x,y) = A \iint_{\infty}^{\infty} P(f_x, f_y) e^{-i2\pi(f_x x, + f_y y)} dxdy \qquad \text{Eq. 1.1}$$

Where $P(f_x, f_y)$ represents the circular aperture of the objective, whose radius is given by NA/λ (14, 15). NA represents the numerical aperture of the lens, and λ is the wavelength of light. Finally, The spatial frequencies in the x and y directions are given by f_x, and f_y respectively(14, 15). From this perspective, as the aperture grows larger it captures more spatial frequencies, which shrinks the size of the central spot proportionally (**Figure 1.2**). The resolution of the microscope is the closest distance at which two point emitters can be distinguished. This idea was first put forth by Abbe(16), and later refined by Rayleigh(17). Therefore, if two point emitters are located side-by-side, how easily they can be distinguished is determined by how narrow the central spot is. Rayleigh said that two points are distinguishable if the maxima of one point is at the first minimum of the Airy pattern, according to (17):

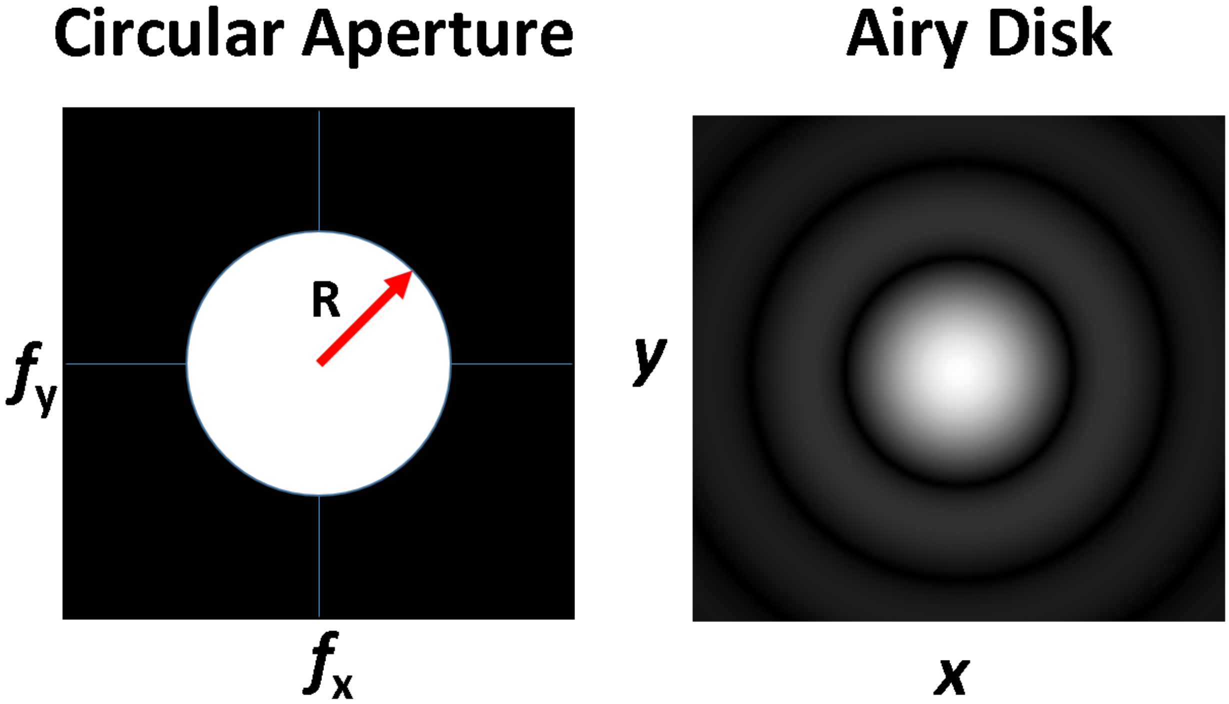

Figure 1.1 Circular aperture, of radius $R = NA/\lambda$ (left), and the magnitude of its Fourier transform (right) which is an Airy Disc

$$Resolution_{x,y} = 0.61\frac{\lambda}{NA} \qquad \text{Eq. 1.2}$$

where λ is the wavelength and NA is the numerical aperture of the lens.(16) This equation is known as the Rayleigh criterion. By inspection, one can see the resolution could be improved by increasing the NA. For example, The NA can increased to be > 1 by immersing the objective in oil which has a high index of refraction. However, the NA cannot increase infinitely because it is not possible to manufacture a perfect lens. Excellent resolution can also be obtained if the wavelength of light used is very short. However, the energy content of these waves is so high, it makes it impossible to study living organisms without killing them. On the other hand, epi-fluorescence, and confocal microscopy are work-horse tools in biology because they can relatively non-invasively probe biological specimens by labeling specific molecules with little to no background signal.

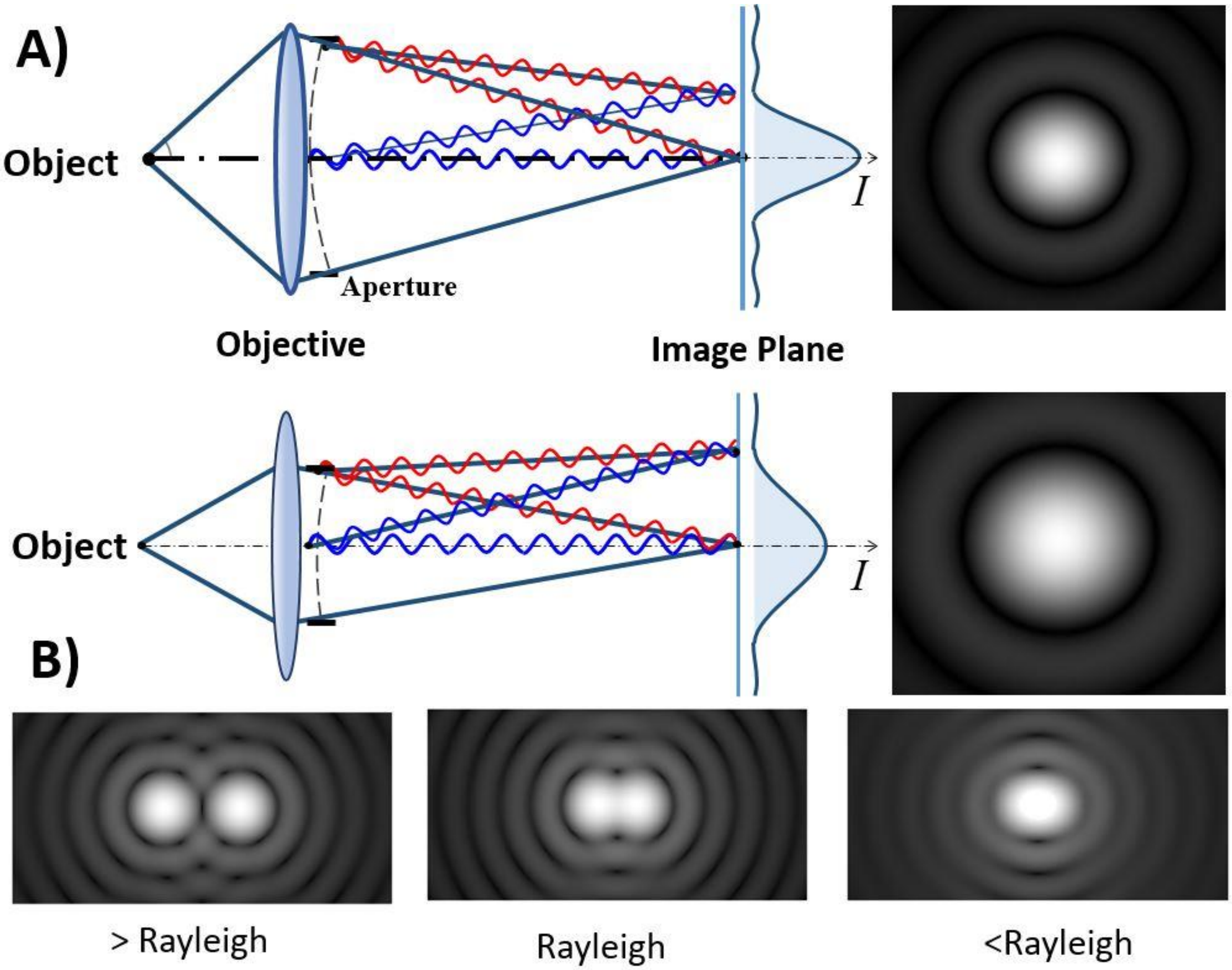

Figure 1.2 A (left) Light emitted from an object passes through an objective lens and is focused onto a plane with intensity distribution *I*. In the top figure the objective has a large aperture, compared to the bottom figure which has a smaller aperture. The intensity distribution at the focal plane is narrow for the large aperture and broad for the small aperture**. A** (right) Calculated 2D images of an airy disc corresponding to a large (top) and small (bottom) aperture.**B)** Calculated pair of airy functions at different spacing to demonstrate the idea of resolution **B** (left) When the peak of one point emitter placed far away from its neighbor, the two points are easily distinguished. **B Center)** When one point is placed at the first minimum of the airy pattern the Rayleigh criteria is met and this is the limit of resolution. **B Right)** when two points are placed closer than the center image, they become indistinguishable and are not resolved

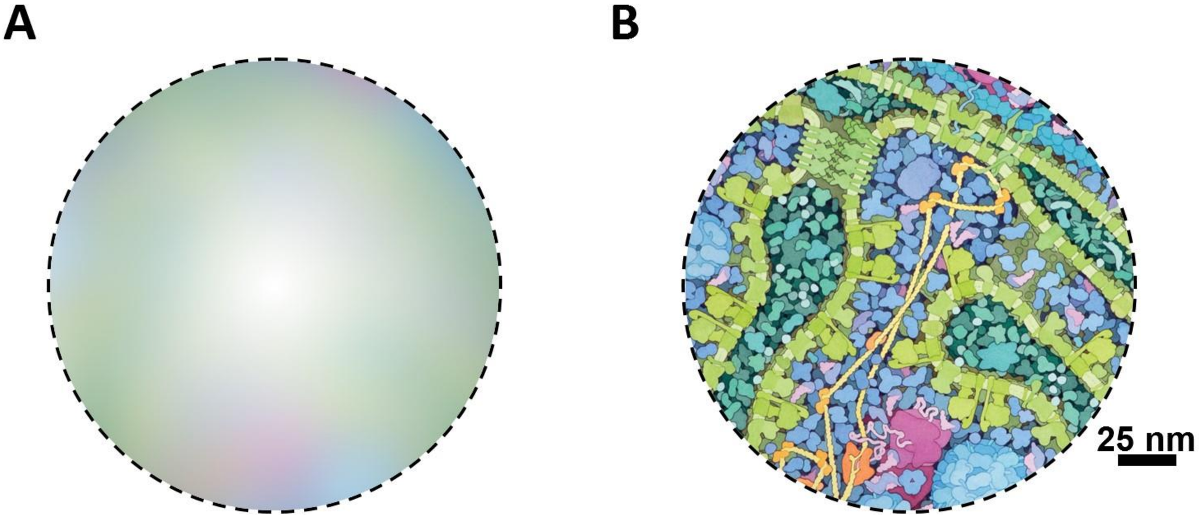

Figure 1.3 Artistic rendition of diffraction limited mitochondrial region using standard fluorescence techniques. Here the diffraction of light obscures the fine details. Once the diffraction limit is broken, one can observe the green mitochondrial membrane, with green embedded electron-transport chain proteins in green. The orange and yellow molecules are DNA/DNA associated proteins, and the pink molecules are ribosomes. (Figure adapted from Goodsell, D.S. 2010)

These techniques are limited to a resolution >250 nm because of the objective lenses and wavelengths used—making it impossible to observe the fine detail of the cell (**Figure 1.3)** (18). Consequently, there has been significant motivation to develop optical microscopy methods that can surpass the diffraction limit, while maintaining the ability to study biological systems with high contrast and molecular specificity.

1.3 DIFFRACTION-LIMITED FLUORESCENCE MICROSCOPY

In a standard diffraction-limited fluorescence microscopy experiment, a specimen is densely labeled with fluorophores. A laser beam illuminates the specimen, causing the fluorophores to be excited into their first excited state (S_1) from the ground state (S_0) **(Figure 1.4A)**. Then a large fraction a large fraction of the excited fluorophores emit a photons as they decay back down to the ground state. These photons are collected by an objective lens and are focused onto a detector, forming an image **(Figure 1.4B, C)**.

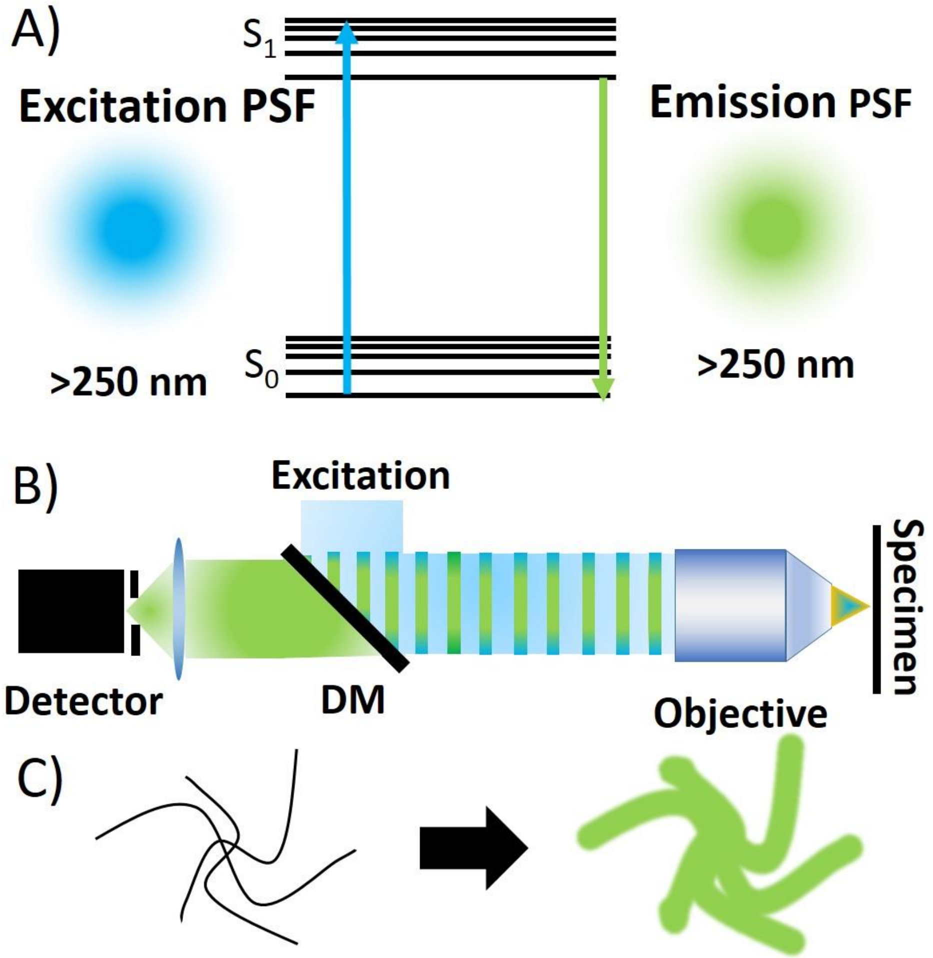

Figure 1.4 Jablonski showing a fluorophore in its ground state S_0 getting promoted to its first excited state, S_1 , via excitation with a blue laser focused down to a spot ~250 nm in size. The emission of the fluorophore is red-shifted as it decays back down to the ground state S_0, which also is detected with a PSF of >250 nm

Schematic of a confocal fluorescence microscope. A dichroic mirror (DC) is inserted into the beam path filtering out the excitation light- allowing only emitted light to reach the detector. A pinhole is placed conjugate to the sample plane to reduce background fluorescence from reaching the detector.

The ground truth structure (left) is blurred by the diffraction of light, and produces a fuzzy image (right).

1.4 STRUCTURED ILLUMINATION MICROSCOPY (SIM)

Structured Illumination microscopy is a technique that illuminates the specimen with a high spatial frequency striped pattern which creates sidebands of a lower frequency that can be analyzed to reconstruct a high-resolution image. In a common SIM implementation, a diffraction grating is used to generate a high spatial frequency pattern, at the limit of what the objective can detect (**Figure 1.5A)**. When this pattern is used to illuminate the specimen, high spatial frequency information beyond the diffraction limit becomes encoded in lower frequency interference patterns called Moiré fringes which can be detected through the objective lens. The patterned light is rotated through several angles and phases collecting a series of images, each with high frequency information encoded in the lower frequency Moiré fringes (**Figure 1.5B)**. The collected images are computationally analyzed in order to extract the high frequency information – resulting in approximately a 2-fold increase in resolution compared to conventional microscopy (**Figure 1.5C)** (7). In less common implementations, non-linear optical effects can be exploited to achieve resolutions as >50 nm via SIM (19). While common implementations of SIM do not achieve as high a resolution as STED or SMLM, it can be quite advantageous for studying live cells. This is because SIM can achieve relatively fast acquisitions, with a lower light dose compared to other techniques—reducing artifacts due to photo-toxicity. Additionally, unlike SMLM and STED, it does not depend on special properties of the fluorophore, making spectral multiplexing much easier.

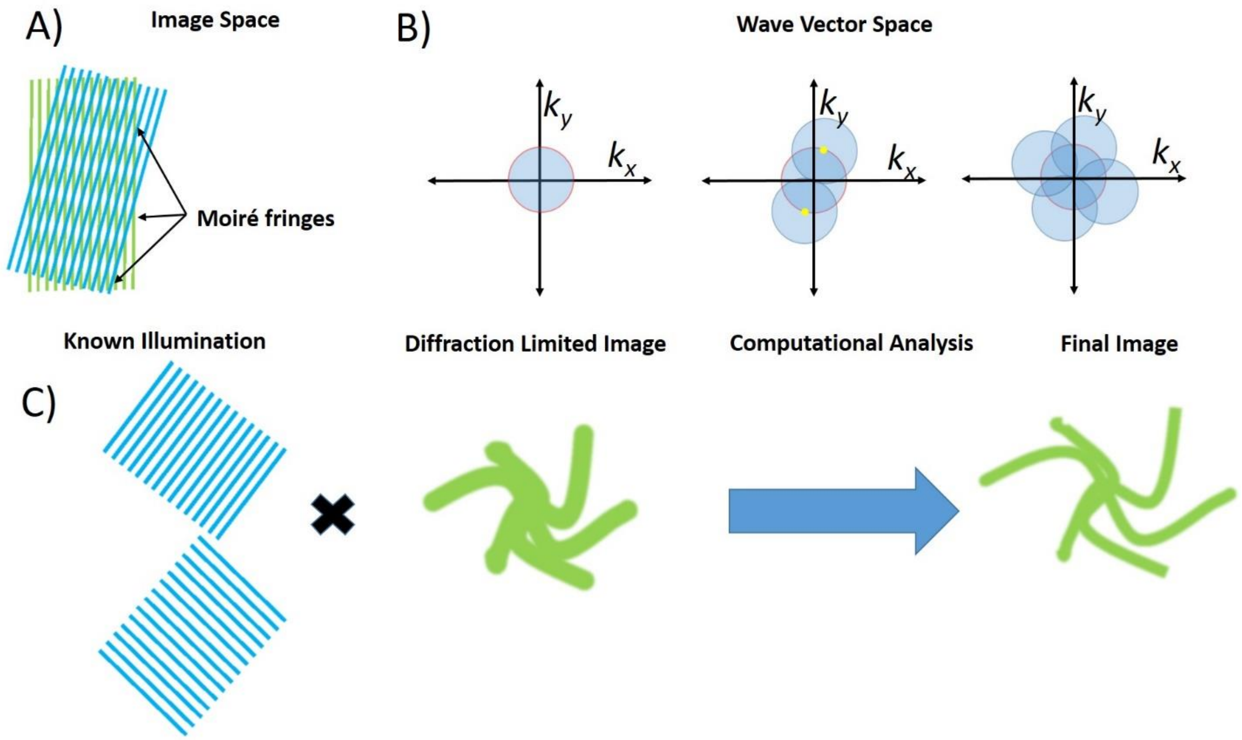

Figure 1.5 High spatial frequency patterned light (blue) is used to illuminate a specimen (green), resulting in low frequency Moiré fringes.
In wave vector space, the disc outlined in red represents the wave vectors the objective lens can detect. The specimen is illuminated with largest magnitude wave vector the objective can detect (white dots). This increases observable region of the objective by creating sidebands in image space which can be computationally analyzed to extract the high frequency information. The wave vector is rotated through different angles (right) which increases the final resolution of the image. C) Schematic in image space of light illuminating a specimen at different angles and phases. Following computational analysis, a high resolution image can be obtained.

In one example, Lesterlin et al. studied DNA double-strand breakage and subsequent repair using 3-D SIM in live E. coli, revealing unexpected roles of RecA bundles in DNA repair (20).

1.5 STIMULATED EMISSION DEPLETION MICROSCOPY (STED)

Stimulated emission depletion microscopy (STED) breaks the diffraction limit by utilizing two overlaid laser beams—an excitation beam and a depletion beam. The excitation beam is focused down to a spot and is used to excite an ensemble of molecules so that they can radiatively decay and emit photons. At the same time, a donut-shaped and red-shifted depletion beam reduces the excited state population of molecules in the periphery of the excited molecules by driving them to the ground state – resulting in stimulated emission of light outside the detection band. Effectively this causes very few of the molecules in that focal volume to be optically detected, shrinking the PSF to < 250 nm and breaking the diffraction limit. Images are acquired by raster scanning the two beams relative to the sample, and collecting light that is emitted from each point (**Figure 1.6)** (6).

STED microscopy has been used to great effect in order to observe somatosensory neurons in live transgenic mice expressing yellow fluorescent protein. Researchers achieved <70 nm resolution, revealing the movements of dendritic spines in the live brain (21). STED has also been used effectively in the field of virology because virus particles are much smaller than the diffraction limit. In one example, Chojnacki et al. visualized the glyco-protein distribution on the surface of individual HIV-1 particles. They found that rearrangements of the inner protein lattice, altered the virus surface, preparing it for successful entry into a host cell(22).

Compared to other modern super resolution techniques, STED can achieve resolution on par with single molecule localization (discussed next), but acquiring multiplexed images is challenging due to the fact that in most implementations two lasers are needed to acquire a single color channel. STED also is challenged with photobleaching because relatively high laser powers are required to shrink the PSF. Also, producing a doughnut shaped beam increases the complexity and cost of the optics.

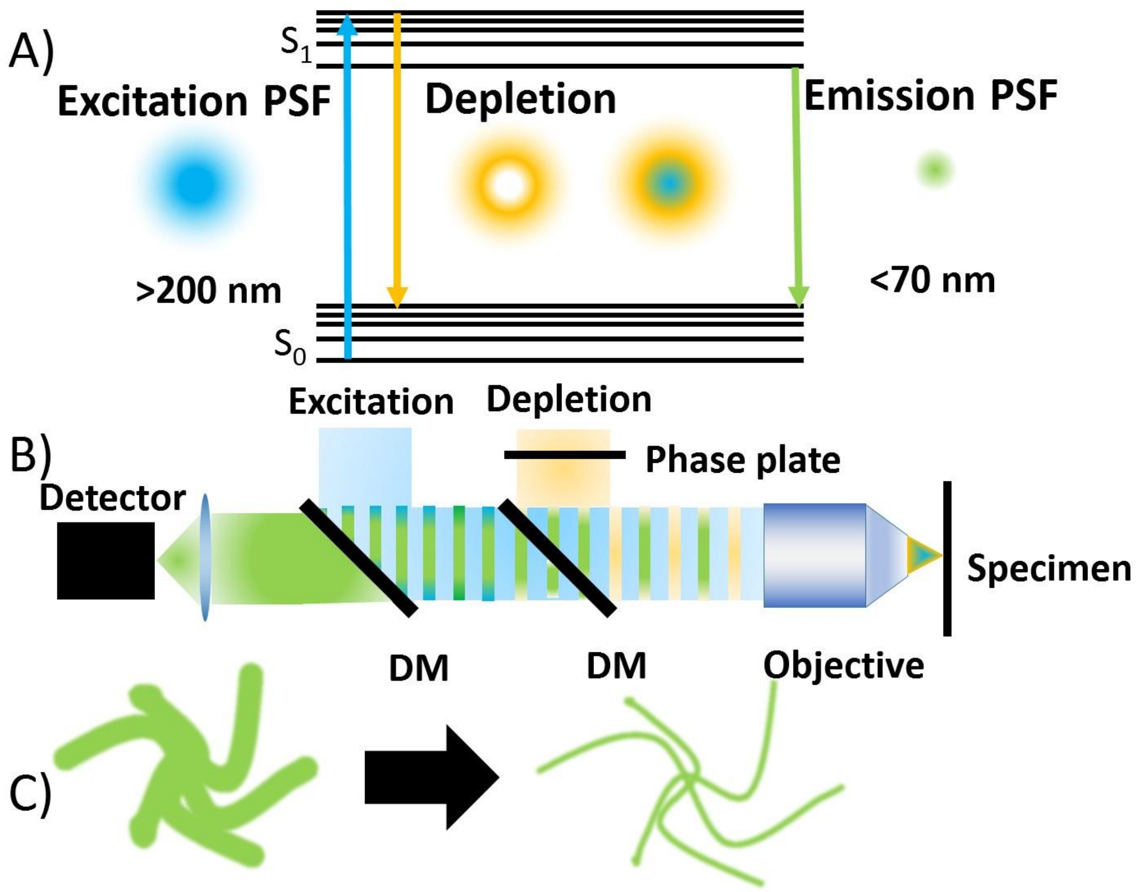

Figure 1.6 (A)In STED microscopy a blue excitation beam exciting ground state (S_0) molecules into the first excited state (S_1). The excitation beam is combined with a red-shifted, doughnut shaped depletion beam, which drives molecules from S_1 to S_0 resulting in red-shifted stimulated emission which is not detected. Consequently, only a small number of molecules emit detectable photons, which results in an emission PSF that is much smaller than the diffraction limit (<70 nm). (B) Diagram of a STED microscope. Beam-shaping optics are inserted in the depletion path in order to shape the beam into a doughnut. Note, sometimes the phase plate is used together with a carefully-positioned lens. (C)After the STED beam has been raster scanned over the specimen, a high resolution image is produced. Illustration depicts resolution improvement by STED.

1.6 SINGLE MOLECULE LOCALIZATION MICROSCOPY (SMLM)

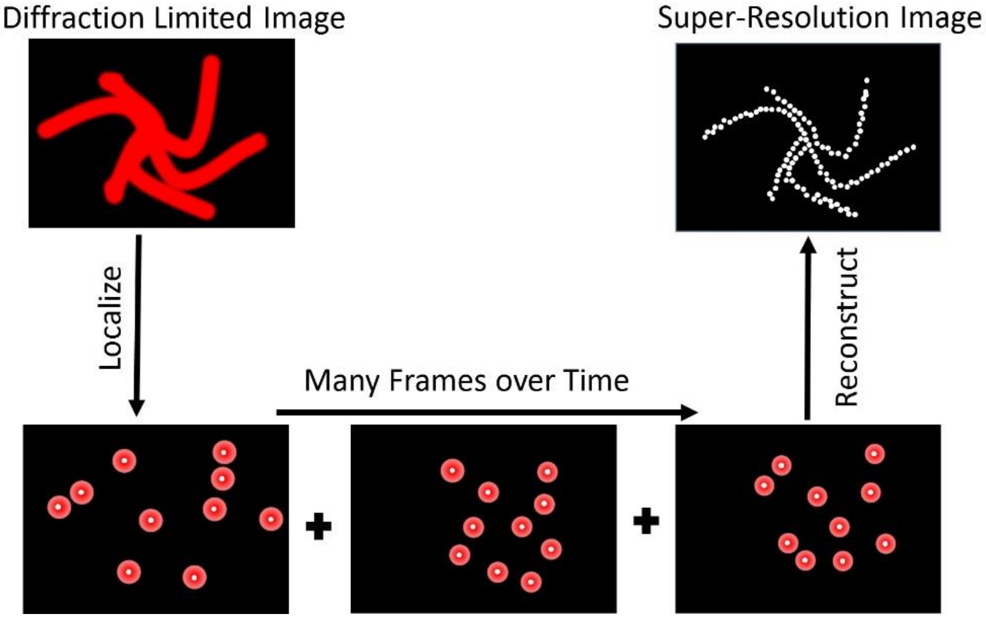

Figure 1.7 Depiction of SMLM microscopy. Under normal conditions a specimen is densely labeled with fluorophores whose PSFs are all overlapping, obscuring the fine detail beneath the diffraction limit. In SMLM, individual emitters are stochastically activated and imaged over many frames, ideally with no overlapping PSFs. After thousands of frames, the localizations are aggregated to reconstruct a super-resolution image, revealing fine structural details beneath the diffraction limit.

SMLM breaks the diffraction limit by stochastically observing sparse subsets of molecules sampled from a densely labeled cellular structure, and localizing their centroids with >25 nm accuracy. Under typical epi-fluorescence conditions a densely-labeled specimen would have its fine details obscured because all the emitters' PSFs would be overlapping. In contrast, SMLM separates out the emitters in time, such that for any individual frame there is a low probability that two or more molecules will be simultaneously emitting in the same excitation volume (8).

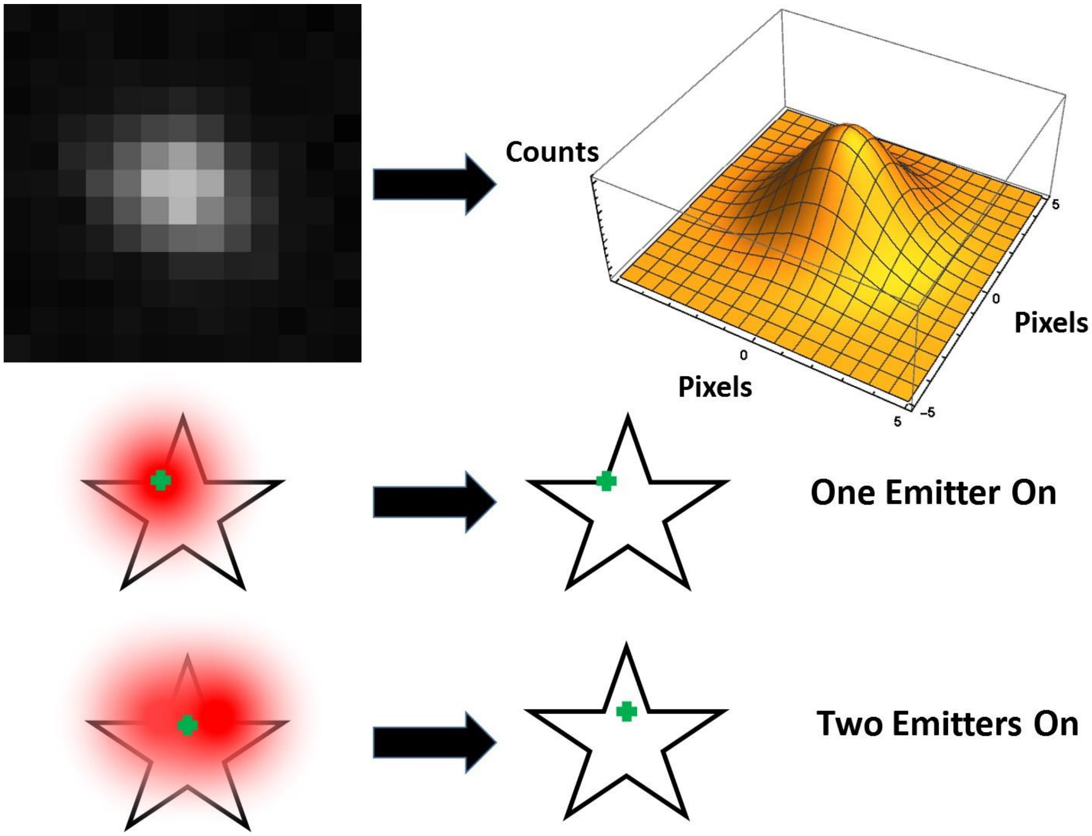

Figure 1.8 (Top Row)**:** A single molecule is fit with a Gaussian function in order to determine its mean position with sub-pixel accuracy. The uncertainty of the mean position is inversely proportional to the number of photons emitted. (Bottom Row) It is important at any moment in time there is only one emitter present per diffraction limited region. Ideally, only one molecule appears in the diffraction limited region resulting in a correct localization. However, if two or more fluorophores emit in the same focal volume the Gaussian fit is skewed which results in an incorrect localization that is approximately between the emitters.

For every frame during an acquisition the PSFs are identified, and each PSF's centroid is determined at sub-pixel accuracy and with extremely high precision (23–25). After a sufficient number of frames, typically thousands, an image is computationally reconstructed using the centroids of the localizations (**Figure 1.7)**. If the localizations are modeled using Gaussian functions, then one can approximate the uncertainty of the localization by the standard error of the mean for a Gaussian function, where σ is standard deviation of the Gaussian fit, and N is the number of detected photons (24).

$$uncertainty \propto \frac{\sigma}{\sqrt{N}} \qquad \text{Eq. 1.3}$$

Spreading out the localizations in time is important because overlapping PSFs are difficult to fit computationally and tends to produce so-called double-localization artifacts (**Figure 1.8)** (26). Importantly, there are a variety of techniques used to take a dense distribution of molecules and spread out their localizations over time so that they do not overlap, which are reviewed below.

1.7 USE OF FLUORESCENT PROTEINS IN SMLM:

Cells can be genetically modified to express fluorescent fusion proteins like photoactivatable green fluorescent protein (PA-GFP) in order to label structures of interest (9, 10). Initially PA-GFP is in a dark state and is not optically detectable. It is then switched to a bright state with illumination by an activation laser at one wavelength, and it is then visualized with illumination by an excitation laser at a different wavelength. The intensity of the activation laser is tuned such that only small number of molecules in the field of view are activated, and ideally separated by distances larger than the diffraction limit. Then the excitation laser is used to image the molecules so that their centroids can be determined, and then the molecules are photobleached. If this cycle is repeated many times over thousands of frames, a super resolved image can be reconstructed (9, 10).

This technique is advantageous because the probes are genetically encoded and can be used to observe cellular dynamics at super-resolution. For example, FPs were used to observe cellular adhesion dynamics in live Chinese Hamster Ovary (CHO) cells at <60 nm resolution (27). It is worth mentioning, that the high-powers required for imaging are often times toxic for cells, and photon-resistant cell lines must be used. Additionally, this technique is useful for probing cellular dynamics that occur on the time scale of minutes because multiple frames need to be recorded in order to create a snapshot in time. This implies that processes occurring faster than the imaging speed would get averaged out (i.e., would produce blurry images) or would be rendered invisible (27). Taken together this implies that the PALM could be improved by developing genetically encodable probes that are brighter and have higher quantum efficiencies. This would permit the use of lower power lasers, faster imaging, and the ability to image the specimen for a longer period of time.

1.8 USE OF ORGANIC FLUOROPHORES FOR SMLM

Organic fluorophores can be used to label proteins of interest by covalently linking them to antibodies which are targeted to proteins of interest. Alternatively, the fluorophores can be directly targeted via a genetically encoded SNAP or HALO tag (28–33). Then a chemical reaction is used to switch the dyes between a dark and fluorescent state, separating out the emitters in time. Like other techniques, bright and photo-stable probes are necessary for accurate localization. However, since the photoswitching behavior is photo-chemically controlled, conditions need to be manipulated such that the dye is fatigue-resistant, emits many photons, and remains mostly in its dark state. This is important because in any diffraction limited volume, it is desirable to only have one fluorophore emitting in order to avoid artifacts. The duty cycle of a dye, or the fraction time it is “on”, determines the probability that two fluorophores will be emitting in the same diffraction limited volume, and thus fundamentally limits the number of fluorophores that can be packed into a diffraction limited region before emitter PSFs overlap and create imaging artifacts (13, 26). Consequently, it is critical to select dyes that both emit many photons when switched into the “on” state, and remain mostly in their “off” state.

For example, cyanine dyes have been used in conjunction with an oxygen scavenger and thiol or tris(2-carboxyethyl)phophine (TCEP) in solution to produce ~25 nm resolution images in a matter of minutes (12). Also, oxazine dyes have been used in conjunction with ascorbic acid and methyl viologen in order to utilize redox chemistry to reversibly switch dyes between an emissive and non-emissive state (34). In a third example intramolecular reactions have been engineered into variants of rhodamine dye which switch by controlling formation of a spiro-ring to brake the conjugation of the fluorophore (35).

Dempsey et al. conducted a systematic study of 26 organic dyes that exhibited blinking behavior and could potentially be used for super-resolution imaging. In their study Alexa647 with a thiol (beta-mercaptoethanol) emerged as the most superior dye because it is very photostable, has many switching events before photobleaching, emits many photons per blink, and has a favorable duty cycle (**Figure 1.9)** (36). In practice this means Alexa647 is easy to use, and can produce excellent images. Compared to other methods, SMLM with Alexa647 can be performed at blazing fast frame rates (500-1000 Hz), allowing the accumulation of many high quality localizations in a matter of minutes (13, 36, 37). This is particularly advantageous because it allows structures to be highly sampled and an image to be generated on the order of minutes rather than hours. The order of magnitude higher data rate positions Alexa647 as the ideal fluorophore for high-throughput super-resolution microscopy applications like machine learning and artificial intelligence. Depmpsey et al. also identified spectrally distinct dyes which could be used for multiplexing however none of them provided an equivalent performance to Alexa 647 (36).

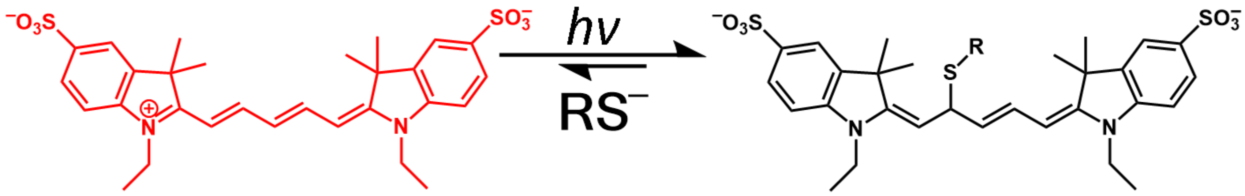

Figure 1.9 Photoswitching mechanism of Alexa647: The dye starts in a bright emissive state. When excited by red light it undergoes a reversible reaction with a thiolate anion, which attacks the polymethine bridge. This breaks the conjugation and renders the dye non-fluorescent.

1.9 CHALLENGES FOR ORGANIC FLUOROPHORES

Given the fact Alexa 647 is generally regarded as the best SMLM dye, methods for multiplexing utilizing only Alexa647 have been tried. For example, Alexa647 can be paired with Cy3 and A405 in an activator-reporter scheme (38). In this scheme, illumination of an activator molecule (Cy3 or A405) at its absorbance band (e.g., 560nm or 405nm) can be used to photoactivate nearby Alexa647-thiol adducts. Then Alexa647 is probed, and its location is assigned to the appropriate activator channel. Effectively, this gives two channel fluorescence using only Alexa647 however great care must be taken to minimize cross talk between the channels (38). In another example, researchers also have used cyclic-immunofluorescence to extend the number of channels that can be acquired. In this scheme, a specimen is immunostained, imaged, the fluorescent signal is quenched, and then the specimen can be immunostained for a different antigen (39, 40). Although this method is effective, it can take a whole day to acquire a few channels of data because re-staining, and finding the same location on the glass slide can be time consuming.

Even though Alexa 647 is the best dye, it is still prone to photobleaching, which is especially problematic if researchers want to obtain 3D images at extended depths. It is crucial to sample the structure of interest densely, and Legant et al. suggest sampling at 5x the Nyquist criteria because sampling is conducted stochastically rather than periodically. When performing 3D SMLM, the specimen is bathed in light, causing fluorophores outside the focal volume to photobleach before they can be localized. While it is possible to obtain 3D volumes by scanning the focal plane, the total number of available localizations must be divided up between all the focal planes (41, 42). Effectively, this lowers the density of localizations in each individual focal plane. This results in images that are lower quality because the structures were not sampled densely enough, and it fundamentally limits the imaging volume because once the specimen photobleaches completely no more information can be obtained

1.10 USE OF DNA CONJUGATED FLUOROPHORES FOR SMLM

In typical implementations of DNA points accumulation for imaging in nanoscale topography (DNA-PAINT), a specimen is labeled with anti-bodies bearing unique, short strands of DNA (< 20 nucleotides). The positions of the DNA barcodes and antibodies are read out, by flowing dye-conjugated reporter oligonucleotides over the specimen. The reporter oligonucleotide is chosen such that it is complimentary to one DNA-antibody conjugate and orthogonal to the rest. As it flows over the specimen, the reporter diffuses to its complimentary strand, and transiently binds and is localized with high precision. Most PAINT experiments are conducted in total internal reflection (TIRF) geometry, limiting the detection volume to a few hundred nanometers above the coverslip, which reduces the background originating from probes diffusing in the bulk solution (11, 43). More recent implementations of PAINT relax the TIRF geometry constraint by imaging through a confocal spinning disc, which reduces background by providing optical sectioning and allows large 3 dimensional volumes to be imaged (44). PAINT is also advantageous because fresh reporter probes are added during image acquisition, making it immune to photobleaching. Additionally, it does not depend on any special excited state properties of the fluorophores-allowing virtually any fluorescent molecule to be used (43).

While PAINT has numerous advantageous and is a notable super-resolution technique, it has a few drawbacks. First, PAINT is limited by how quickly the reporter probes bind to their complimentary targets within the cell. This association rate is directly proportional to the bulk concentration of probes, so a high concentration leads to a fast association rate. However, at the same time, a high concentration of bulk reporter leads to an increase in the background signal. At some point the bulk concentration gets high enough, that individual localizations are not observable against the background (11). This implies that the imaging speed of PAINT inherently is limited by the background against which the localizations are measured. As a result, PAINT experiments are typically performed around 20 Hz (45–47). This provides an acceptable level of bulk-background fluorescence, while allowing sufficient time for a reporter probe to diffuse into the detection volume, transiently bind to its target, get localized, and diffuse away. This can be problematic when imaging structurally dense targets which require very high sampling rates because the specimen may need to be on the stage for a day or more in order to accumulate a sufficient number of localizations (47).

1.11 SUMMARY

The last decade of developments in super-resolution imaging has set the stage for probing biological specimens at the nano-scale and will continue to develop into the future. Commercial versions of these instruments have become available, democratizing the techniques and making them available to a wide range of practitioners. However, there is still a need to develop and optimize sample preparation techniques, multiplexing strategies, and hardware setups in order to get these tools in the hands of practitioners. These categories span the space of chemistry, biology, and optics, and when brought together they enable researchers to examine the nano-scale structure of cells at >25 nm resolution.

This thesis addresses key issues across these disciplines. In **Chapter 2** I show the importance of sample preparation in super-resolution imaging. Then in **Chapter** 3 I show how bio-conjugate chemistry can be used to refresh the fluorescent signal of photobleached specimens, and to multiplex using a single dye. Finally, in **Chapter 4** I describe the importance of hardware to microscopy, and show how I have created setups that are highly customized for the end user.

1.12 REFERENCES

1. Crick, F. 1970. Central Dogma of Molecular Biology. Nature. 227: 561–563.

2. Hutchings, J. 1960. Engineering and Science, Volume 23:5, February 1960. Engineering and Science.

3. Müller, D.J., and Y.F. Dufrêne. 2011. Atomic force microscopy: a nanoscopic window on the cell surface. Trends in Cell Biology. 21: 461–469.

4. Chang, Y.-W., S. Chen, E.I. Tocheva, A. Treuner-Lange, S. Löbach, L. Søgaard-Andersen, and G.J. Jensen. 2014. Correlated cryogenic photoactivated localization microscopy and cryo-electron tomography. Nature Methods. 11: 737–739.

5. A., Lin, G., Krockmalnic, and S., Penman. 1990. Imaging cytoskeleton-mitochondrial membrane attachments by embedment-free electron microscopy of saponin-extracted cells. Proceedings of the National Academy of Sciences of the United States of America. 87: 8565–8569.

6. Hell, S.W., and J. Wichmann. 1994. Breaking the diffraction resolution limit by stimulated emission: stimulated-emission-depletion fluorescence microscopy. Optics letters. 19: 780–782.

7. Gustafsson, M.G. 2000. Surpassing the lateral resolution limit by a factor of two using structured illumination microscopy. J. Microsc. 198: 82–87.

8. Betzig, E. 1995. Proposed method for molecular optical imaging. Optics letters. 20: 237–239.

9. Betzig, E., G.H. Patterson, R. Sougrat, O.W. Lindwasser, S. Olenych, J.S. Bonifacino, M.W. Davidson, J. Lippincott-Schwartz, and H.F. Hess. 2006. Imaging intracellular fluorescent proteins at nanometer resolution. Science. 313: 1642–1645.

10. Hess, S.T., T.P.K. Girirajan, and M.D. Mason. 2006. Ultra-high resolution imaging by fluorescence photoactivation localization microscopy. Biophys. J. 91: 4258–4272.

11. Jungmann, R., C. Steinhauer, M. Scheible, A. Kuzyk, P. Tinnefeld, and F.C. Simmel. 2010. Single-Molecule Kinetics and Super-Resolution Microscopy by Fluorescence Imaging of Transient Binding on DNA Origami. Nano Lett. 10: 4756–4761.
12. Rust, M.J., M. Bates, and X. Zhuang. 2006. Sub-diffraction-limit imaging by stochastic optical reconstruction microscopy (STORM). Nat Methods. 3: 793–796.

13. van de Linde, S., A. Löschberger, T. Klein, M. Heidbreder, S. Wolter, M. Heilemann, and M. Sauer. 2011. Direct stochastic optical reconstruction microscopy with standard fluorescent probes. Nat. Protocols. 6: 991–1009.

14. Hanser, B.M., M.G.L. Gustafsson, D.A. Agard, and J.W. Sedat. 2003. Phase retrieval for high-numerical-aperture optical systems. Optics Letters. 28: 801.

15. Hanser, B.M., M.G.L. Gustafsson, D.A. Agard, and J.W. Sedat. 2004. Phase-retrieved pupil functions in wide-field fluorescence microscopy. Journal of microscopy. 216: 32–48.

16. Abbe, E. 1873. Beiträge zur Theorie des Mikroskops und der mikroskopischen Wahrnehmung: I. Die Construction von Mikroskopen auf Grund der Theorie. Archiv für Mikroskopische Anatomie. 9: 413–418.

17. F.R.S, L.R. 1879. XXXI. Investigations in optics, with special reference to the spectroscope. The London, Edinburgh, and Dublin Philosophical Magazine and Journal of Science. 8: 261–274.

18. Goodsell, D.S. 2010. Mitochondrion. Biochemistry and Molecular Biology Education. 38: 134–140.

19. Gustafsson, M.G.. 2005. Nonlinear structured-illumination microscopy: wide-field fluorescence imaging with theoretically unlimited resolution. Proceedings of the National Academy of Sciences of the United States of America. 102: 13081.

20. RecA bundles mediate homology pairing between distant sisters during DNA break repair | Nature

21. Berning, S., K.I. Willig, H. Steffens, P. Dibaj, and S.W. Hell. 2012. Nanoscopy in a Living Mouse Brain. Science. 335: 551–551.

22. Chojnacki, J., T. Staudt, B. Glass, P. Bingen, J. Engelhardt, M. Anders, J. Schneider, B. Muller, S.W. Hell, and H.-G. Krausslich. 2012. Maturation-Dependent HIV-1 Surface Protein Redistribution Revealed by Fluorescence Nanoscopy. Science. 338: 524–528.

23. Ma, H., J. Xu, J. Jin, Y. Gao, L. Lan, and Y. Liu. 2015. Fast and Precise 3D Fluorophore Localization based on Gradient Fitting. Sci Rep. 5: 14335.

24. Thompson, R.E., D.R. Larson, and W.W. Webb. 2002. Precise nanometer localization analysis for individual fluorescent probes. Biophys J. 82: 2775–2783.

25. Babcock, H.P., and X. Zhuang. 2017. Analyzing Single Molecule Localization Microscopy Data Using Cubic Splines. Sci Rep. 7.

26. van de Linde, S., S. Wolter, M. Heilemann, and M. Sauer. 2010. The effect of photoswitching kinetics and labeling densities on super-resolution fluorescence imaging. J. Biotechnol. 149: 260–266.

27. Shroff, H., C.G. Galbraith, J.A. Galbraith, and E. Betzig. 2008. Live-cell photoactivated localization microscopy of nanoscale adhesion dynamics. Nat Meth. 5: 417–423.

28. Cole, N.B. 2013. Site-Specific Protein Labeling with SNAP-Tags: Site-Specific Labeling with SNAP-Tags. In: Coligan JE, BM Dunn, DW Speicher, PT Wingfield, editors. Current Protocols in Protein Science. Hoboken, NJ, USA: John Wiley & Sons, Inc. pp. 30.1.1-30.1.16.

29. Campos, C., M. Kamiya, S. Banala, K. Johnsson, and M. González-Gaitán. 2011. Labelling cell structures and tracking cell lineage in zebrafish using SNAP-tag. Developmental Dynamics. 240: 820–827.

30. Keppler, A., S. Gendreizig, T. Gronemeyer, H. Pick, H. Vogel, and K. Johnsson. 2002. A general method for the covalent labeling of fusion proteins with small molecules in vivo. Nature Biotechnology. 21: 86–89.

31. Keppler, A., M. Kindermann, S. Gendreizig, H. Pick, H. Vogel, and K. Johnsson. 2004. Labeling of fusion proteins of O6-alkylguanine-DNA alkyltransferase with small molecules in vivo and in vitro. Methods. 32: 437–444.
32. Keppler, A., H. Pick, C. Arrivoli, H. Vogel, and K. Johnsson. 2004. Labeling of fusion proteins with synthetic fluorophores in live cells. Proceedings of the National Academy of Sciences of the United States of America. 101: 9955–9959.

33. Los, G.V., L.P. Encell, M.G. McDougall, D.D. Hartzell, N. Karassina, C. Zimprich, M.G. Wood, R. Learish, R.F. Ohana, M. Urh, D. Simpson, J. Mendez, K. Zimmerman, P. Otto, G. Vidugiris, J. Zhu, A. Darzins, D.H. Klaubert, R.F. Bulleit, and K.V. Wood. 2008. HaloTag: A Novel Protein Labeling Technology for Cell Imaging and Protein Analysis. ACS Chemical Biology. 3: 373–382.

34. Deniz, E., M. Tomasulo, J. Cusido, I. Yildiz, M. Petriella, M.L. Bossi, S. Sortino, and F.M. Raymo. 2012. Photoactivatable Fluorophores for Super-Resolution Imaging Based on Oxazine Auxochromes. The Journal of Physical Chemistry C. 116: 6058–6068.
35. Belov, V.N., and M.L. Bossi. 2013. Photoswitching Emission with Rhodamine Spiroamides for Super-resolution Fluorescence nanoscopies. Israel Journal of Chemistry. 53: 267–279.

36. Dempsey, G.T., J.C. Vaughan, K.H. Chen, M. Bates, and X. Zhuang. 2011. Evaluation of fluorophores for optimal performance in localization-based super-resolution imaging. Nat. Methods. 8: 1027–1036.

37. Babcock, H.P. 2018. Multiplane and Spectrally-Resolved Single Molecule Localization Microscopy with Industrial Grade CMOS cameras. Sci Rep. 8: 1–8.

38. Bates, M., B. Huang, G.T. Dempsey, and X. Zhuang. 2007. Multicolor super-resolution imaging with photo-switchable fluorescent probes. Science. 317: 1749–1753.

39. Lin, J.-R., M. Fallahi-Sichani, and P.K. Sorger. 2015. Highly multiplexed imaging of single cells using a high-throughput cyclic immunofluorescence method. Nature Communications. 6: ncomms9390.

40. Tam, J., G.A. Cordier, J.S. Borbely, Á. Sandoval Álvarez, and M. Lakadamyali. 2014. Cross-Talk-Free Multi-Color STORM Imaging Using a Single Fluorophore. PLoS One. 9: e101772.
41. Huang, F., G. Sirinakis, E.S. Allgeyer, L.K. Schroeder, W.C. Duim, E.B. Kromann, T. Phan, F.E. Rivera-Molina, J.R. Myers, I. Irnov, M. Lessard, Y. Zhang, M.A. Handel, C. Jacobs-Wagner, C.P. Lusk, J.E. Rothman, D. Toomre, M.J. Booth, and J. Bewersdorf. 2016. Ultra-High Resolution 3D Imaging of Whole Cells. Cell. 166: 1028–1040.

42. Huang, B., W. Wang, M. Bates, and X. Zhuang. 2008. Three-dimensional super-resolution imaging by stochastic optical reconstruction microscopy. Science. 319: 810–813.

43. Jungmann, R., M.S. Avendaño, J.B. Woehrstein, M. Dai, W.M. Shih, and P. Yin. 2014. Multiplexed 3D cellular super-resolution imaging with DNA-PAINT and Exchange-PAINT. Nature Methods. 11: 313–318.

44. Schueder, F., J. Lara-Gutiérrez, B.J. Beliveau, S.K. Saka, H.M. Sasaki, J.B. Woehrstein, M.T. Strauss, H. Grabmayr, P. Yin, and R. Jungmann. 2017. Multiplexed 3D super-resolution imaging of whole cells using spinning disk confocal microscopy and DNA-PAINT. Nat. Commun. 8: 2090.

45. Werbin, J.L., M.S. Avendaño, V. Becker, R. Jungmann, P. Yin, G. Danuser, and P.K. Sorger. 2017. Multiplexed Exchange-PAINT imaging reveals ligand-dependent EGFR and Met interactions in the plasma membrane. Scientific Reports. 7.

46. Agasti, S.S., Y. Wang, F. Schueder, A. Sukumar, R. Jungmann, and P. Yin. 2017. DNA-barcoded labeling probes for highly multiplexed Exchange-PAINT imaging. Chem. Sci. 8: 3080–3091.

47. Legant, W.R., L. Shao, J.B. Grimm, T.A. Brown, D.E. Milkie, B.B. Avants, L.D. Lavis, and E. Betzig. 2016. High-density three-dimensional localization microscopy across large volumes. Nat. Meth. 13: 359–365.

Chapter 2. 'POINT BY POINT': AN INTRODUCTORY GUIDE TO SAMPLE PREPARATION FOR SINGLE-MOLECULE SUPER-RESOLUTION FLUORESCENCE MICROSCOPY

2.1 PREFACE

A great super-resolution image starts with careful sample preparation. Super-resolution techniques are ideal for showing the fine structure of cells as long as the structure is well preserved and labeled. It is a common misconception that super-resolution techniques can take a poorly prepared sample and improve the image quality. In fact, these techniques do the opposite, and instead reveal and amplify artifacts due to sample preparation. Consequently, it is critical that the sample be well preserved and labeled before proceeding to super-resolution imaging.

The protocol which I co-authored below was my first project. Since I was a new practitioner of super-resolution imaging, I played an important role in validating the procedures outlined in the article, and in ensuring that the directions were clear to novices. This was an ideal project to start with because it laid the foundation for my past and future work in microscopy.

The following material in this chapter is reproduced with permission from:

Halpern, A.R., **M.D. Howard**, and J.C. Vaughan. 2015. Point by Point: An Introductory Guide to Sample Preparation for Single-Molecule, Super-Resolution Fluorescence Microscopy. Current Protocols in Chemical Biology. Hoboken, NJ, USA: John Wiley & Sons, Inc. pp. 103–120.

2.2 ABSTRACT

Single-molecule localization-based super resolution microscopy is able to reveal detailed sub-cellular structures and protein distributions below the classical ~250 nm diffraction limit of light, but utilizing the technique effectively requires a combination of careful sample preparation, data acquisition, and data analysis which can be daunting to newcomers. In this protocol, we provide detailed instructions on preparation of robust reference samples for super-resolution microscopy, including the cytoskeleton (microtubules), membrane-bound organelles (peroxisomes), and scaffold proteins (clathrin). These samples also constitute a representative subset of imaging targets of interest to biological researchers which instruct on the differences and similarities in sample preparation.

Keywords: Super-resolution microscopy, STORM, PALM, microtubules, peroxisomes, clathrin

2.3 INTRODUCTION

Fluorescence microscopy has become an indispensable tool in biology owing to its ability to non-invasively image specific biological molecules or structures in fixed or living cells. Traditionally, fluorescence microscopy has faced the limitation of a poor spatial resolution (~250 nm) that is mismatched to the length scales of the molecular building blocks of the cell (e.g., ~3 nm for a small protein) by about two orders of magnitude. Electron microscopy and atomic force microscopy attain much higher spatial resolution, on the order of a few nanometers or better, but generally with poor molecular specificity and/or the limitation of measuring surface features. Super-resolution fluorescence imaging techniques now bridge the gap between the ~250 nm optical diffraction limit and the molecular scale, with routine measurements now in the ~20-50 nm range, while maintaining high molecular specificity and capabilities for live-cell imaging.

One set of approaches to circumvent or extend the diffraction limit utilizes patterned light to restrict fluorescence to defined regions within the sample and then repeats this process by scanning the patterned light across the sample, such as in Stimulated Emission and Depletion (STED) microscopy or Structured Illumination Microscopy (SIM) (1–5). Another approach utilizes stochastic single-molecule localization in order to determine the positions of the individual fluorescent molecules labeling the sample. The single-molecule approach is known by several names, including Stochastic Optical Reconstruction Microscopy (STORM) (6, 7) and (fluorescence) Photoactivated Localization Microscopy ((f)PALM) (8, 9). For simplicity sake, we refer to the single-molecule approach here as STORM/PALM.

While immensely enabling, these super-resolution imaging techniques are also more challenging than many traditional fluorescence imaging techniques. Key factors include sample quality (structure preservation and fluorescent labeling), imaging cocktail, laser power density, camera frame rate, stage drift, multicolor imaging, image analysis, and reconstruction. Each of these factors can affect the quality of the output images, and some of these can be difficult to troubleshoot. In this protocol we will focus on the fluorescent immunostaining of three exemplary structures for STORM/PALM imaging, microtubules, peroxisomes, and clathrin, all of which exhibit distinct sub-diffraction limit features, as well as dye selection, antibody labeling, and imaging conditions. Our goals are twofold. First, we aim to provide robust protocols for generation of excellent reference samples which practitioners can use to benchmark the performance of their microscope and analysis procedures.

Second, we hope to highlight some of the important considerations in staining a variety of samples, since the challenges and details of sample preparation are typically underappreciated by new users of these techniques.

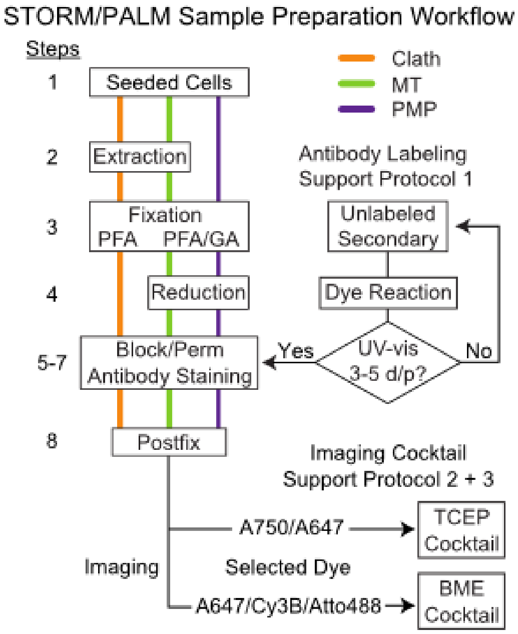

Figure 2.1 Sample preparation workflow and corresponding protocol steps for staining tubulin (MT, green), peroxisome membrane protein 70 (PMP, purple), or clathrin (Clath, orange). Secondary antibody dye conjugates are used for cell staining in step 7, and are described in Support Protocol 1. An imaging cocktail is used to facilitate photoswitching and should be appropriately matched to the dyes selected in the staining procedure (e.g., BME cocktail for Atto 488), as described in Support Protocols 2 and 3.

The structures we have chosen include the following. Microtubules are representative of the cytoskeleton and, when labeled with primary/secondary antibodies for fluorescence immunostaining that somewhat broaden the structure, exhibit a longitudinal hollow feature ~35-40 nm in diameter. Peroxisomes are representative membrane-bound organelles which can adopt a variety of morphologies, but in the cell lines we have chosen here, exhibit a 60-90 nm hollow stripe. Finally, clathrin is representative of scaffold proteins and appears toroidal with diameters of ~100-200 nm. The successful observation of these features can help confirm that all aspects of the sample preparation, instrument, and analysis are working well and provide a good starting point for the beginner super-resolution microscopist.

We note that a related set of challenges is faced by practitioners who use photoswitchable or photoactivatable fluorescent proteins for STORM/PALM, in terms of sample preservation and fluorescent protein choice (10–13). Readers may also want to consult other excellent reviews which address in detail the instrumentation and analysis for STORM/PALM (14–16).

2.4 STRATEGIC PLANNING

The suggested targets addressed in this protocol are microtubules, peroxisomes and clathrin; slight modifications in the procedure are necessary for the successful staining of each structure and are displayed schematically in Figure 2.1. These choices include, extraction, fixative, and dye selection and are addressed below.

Extraction involves briefly exposing the cells to a detergent solution to remove the cellular membrane and many cytoplasmic proteins prior to fixation. This allows antibodies easier access to their binding sites, increasing the density of labeling, a key parameter of resolution which will be discussed later, and also lowering nonspecific background fluorescence. **Figure 2.2** shows an example where microtubules (green) in an extracted cell are more than twice as bright (e.g., more densely labeled) as the microtubules in a non-extracted cell. The background levels are also substantially lower in the extracted cell, likely due to the absence of free tubulin heterodimers or other cytoplasmic factors removed by extraction that could bind the anti-tubulin antibody. In general, extraction is suggested as an option for cytoskeletal proteins and scaffold proteins, and has been successfully applied to image structures such as microtubules, vimentin, and actin, and is also recommended when staining for clathrin. Many cellular structures are heavily perturbed by extraction, though, especially membrane-bound organelles.

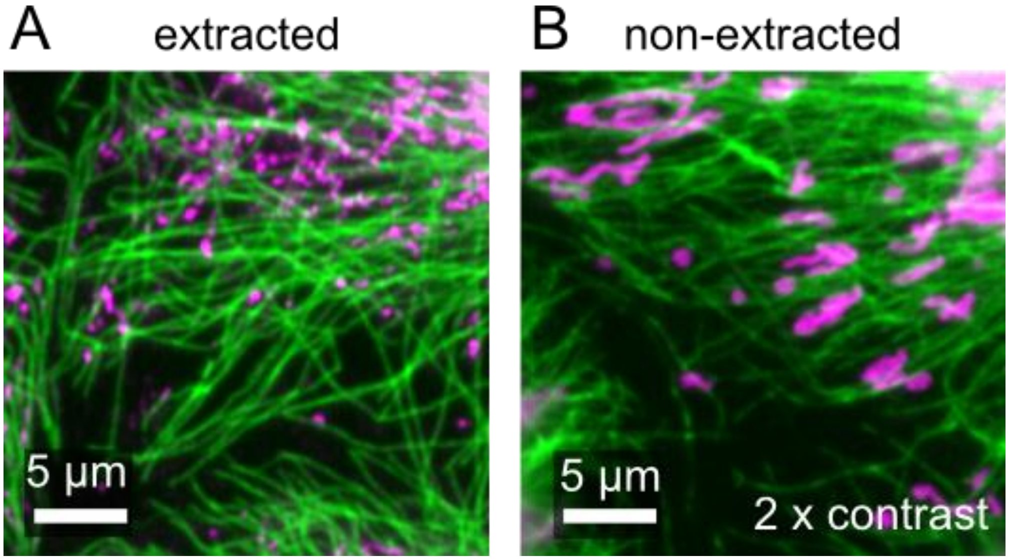

Figure 2.2 Conventional fluorescence images of fixed cells immunostained for microtubules and mitochondria, with and without extraction. The extracted cell (A) shows homogenous, densely labeled microtubules (green), but fractured mitochondria (magenta). A non-extracted, fixed cell (B) shows weakly labeled microtubules, but intact mitochondria. The contrast in (B) has been increased by a factor of two in both channels. Scale bar 5 μm

For example, in **Figure 2.2A**, mitochondria in extracted cells have been badly fragmented, whereas mitochondria in non-extracted cells (Fig. 2.2B) are well-preserved. The primary concerns of fixation in immunostaining are to preserve the structure of the sample while also preserving antigenicity. Glutaraldehyde, or a mixture of glutaraldehyde and paraformaldehyde (GA/PFA), can provide excellent preservation of structure in cultured cells but often compromises antibody binding due to the strong ability of GA to crosslink samples. Paraformaldehyde alone has less problems with loss of antigenicity but may not preserve the structure of interest. Another popular procedure uses cold organic solvents such as methanol or acetone to fix specimens, but these can damage delicate membrane-bound organelles similarly to extraction (**Figure 2.1**). In any event, choice of fixative and antibody are critical parameters when optimizing an immunostaining protocol (17). In the example protocols shown here, PFA/GA fixation nicely preserves microtubule and peroxisome structures while maintaining antigenicity to the antibodies which label the structures. In contrast, we observed that PFA/GA fixation compromises antigenicity of the anti-clathrin antibody and we therefore optimized clathrin immunostaining with a PFA-only protocol.

A final consideration in the staining process is the selection of an appropriate dye, or combination of dyes for multicolor imaging. Desirable properties of dyes for conventional fluorescence microscopy typically include a high brightness and photostability. Photostability is particularly important for super resolution techniques such as STED or SIM which involve scanning procedures that are sensitive to photobleaching during acquisition. However, for localization microscopy, two additional critical single-molecule characteristics that will determine resolution are: a high photon output per switching event, and a low duty cycle. These single-molecule properties will be discussed further later in this protocol and are also reviewed in depth by Dempsey et al. for a wide range of commercially available fluorophores and imaging cocktail solutions (18).

The recommendations for different spectral regions are Atto 488, Cy3B, Cy5/Alexa Fluor 647 or Cy7/Alexa Fluor 750. It should be stressed that although good results are obtainable with all of these dyes, Cy5/Alexa Fluor 647 preforms noticeably better and is more forgiving to beginner super resolution microscopists. These fluorophores are sensitive to their chemical environment, and this sensitivity is exploited to by formulating imaging cocktail that facilitates robust photoswitching. An imaging cocktail containing a thiol and an oxygen scavenging system is perhaps the best starting point for general purpose imaging, although Atto488, Cy3B, and Cy7/Alexa Fluor 750 perform substantially more poorly than Cy5/Alexa Fluor 647 (18). An alternative imaging cocktail for high-quality two-channel imaging with Cy5/Alexa Fluor 647 and Cy7/Alexa Fluor 750 utilizes the phosphine TCEP (tris(2-carboxyethyl)phosphine), and attains comparable performance in each channel (19).

2.5 PROTOCOL: IMMUNOSTAINING OF CULTURED CELLS

The immunostaining protocol begins with an optional extraction step that reduces fluorescent background and increases labeling density when staining for tubulin or clathrin. The cells are immediately fixed in a PFA/GA or PFA only solution that will preserve the cellular structure of interest while retaining antigenicity for immunostaining. The anti-tubulin antibodies and the anti-PMP70 antibody against peroxisome membrane protein 70 both bind their respective epitopes with PFA/GA fixation. In contrast, we achieved better staining for clathrin using PFA-only fixation.

Cells fixed with PFA/GA are briefly exposed to a mild reducing agent to quench reactive free aldehydes and to lower the autofluorescence created by the reaction of GA with flavins or other factors in the cell that then become fluorescent. The immunostaining steps then include a blocking and permeabilization solution (Block/Perm), followed by an incubation with the primary antibodies, and then incubation with a secondary antibody labeled with organic fluorophores. As mentioned previously, dye choice is critical in STORM/PALM and we have selected to use two cyanines, Alexa Fluor 647 and Alexa Fluor 750 in a BME and TCEP imaging cocktail, respectively, for the two color staining of tubulin. These dyes are able to reveal the microtubule hollow structure in both color channels (19). If however a 750 nm excitation source is not available, comparable results can be obtained using the fluorophore Cy3B with a more commonly available laser line around 560 nm. To finish the procedure, the stained cells are postfixed to increase their long term stability, and can be used for many months after staining when stored correctly. For a brief description of secondary antibody labeling, imaging cocktails and conditions, refer to the Support Protocols.

The user may choose any one of the four antibodies listed below for single-channel imaging. In that case, we recommend Alexa Fluor 647 on the secondary antibody. Additionally, the user may co-stain for two or more structures for multi-color imaging, with tubulin/detyrosinated as perhaps the easiest choice. In that case, two primary antibodies are included in the primary antibody incubation solution and two secondary antibodies bearing different fluorescent dyes are included in the secondary antibody incubation solution. We recommend either Alexa Fluor 647, Alexa Fluor 750 (with the TCEP imaging cocktail) or Alexa Fluor 647, Cy3B (with the thiol imaging cocktail).

Note that this same set of immunostaining protocols can be adapted for other imaging techniques, including standard widefield microscopy, confocal microscopy, STED microscopy, or SIM, with minimal modification. In particular, STED microscopy and SIM may require different choices of fluorescent dyes and mounting to minimize aberrations due to index mismatch (20).

Materials List

BS-C-1 cells (African green monkey kidney, ATCC CCL-26)

Eight-well, no. 1.5 coverglass chamber (Nunc Labtek II #155409 or Ibidi μ-Slide #80821)

Extraction solution

PFA/GA fixation solution (when using the antibodies against tubulin or PMP70) or

PFA-only fixation solution (for clathrin)

Phosphate buffered saline (PBS) pH 7.4

Storage solution

1 mg/mL (26 mM) sodium borohydride solution in water, prepared immediately prior to use
Block/Perm buffer

Primary antibody solution in Block/Perm buffer containing either:

For microtubules (two-color)

Rat anti-alpha tubulin YL1/2 (Pierce, MA1-80017, 1 mg/mL) diluted 1:100 to 10 μg/mL

Rabbit anti-detyrosinated tubulin (Abcam, Ab48389, whole serum) diluted 1:500

For peroxisomes

Rabbit anti-PMP70 (Invitrogen, 78-3100, 500 μg/mL) diluted 1:500 to 1 μg/mL

For clathrin

Mouse anti-clathrin X-22 (Abcam, ab2731, 6 mg/mL) diluted 1:1500 to 4 μg/mL

Secondary antibody solution (see Support Protocol 1) in Block/Perm buffer containing either:

For microtubules (two-color)

Donkey anti-rat (Jackson, 712-005-150) Alexa Fluor 750 conjugate diluted to 2 μg/mL

Donkey anti-rabbit (Jackson, 711-005-152) Alexa Fluor 647 conjugate diluted to 2 μg/mL

For peroxisomes

Donkey anti-rabbit (Jackson, 711-005-152) Alexa Fluor 647 conjugate diluted to 2 μg/mL

For clathrin

Donkey anti-mouse (Jackson, 715-005-151) Alexa Fluor 647 conjugate diluted to 2 μg/mL

Postfixation solution

2.5.1 *Seeding Cells and Coverglass Chamber*

1) Seed BS-C-1 cells 12-24 hours prior to fixation in a LabTek II or Ibidi 8-well coverglass chamber aiming for 50-70% confluency at the time of fixation. Typically, we will seed 4.3×10^4 cells/cm^2 ($3\text{x}10^4$ cells per well) one day prior to staining. In the following steps, we recommend using at least 125 μL of solution per well of the 8-well chamber in order to fully cover the surface with the solution. This is important to protect the surface from drying, and also to minimize the usage of valuable reagents, particularly the primary and secondary antibodies. For less valuable reagents, such as the extraction or fixation solutions, the volume per well can be increased if desired. Careful handling is needed to ensure the delicate coverslip is not cracked during the staining.

2.5.2 *Extraction*

2) (Optional, but highly recommended when staining for tubulin or clathrin). Remove cells from incubator, aspirate media from the desired wells and add 125 μL of extraction solution. Remove the extraction solution after 30 seconds and immediately proceed to step 3.

2.5.3 *Fixation*

3) (If step 2 extraction was skipped, aspirate medium.) Add at least 125 μL of fixation solution per well. When staining for tubulin, or PMP70, use the PFA/GA fixation solution. For staining clathrin, use the PFA-only fixation solution. After 10 minutes, remove the fixative and wash 3× with PBS.

4) (Optional, but highly recommended for samples fixed with PFA/GA.) Add at least 125 μL of freshly prepared $NaBH_4$ solution and incubate for 10 minutes. Some small bubbles should be

visible on the coverglass surface which indicate the evolution of H_2 gas due to the hydrolysis of $NaBH_4$ in water. Rinse the sample 3× with PBS. Note: After this step, if desired, the immunostaining process can be postponed by storing the fixed cells in Storage solution at 4°C. We have successfully immunostained cells one week after fixation without noticeable loss in quality.

2.5.4 *Immunostaining*

5) Aspirate the PBS rinse (or storage solution) and add at least 125 µL of Block/Perm solution per well. Incubate for 45 minutes in a humidity chamber to ensure the wells do not dry out. Use the time during the incubation to prepare the primary and secondary antibody dilutions: For two color tubulin stain, the primary antibody solution will contain both the rat anti-alpha tubulin and rabbit anti-detyrosinated tubulin antibodies. The secondary antibody solution will contain both the donkey anti-rat Alexa Fluor 750 conjugate and donkey anti-rabbit Alexa Fluor 647 conjugate. For the single color peroxisome stain, the primary and secondary antibody solutions will contain rabbit anti-PMP70 and donkey anti-rabbit Alexa Fluor 647 conjugate, respectively. For the single color peroxisome stain, the primary and secondary antibody solutions will contain mouse anti-clathrin and donkey anti-mouse Alexa Fluor 647 conjugate, respectively.

6) Aspirate the Block/Perm solution. Add 125 µL of primary antibody solution per well and incubate for 45 minutes at 25°C in a humidity chamber. Note that use of the chamber lids during primary or secondary antibody staining steps is not recommended as the solution has a tendency to creep up chamber walls and can potentially contaminate neighboring wells. Aspirate the primary antibody solution and rinse 3× with PBS. For the final rinse, allow the chamber to incubate for 5 minutes before removing.

7) Add 125 µL of secondary antibody solution per well. Incubate for 45 minutes at 25°C in a humidity chamber, then aspirate secondary antibody solution and rinse 3× with PBS. For the final rinse, allow the chamber to incubate for 5 minutes before removing.

2.5.5 *Postfixation and Storage*

8) Add at least 125 µL of postfix solution per well and incubate for 10 minutes. After removing the postfix solution, rinse with PBS. The sample is ready for imaging, or can be stored in Storage solution at 4°C for up to 6 months or longer.

9) It is highly recommended to verify the quality of the stain on a conventional fluorescence microscope before attempting to image by STORM/PALM. The conventional fluorescence image should appear bright, homogenously fluorescent, and continuous, as described previously and shown in Figure 2.2A for microtubules.

2.6 SUPPORT PROTOCOL 1: SECONDARY ANTIBODY LABELING WITH NHS FLUOROPHORES

This protocol describes how to create antibody–dye conjugates using commercially available fluorophores that are functionalized with NHS (n-hydroxy succinimidyl) ester for covalent linkage with amines. Although preconjugated antibodies are commercially available, the user is encouraged to label their own secondary antibodies since the reaction is relatively easy, economical, and, importantly, offers control of the dye to protein (d/p) labeling ratio. After the reaction is completed, the antibodies are purified by size exclusion to remove unreacted dyes, and the d/p ratio is calculated taking into account the proper correction factors, as shown below. For this work, we have suggested four dyes, Atto488, Cy3B, Alexa Fluor 647 and Alexa Fluor 750 that currently offer the best switching properties in four separate spectral regions. However, note that this protocol is general and can be applied to other fluorophores with suitable bioconjugation groups (e.g., succinimidyl ester, maleimide, etc.) and photoswitching properties.

Material List

Alexa Fluor 750, NHS ester (Thermo Fisher / Life Technologies, A-20111)

Alexa Fluor 647, NHS ester (Thermo Fisher / Life Technologies, A-20006)

Cy3B, NHS ester (GE Healthcare, PA63101)

ATTO 488, NHS ester (Atto-Tec, AD 488-31)

Anhydrous dimethyl sulfoxide (DMSO)

1 M stock solution of sodium bicarbonate, freshly prepared

Phosphate buffered saline (PBS) pH 7.4

Donkey anti-rat (min Mouse), unconjugated secondary antibody (Jackson, 712-005-153)

or

Donkey anti-rabbit, unconjugated secondary antibody (Jackson, 711-005-152)

or

Donkey anti-mouse (min Rat), unconjugated secondary antibody (Jackson, 715-005-151)

Illustra Nap-5 columns, Sephadex G-25 (GE Healthcare, 17-0853-02)

UV-vis spectrometer and reduced volume cuvette

2.6.1 *Labeling Reaction*

1) (Optional) If starting with a powdered or lyophilized form of NHS dye, it is necessary to create a dye stock solution in dry DMSO. We recommend creating a concentrated DMSO stock (~100 μg/μL) from a 1 mg tube supplied by the vendor (NHS groups can hydrolyze and store best when concentrated). Using 1 μL of the concentrated stock, create a working stock that is 1-5

µg/µL that can be used until consumed. It is best to store all NHS dye stocks dry at -20°C and keep stocks on ice when working with them at the bench. The concentrated DMSO stock can also be aliquoted and lyophilized (under mild heating due to the low DMSO vapor pressure) to avoid freeze-thaw cycles for a single large aliquot.

2) To a 40 µL aliquot of unconjugated secondary antibody (~1.3 mg/mL), add 5 µL of 1 M $NaHCO_3$ and 1-5 µg of dye using the appropriate amount of DMSO stock and mix well. Allow the solution to react for 30 minutes at room temperature. Note: It may be difficult to predict the coupling efficiency of the reaction depending on the freshness and storage conditions of the NHS stock solution. For this reason, we recommend running a few reactions in parallel with range of dye amount. For freshly prepared dye stocks, suggested amounts are 2-3 µg of Alexa Fluor 647 or Alexa Fluor 750 to achieve ~3-5 d/p, or 1-2 µg of Cy3B to achieve 2-3 d/p. However again, these values will need to be optimized on a case by case basis. A final consideration is to keep the total amount of DMSO in this reaction below 5% (v/v).

2.6.2 *Dye Purification and ratio determination*

3) During the 30 min reaction period, discard the NAP-5 column storage solution and then equilibrate the NAP-5 column by flowing through 10 mL of PBS.

4) When the 30 min reaction time is over, allow the remaining PBS to drain from the NAP-5 column. When the meniscus goes below the frit, evenly load the column with the antibody solution.

5) Once the antibody solution settles onto the column, add 650 µL of PBS to the column and discard the eluent.

6) When the meniscus again settles below the frit, add 300 μL of PBS and collect the eluent. This is the purified labeled antibody.

7) Measure the UV-Vis absorbance spectrum that contains the protein absorption peak at 280 nm as well as the full adsorption band of the selected fluorophore. Calculate the concentration of antibody, as well as the dye to protein labeling ratio (d/p), using the following equations:

$$[\mathrm{Antibody}](\mathrm{in\ mg/mL}) = \mathrm{MW}_{\mathrm{IgG}} * \frac{\mathrm{A}_{280}-(\mathrm{CF}\cdot \mathrm{A}_{\mathrm{max}})}{\varepsilon_{\mathrm{IgG}}} \qquad \text{Eq. 2.1}$$

$$^{\mathrm{d}}/_{\mathrm{p}} = \frac{\mathrm{A}_{\mathrm{max}} * \varepsilon_{\mathrm{IgG}}}{\epsilon_{\mathrm{dye}}(\mathrm{A}_{280}-(\mathrm{CF}\cdot \mathrm{A}_{\mathrm{max}}))} \qquad \text{Eq. 2.2}$$

The molecular weight $\mathrm{MW}_{\mathrm{IgG}} \approx 150{,}000$ g/mol, the antibody molar absorptivity $\varepsilon_{\mathrm{IgG}} \approx 200{,}000$ $\mathrm{M}^{-1}\mathrm{cm}^{-1}$, A_{280} is the dye absorbance at 280 nm, $\mathrm{A}_{\mathrm{max}}$ is the maximum dye absorbance, CF is the correction factor of the selected dye at 280 nm, and $\varepsilon_{\mathrm{dye}}$ is the dye molar absorptivity. For a complete list of reported values refer to manufacturer's data sheet.

2.7 Support Protocol 2: Thiol Imaging Cocktail for Alexa Fluor 647/Cy5/Cy3B/Atto 488

When Cy5 or Alexa Fluor 647 are illuminated with red light in the presence of a thiol, the fluorophore can form a covalent adduct with the thiol that is nonfluorescent (21). This nonfluorescent form can be returned to the fluorescent form either spontaneously or by illumination with ultraviolet light, and the cycling between nonfluorescent and fluorescent forms is the basis for photoswitching for these dyes used in STORM/PALM. To facilitate this photoswitching, a thiol-based imaging cocktail solution containing beta-mercaptoethanol (BME) and an enzymatic oxygen scavenger system are freshly prepared within ~1 hour of imaging. Many other fluorophores exhibit photoswitching in this same imaging cocktail, such as the other recommended fluorophores in this protocol, Alexa Fluor 750, Cy3B, and Atto 488 (18). Red- and near infrared-absorbing cyanine fluorophores also photoswitch well in a phosphine-based imaging cocktail, which in particular boosts the photon output of Alexa Fluor 750, and is described in Support Protocol 3 (19). A further discussion of photoswitching and imaging cocktails is contained below.

Materials List:

Oxygen scavenger stock solution (GLOX)

- Glucose Oxidase from *Aspergillus Niger* (Sigma, G2133)
- Catalase from Bovine Liver (Sigma, C100)

1M Tris buffer pH 8

50% w/v Glucose solution

Beta-mercaptoethanol (BME, Sigma, M6250)

Phosphate buffered saline (PBS), pH 7.4

Storage solution

2.7.1 *Oxygen Scavenger stock solution (GLOX) preparation*

1) Mix 14 mg glucose oxidase enzyme powder and 50 µL catalase suspension in 200 µL PBS. Centrifuge the reaction and transfer supernatant to a fresh tube and discard the pellet if present. If desired, snap-freeze GLOX aliquots in liquid nitrogen and store at -20°C, or store at 4°C and use for up to several weeks.

2.7.2 *Imaging Cocktail*

2) To create 1 mL of imaging cocktail, mix 680 µL H_2O, 200 µL 50% glucose, 100 µL of 1M tris, 10 µL BME and 10 µL GLOX. The total amount of imaging cocktail created can be adjusted

depending on needs, but use at least 250 μL per well when imaging. Typically the imaging cocktail is good for up to one hour, but can be used for longer if the chamber is sealed.

2.7.3 *Imaging Conditions*

3) Optimize the TIRF angle at low intensity and record conventional images if desired. To image Alexa Fluor 647 labeled samples, set a frame rate of 200 frames per second in a 128 x 128 pixel ROI with a 647 nm laser power density of 2.5 kW/cm^2. Power densities ranging from 1-5kW/cm^2 did not seem to adversely affect image quality (the power density was measure is EPI mode and therefore does not take into account the TIRF enhancement factor). The frame rate may be adjusted by varying the excitation power so that the average molecule on time roughly matches the acquisition time. When spontaneous blinking becomes sparse, the rate of blinking events may be increased by exposure to 405 nm light. At first, 405 nm activation must be applied sparingly ($<25\ W/cm^2$), to ensure that the blinking events are not too dense and overlapping. Sparse objects require extra care in this regards (e.g., imaging the centrosome) since only one or a few molecules may be detectable for frame without leading to ‘double localizations’ (described in more detail, below).

2.7.4 *Storage*

4) When finished imaging, remove the imaging cocktail and rinse with PBS. Store sample at 4°C in Storage solution to deter bacteria growth.

2.8 SUPPORT PROTOCOL 3: TCEP IMAGING COCKTAIL FOR ALEXA 750/CY7

The imaging cocktail containing TCEP (tris(2-carboxyethy)phosphine) is recommended for single color imaging of the infrared dye Alexa Fluor 750 or two color sequential imaging of

Alexa Fluor 750 then Alexa Fluor 647 [19]. Although the TCEP adduct formation mechanism has similarities to the thiol-based system, the dark state forms spontaneously immediately after addition of TCEP to the sample. For this reason, a slightly modified order of operations should be used when working with TCEP. Note that TCEP spontaneously degrades depending on storage conditions, so it is recommend to use a freshly opened ampule within at most 24 hours.

Materials List

GLOX oxygen scavenger stock solution (described in Support Protocol 2)
100 mM Methyl Viologen (MV, Sigma, 856177), freshly prepared
100 mM Ascorbic acid (AA, Fisher, A61), freshly prepared
50% w/v Glucose solution
1M Tris buffer pH 9
TCEP 0.5M pH 7 ampule (Sigma, 646547-10X1ML), used within 12 hours

2.8.1 *Imaging Cocktail*

1) Create 1 mL of imaging cocktail by mixing 500 µL H_2O, 200 µL 1M Tris pH 9, 200 µL 50% glucose, 10 µL of 100mM MV, 80 µL of 100 mM AA and 10 µL GLOX. The total amount created can be scaled appropriately, but apply at least 250 µL of the imaging cocktail per well. Note that this solution does not contain TCEP.

2.8.2 *TCEP Addition*

2) Before adding TCEP to the imaging cocktail, it is convenient to optimize the TIRF angle, and find a few regions of interest, save their stage positions for later reference, and record conventional widefield fluorescence images at low laser intensity if desired.

3) Just before imaging by STORM/PALM, and without removing the sample from the microscope, add a volume of the 0.5M TCEP stock to bring the total concentration of TCEP to 25 mM. For the suggested volume of 250 µL of imaging cocktail, it is necessary to add 12.5 µL of TCEP. Gently mix the solution by pipetting, being careful not to bump the sample or stage. The fluorescence intensity will decrease immediately.

2.8.3 *Imaging Conditions*

4) To image Alexa Fluor 750 labeled samples, set a frame rate of 30-60 frames per second in a 128 x 128 pixel ROI with a 750 nm laser power density of 2-6 kW/cm^2. When spontaneous blinking has become sparse, the number of blinking events can be increased by exposure to 405 nm light (<25 W/cm^2).

Reagents, Solutions, and Materials

Block/Perm Buffer

PBS Buffer pH 7.4

3% w/v Bovine Serum Albumin, IgG-free (Jackson, 001-000-161)

0.5% v/v Triton X-100 (Sigma, T8787)

Store at 4°C for up to 2 months

Extraction Buffer

1× PEM buffer (100 mM PIPES, 1 mM EGTA, 1 mM $MgCl_2$, final concentrations)

0.5% v/v TX-100

Freshly prepared using 10× PEM stock

Phosphate Buffered Saline pH 7.4 (PBS) (Invitrogen, 10010-023)

PEM Stock Buffer (10×), pH 7 stored at room temperature in the dark

1 M PIPES (piperazine-N,N′-bis(2-ethanesulfonic acid)

10 mM EGTA

10 mM $MgCl_2$

Adjust to pH 7

PFA only fixation solution

1× PEM buffer (100 mM PIPES, 1 mM EGTA, 1 mM $MgCl_2$, final concentrations)

3.2% paraformaldehyde (Electron Microscopy Science, #15714)

Freshly prepared. Heat the 32% PFA to 37°C to solubilize the polymerized form until the solution is clear.

PFA/GA fixation solution

1× PEM buffer (100 mM PIPES, 1 mM EGTA, 1 mM $MgCl_2$, final concentrations)

3.2% paraformaldehyde (Electron Microscopy Science, #15714)

0.1% glutaraldehyde (Electron Microscopy Science, #16300)

Freshly prepared using 50% glutaraldehyde and 32% PFA heated to 37° (see above).

Postfixation solution,

PBS buffer pH 7.4

0.25% glutaraldehyde

Freshly prepared using 50% glutaraldehyde

Storage solution

PBS buffer pH 7.4

3mM Sodium Azide

TCEP-based imaging cocktail

200 mM Tris pH 9

10% w/v glucose

1 mM Methyl Viologen (MV)

8 mM Ascorbic Acid (AA)

25 mM TCEP, added immediately before STORM/PALM acquisition

Freshly prepared using 1 M Tris pH 9, 50% glucose, 100 mM MV and 100 mM AA stock solutions.

Thiol-based imaging cocktail

100 mM Tris pH 8

10% w/v glucose

1% (v/v) 2-mercaptoethanol (BME)

1% (v/v) GLOX

Freshly prepared using 1 M Tris pH 8, 50% glucose, BME and GLOX stock (Support protocol 2)

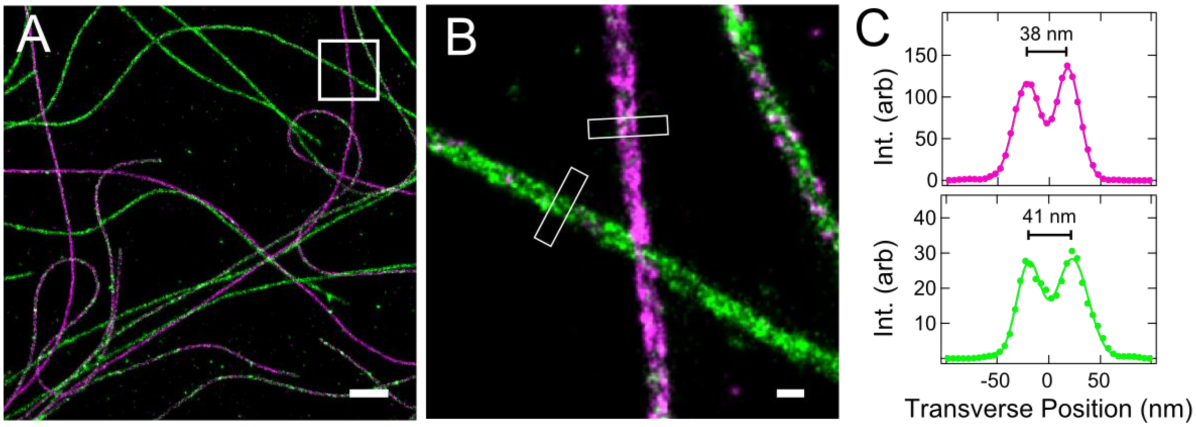

Figure 2.3 Two-color STORM image of fixed microtubules in BS-C-1 cells using the procedure described in the protocol. (A) Tyrosinated and detyrosinated microtubules stained with Alexa Fluor 750 (green) and imaged using the TCEP imaging cocktail, and Alexa Fluor 647 (magenta) imaged in the BME imaging cocktail, respectively. (B) Magnification of (A) showing the hollow structure in two microtubules in both color channels. The microtubule in the upper right exhibits labeling by both the tyrosinated and detyrosinated tubulin antibody, facilitating alignment. (C) Transverse profiles of hollow microtubules from (B) with fits to two Gaussian functions with 38 and 41 nm peak separation. Scale bars, 1 μm (A), and 100 nm (B).

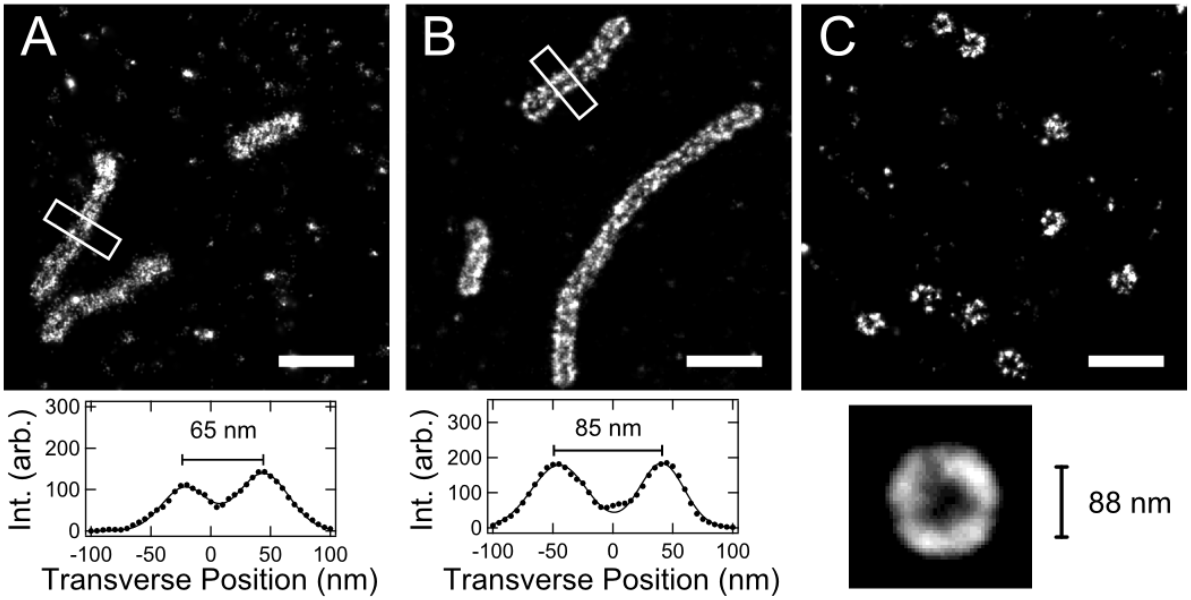

Figure 2.4 Single-color STORM images of cells stained for peroxisomes (PMP70) and clathrin in BS-C-1 cells. Peroxisomes labeled with (A) Alexa Fluor 750 and (B) Alexa Fluor 647 displaying hollow structure, imaged in the TCEP cocktail and BME cocktail, respectively. Below, the transverse profiles of (A) and (B) fit to two Gaussian functions with peak separation of 65 and 85 nm, respectively. (C) Clathrin labeled with Alexa Fluor 647 displaying toroidal structures. Below, an alignment of 36 clathrin-coated pits images, with diameter of ~88 nm. Scale bars, 500 nm.

2.9 COMMENTARY

2.9.1 *Background info*

Since its inception in 2006, STORM/PALM has advanced rapidly, with many variations now available, including multicolor imaging, 3D localization, and live-cell imaging. These tools are now routinely used to investigate a wide range of questions involving the nanoscale organization of biological systems including living cultured mammalian cells, yeast, bacteria, etc. (22–24). The greatly improved spatial resolution of STORM/PALM (~20-30 nm) places stringent demands on robust sample preparation, fluorophore properties, data acquisition, and data analysis. In this protocol, we described in detail the procedure for fluorescent immunostaining of representative cellular structures with the hope that suitable samples will allow practitioners the ability to troubleshoot their full imaging workflow.

Of course, immunological labeling is only one procedure out of many for labeling biological specimens for STORM/PALM. In fact, a large number of STORM/PALM experiments make use of photoswitchable (photoactivatable, photoconvertible, etc.) fluorescent proteins (FPs) (11, 25). Photoswitchable FPs have many benefits, including genetic encodability, a compact size (~3.5 nm across, compared to an antibody at 10-15 nm across), and compatibility with live-cell imaging. In terms of their fluorescent properties, the currently preferred photoswitchable FPs have a very good (i.e., low) duty cycle, which can potentially allow a high density of localizations, but emit fewer photons than the currently preferred organic dyes, which can make detection difficult in some cases, such as in the presence of a large fluorescent background signal (13). Additional challenges facing photoswitchable FPs include the lack of good multicolor imaging options, but overall it should be stressed that fluorescent protein approaches to STORM/PALM are an excellent option and in many ways possess complementary benefits and limitations. A labeling approach which has grown substantially in recent years utilizes genetically encoded reactive protein tags, such as SNAP tag or Halo tag, and others, that can react with or bind to a ligand attached to a small organic fluorescent dye (26, 27). Another area of active research in a number of labs uses very small peptide tags that are recognized by a co-expressed enzyme that can ligate a fluorophore to the small peptide (28, 29). As the field moves forward, these technologies and possibly new approaches will provide practitioners a wealth of powerful labeling tools.

2.9.2 *Critical Parameters*

Sample preparation for fixed specimens with STORM/PALM revolves around preservation of structure and good labeling with appropriate STORM/PALM fluorophores. Structure preservation and labeling are often at odds with one another when using immunostaining approaches, and this central tradeoff can occupy a large amount of time when optimizing protocols for a specific stain. This was evident in the extraction procedure which can improve labeling for some structures that survive the process (e.g., microtubules) but destroy other structures (e.g., mitochondria), as shown in Figure 2.2A. Fixation by glutaraldehyde, which is well known from electron microscopy for its ability to help preserve ultrastructure in specimens by crosslinking, may compromise labeling due to two reasons. First, quite a few antibodies are unable to recognize their target proteins once the target proteins have been treated with GA (or PFA/GA). Second, well-preserved specimens can hinder penetration of antibodies, especially in tissue or organisms.

Specificity of labeling is another critical parameter, and is somewhat at the mercy of the antibodies chosen. Many antibodies have nonspecific binding or weak binding to the proteins of interest, and searching for high-affinity and high-specificity antibodies can be time-consuming and expensive. Furthermore, multi-color labeling requires a little additional care to avoid crosstalk from secondary antibodies recognizing closely-related species. For instance, use of primary antibodies raised in rat and mouse to label two proteins of interest may produce crosstalk with anti-rat and anti-mouse secondary antibodies having some affinity for the other primary. Antibody crosstalk can be prevented to a large extent by use of antibodies that have been cross adsorbed to have minimal reactivity to other closely related species.

Assuming good labeling of the specimen, the choice of fluorophore(s) can make or break an experiment in STORM/PALM since image quality is strongly dependent on photoswitching properties of the fluorophores. Two key fluorophore parameters include *detected photons per localization* and the *duty cycle* (18). The number of detected photons per localization strongly influences the uncertainty of position determination, with an inverse square-root dependence of uncertainty on the number of detected photons (30, 31), and a low number of detected photons can therefore lead to a blurry image. The duty cycle, or fraction of time a fluorophore spends in a 'bright' state, limits the maximum density of fluorophores that can be detected. A low duty cycle allows many more fluorophores within a diffraction-limited region the ability to be individually detected, while a high duty cycle is more likely to result in 'double localization' artifacts where the position of more than one fluorophore is averaged together. When examining STORM/PALM images, one can assess the presence of double localizations by looking for localizations which connect two structures that are in fact distinct. In the case of microtubules, this would occur many times in typical images at the crossing of two microtubules, and the presence of excessive 'salt and pepper' at microtubule junctions is an indication of double localization artifacts. Some amount of these are inevitable based on the stochastic nature of the activation process, but these artifacts can be strong enough to artificially narrow structures or create apparent structures where none exists, and care must be taken in this regard when interpreting STORM/PALM images. While the preferred STORM/PALM fluorophores generally provide 1000-5000 detected photons per localization and duty cycles of 0.001 (0.1%) or better for a range of dyes spanning the visible and near-infrared, the preferred photoswitchable FPs provide about 1000 photons or less with a duty cycle of 10^{-6} and generally in a single channel (13, 18, 32). The recommended fluorophores for different spectral regions are Atto 488, Cy3B, Cy5/Alexa Fluor 647 or Cy7/Alexa Fluor 750, with Alexa Fluor 647 being the most robust and forgiving to beginner super resolution microscopist.

The photoswitching properties described above for organic STORM/PALM fluorophores generally require the use of a special additives to the imaging solution. Most of these contain an oxygen scavenging system consisting of two enzymes (glucose oxidase, catalase) together with a substrate (glucose) that can lower oxygen concentrations from ~300 µM to ~14 µM (33). The oxygen scavenger system helps to increase fluorophore photostability by lowering the rates of reaction with oxygen, and can influence the activation rate of some fluorophores (18). Additionally, the imaging cocktail may contain chemicals that are essential for photoswitching. For example, the cyanine dyes Alexa Fluor 647 or Cy5 exhibit a high photon output (~5000) and low duty cycle (0.001) in an imaging cocktail that contains a primary thiol, 2-mercapoethanol (BME), along with the oxygen scavenger system. It has been shown that the thiol reacts with the polymethine bridge of the cyanine dye which disrupts the conjugation and shifts the absorption wavelength from the visible to the ultraviolet (21). The conjugation is spontaneously recovered at a slow rate resulting in single molecule blinking events, and the activation rate may be further increased by exposure to UV light. Many other fluorophores exhibit photoswitching in this same imaging cocktail but may use other photoswitching mechanisms, including generation of long-lived radicals or two-electron reduced forms (18, 34–37), however it is difficult to match the performance of Alexa Fluor 647 in the visible regime for applications involving multicolor labeling. One dye that exhibits comparable photon output and duty cycle to Alexa Fluor 647 is the infrared dye Alexa Fluor 750 in an imaging cocktail containing the reducing agent (tris(2-carboxyethyl)phosphine) (TCEP) and the oxygen scavenger system. A dark state is formed spontaneously by a phosphine adduct on Alexa Fluor 750 bridge and fluorescence is recovered by activation with UV light (19). Additionally, the TCEP imaging cocktail contains a reducing and oxidizing system (ROXS) of methyl viologen and ascorbic acid to boost the photon output (38). The composition of the thiol-based and TCEP-based imaging cocktails are described in Support Protocols 2 and 3. Yet other imaging cocktails have been reported for use with one or more dyes, which we do not describe in detail here, but include the following: a mixture of ascorbic acid and methyl viologen (38); the use of the proprietary mounting medium Vectashield (39); the addition of cyclooctatetraene to the thiol imaging cocktail (40).

During imaging, two important and intertwined parameters are the camera frame rate and laser power density. The frame rate of the camera should roughly match the average fluorophore on time. If the fluorophore on time is much longer than an exposure, there will be less signal per frame and the comparably weak single molecule fluorescence signal would suffer from the additive effects of read noise. If the fluorophore on time is much shorter than an exposure, the duty cycle will in effect be artificially high since only one fluorophore can be detected within a single frame in a diffraction-limited volume. Very short on times relative to the camera exposure also lead to unnecessary detection of stray room or laser light which are collected during the full frame, rather than just during the period when the molecule is emitting. Since the laser power density typically has a strong effect on fluorophore on times, with higher power density leading to shorter on times and vice versa, both the camera frame rate and power density may be adjusted to find an optimal arrangement. The suggested power density for Alexa Fluor 647 imaging at 200 Hz is 1-5 kW/cm^2, whereas for 30-60 Hz imaging of Alexa Fluor 750 it is 2-6 kW/cm^2. The power density (power/area) can be found by shuttering down the illumination to a known area on the sample and then measuring the laser intensity in epifluorescence mode to find the ratio.

Although not directly related to resolution, drift correction can make or break an experiment. The trade of high resolution comes at the price of relatively poor temporal resolution. Even at high frame rates (200-500 Hz for Alexa Fluor 647) a typical image of microtubules constructed from 60k frames can take 2-5 minutes to acquire. During this time, lateral and axial drift arising from mechanical or thermal fluctuations cannot generally be ignored. Lateral drift can be corrected during post processing by correlation analysis, however axial drift must be corrected in real time using a feedback focus lock (6, 41)(42). Often, features such as the microtubule hollowness will be obscured until the reconstructed image is corrected for drift using post processing.

2.9.3 *Troubleshooting*

Table 2-1

Problem	**Possible Cause**	**Solution**
Extracted cells badly damaged or peeling off coverglass	Excessive extraction	Decrease extraction time
Fixed cells peeling	Shear forces	Gently pipette solutions against chamber walls, avoid sloshing and tapping chamber
Microtubules appear fractured	Extraction too aggressive GA degraded	Decrease extraction time Use fresh fixatives Use PEM buffer
High background	Excess primary antibody nonspecific adsorption Poor blocking	Titrate down primary antibody Use fresh BSA blocking solution
Structures appear dim	Low primary or secondary antibody concentrations Low d/p labeling ratio	Increase antibody concentrations Check or remake labeled secondary d/p ratio
Photobleaching under high laser power	Presence of oxygen	Remake GLOX with fresh enzymes
Hollow feature not apparent	Not enough localizations Stage drift Suboptimal d/p	Acquire more frames 2D correlation alignment Use secondary labeled with Alexa Fluor 647 at ~3-5 d/p
Single molecules appear dim	Low laser power Short integration	Increase power density Optimize TIRF angle Decrease integration time
Single molecules are too dense to localize	Initial frames are bright Activation too high	Discard initial frames Decrease 405 nm activation

2.9.4 *Anticipated Results*

With proper fixation and staining, microtubules are a robust and straightforward reference sample for super resolution imaging and an ideal sample for gaining an appreciation for the capabilities and limitations of STORM/PALM, in both one and two colors (**Figure 2.3**). We would like to stress that stained samples should be first validated using conventional fluorescence microscopy to determine if they are acceptable to be imaged by STORM/PALM. If the conventional images are poor, the STORM/PALM images will almost certainly be bad and it is not recommend to proceed to STORM/PALM imaging. For the first sample suggested in this protocol, the microtubules should appear continuous, with little fracturing, and should display a high signal with a low fluorescence background as shown in Figure 2.2A. If these criteria are met, resolving the microtubule hollow feature in STORM/PALM can be routinely achieved. With proper dye choice (Alexa Fluor 647 foremost, followed by Alexa Fluor 750) and imaging cocktail, sequential imaging of tyrosinated and detyrosinated microtubules, the hollow appearance may be observed in both channels (**Figure 2.3AB**), with a ~35-40 nm peak separation as shown previously (**Figure 2.3C**). The observed width of the microtubules is due both to the intrinsic width of the microtubules and the broadening caused by the antibody labels.

A second suggested reference sample are peroxisomes, which display a slightly larger hollow feature. Peroxisomes have been observed in a variety dimensions and morphologies (43), however in these samples from BS-C-1 cells, they appear elongated with ~60-90 nm transverse diameter as observed using both Alexa Fluor 750 and Alexa Fluor 647 in Figure 4AB. Fixation in the peroxisome-stained sample utilized PFA/GA without extraction in order to preserve the membrane; it is possible to perform a two color stain for microtubules and peroxisomes, however the hollow feature of the microtubules becomes more obscure due to the lack of extraction. The final suggested reference sample is clathrin which appear toroidal (**Figure 2.4C**) with diameters ranging from 100-200 nm (6).

2.9.5 *Time Considerations*

The total time for the full immunostaining protocol is approximately 3-4 hours, however depending on the complexity, the total planning and hands on time may vary and it is be best to allocate 5-6 hours for the beginner. If the user wishes to do multicolor fluorescence immunostaining in all eight wells using a variety of considerations, the procedure can quickly become overwhelming and we suggest setting out extra time initially to draw a cell staining "map" that contains a detailed plan for each individual well. Note that not all wells must be used in the same staining session, and rather may be fixed and stored in Storage solution (PBS + 3 mM sodium azide) for future staining (refer to Basic Protocol 1, Step 3). Cells are seeded 12-24 hours in advance and secondary antibody labeling (Support protocol 1) should be completed ahead of time so that there is no bottleneck in the cell staining procedure. An antibody labeling reaction and purification can be completed within one hour, including time for UV-vis characterization, and reactions can be run in parallel in order to save time.

Acknowledgements. This work was supported in part by the University of Washington and by a Burroughs-Welcome Career Award at the Scientific Interface. The authors would like to thank Tyler Chozinski, Dr. Honglin Li, and Lauren Gagnon for their help with antibody labeling and cell staining.

Conflict of Interest. The Authors declare no conflict of interest

2.10 REFERENCES

1. Hell, S., and J. Wichmann. 1994. Breaking the diffraction resolution limit by stimulated emission: stimulated-emission-depletion fluorescence microscopy. Opt Lett. 19: 780–782.

2. Gustafsson, M.G. 2000. Surpassing the lateral resolution limit by a factor of two using structured illumination microscopy. J Microsc. 198: 82–87.

3. Schermelleh, L., R. Heintzmann, and H. Leonhardt. 2010. A guide to super-resolution fluorescence microscopy. J Cell Biol. 190: 165–175.

4. Hell, S.W. 2009. Microscopy and its focal switch. Nat Methods. 6: 24–32.

5. Huang, B., H. Babcock, and X. Zhuang. 2010. Breaking the diffraction barrier: super-resolution imaging of cells. Cell. 143: 1047–1058.

6. Bates, M., B. Huang, G.T. Dempsey, and X. Zhuang. 2007. Multicolor super-resolution imaging with photo-switchable fluorescent probes. Science. 317: 1749–1753.

7. Rust, M.J., M. Bates, and X. Zhuang. 2006. Sub-diffraction-limit imaging by stochastic optical reconstruction microscopy (STORM). Nat Methods. 3: 793–796.

8. Betzig, E., G.H. Patterson, R. Sougrat, O.W. Lindwasser, S. Olenych, J.S. Bonifacino, M.W. Davidson, J. Lippincott-Schwartz, and H.F. Hess. 2006. Imaging intracellular fluorescent proteins at nanometer resolution. Science. 313: 1642–1645.

9. Hess, S.T., T.P.K. Girirajan, and M.D. Mason. 2006. Ultra-high resolution imaging by fluorescence photoactivation localization microscopy. Biophys J. 91: 4258–4272.

10. Shroff, H., H. White, and E. Betzig. 2008. Photoactivated localization microscopy (PALM) of adhesion complexes. In: Bonifacino JS, M Dasso, JB Harford, J Lippincott-Schwartz, KM Yamada, editors. Current Protocols in Cell Biology. Hoboken, NJ, USA: John Wiley & Sons, Inc.

11. Gould, T.J., V.V. Verkhusha, and S.T. Hess. 2009. Imaging biological structures with fluorescence photoactivation localization microscopy. Nat Protoc. 4: 291–308.

12. Rocha, S., H. De Keersmaecker, H. Uji-i, J. Hofkens, and H. Mizuno. 2014. Photoswitchable fluorescent proteins for superresolution fluorescence microscopy circumventing the diffraction limit of light. In: Engelborghs Y, AJWG Visser, editors. Fluorescence Spectroscopy and Microscopy. Totowa, NJ: Humana Press. pp. 793–812.

13. Wang, S., J.R. Moffitt, G.T. Dempsey, X.S. Xie, and X. Zhuang. 2014. Characterization and development of photoactivatable fluorescent proteins for single-molecule-based superresolution imaging. Proc Natl Acad Sci USA. 111: 8452–8457.

14. Dempsey, G.T. 2013. A user's guide to localization-based super-resolution fluorescence imaging. In: G. Sluder, D. E. Wolf, editors. Methods in Cell Biology. Academic Press. pp. 561–592.
15. van de Linde, S., A. Löschberger, T. Klein, M. Heidbreder, S. Wolter, M. Heilemann, and M. Sauer. 2011. Direct stochastic optical reconstruction microscopy with standard fluorescent probes. Nat Protoc. 6: 991–1009.

16. Manley, S., J. Gunzenhäuser, and N. Olivier. 2011. A starter kit for point-localization super-resolution imaging. Curr Opin Chem Biol. 15: 813–821.

17. Schnell, U., F. Dijk, K.A. Sjollema, and B.N.G. Giepmans. 2012. Immunolabeling artifacts and the need for live-cell imaging. Nat Methods. 9: 152–158.

18. Dempsey, G.T., J.C. Vaughan, K.H. Chen, M. Bates, and X. Zhuang. 2011. Evaluation of fluorophores for optimal performance in localization-based super-resolution imaging. Nat Methods. 8: 1027–1036.

19. Vaughan, J.C., G.T. Dempsey, E. Sun, and X. Zhuang. 2013. Phosphine Quenching of Cyanine Dyes as a Versatile Tool for Fluorescence Microscopy. J Am Chem Soc. 135: 1197–1200.

20. Wurm, C., D. Neumann, R. Schmidt, A. Egner, and S. Jakobs. 2010. Sample preparation for STED microscopy. In: Live Cell Imaging. Humana Press. pp. 185–199.

21. Dempsey, G.T., M. Bates, W.E. Kowtoniuk, D.R. Liu, R.Y. Tsien, and X. Zhuang. 2009. Photoswitching mechanism of cyanine dyes. J Am Chem Soc. 131: 18192–18193.

22. Jones, S.A., S.-H. Shim, J. He, and X. Zhuang. 2011. Fast, three-dimensional super-resolution imaging of live cells. Nat Methods. 8: 499–505.

23. Gahlmann, A., and W.E. Moerner. 2013. Exploring bacterial cell biology with single-molecule tracking and super-resolution imaging. Nat Rev Microbiol. 12: 9–22.

24. Ries, J., C. Kaplan, E. Platonova, H. Eghlidi, and H. Ewers. 2012. A simple, versatile method for GFP-based super-resolution microscopy via nanobodies. Nat Methods. 9: 582–584.

25. Patterson, G., M. Davidson, S. Manley, and J. Lippincott-Schwartz. 2010. Superresolution imaging using single-molecule localization. Annu Rev Phys Chem. 61: 345–367.

26. Hinner, M.J., and K. Johnsson. 2010. How to obtain labeled proteins and what to do with them. Cur Opin Biotech. 21: 766–776.

27. Jing, C., and V.W. Cornish. 2011. Chemical tags for labeling proteins inside living cells. Acc. Chem Res. 44: 784–792.

28. Wombacher, R., and V.W. Cornish. 2011. Chemical tags: Applications in live cell fluorescence imaging. J Biophotonics. 4: 391–402.

29. Fernández-Suárez, M., and A.Y. Ting. 2008. Fluorescent probes for super-resolution imaging in living cells. Nat Rev Mol Cell Bio. 9: 929–943.

30. Thompson, R.E., D.R. Larson, and W.W. Webb. 2002. Precise nanometer localization analysis for individual fluorescent probes. Biophys J. 82: 2775–2783.

31. Mortensen, K.I., L.S. Churchman, J.A. Spudich, and H. Flyvbjerg. 2010. Optimized localization analysis for single-molecule tracking and super-resolution microscopy. Nat Methods. 7: 377–381.

32. Chozinski, T.J., L.A. Gagnon, and J.C. Vaughan. 2014. Twinkle, twinkle little star: photoswitchable fluorophores for super-resolution imaging. FEBS Lett. 588: 3603–3612.

33. Aitken, C.E., R.A. Marshall, and J.D. Puglisi. 2008. An oxygen scavenging system for improvement of dye stability in single-molecule fluorescence experiments. Biophys J. 94: 1826–1835.

34. Kottke, T., S. van de Linde, M. Sauer, S. Kakorin, and M. Heilemann. 2010. Identification of the product of photoswitching of an oxazine fluorophore using Fourier transform infrared difference spectroscopy. J Phys Chem Lett. 1: 3156–3159.

35. van de Linde, S., I. Krstić, T. Prisner, S. Doose, M. Heilemann, and M. Sauer. 2011. Photoinduced formation of reversible dye radicals and their impact on super-resolution imaging. Photoc Photobio Sci. 10: 499.

36. Fölling, J., M. Bossi, H. Bock, R. Medda, C.A. Wurm, B. Hein, S. Jakobs, C. Eggeling, and S.W. Hell. 2008. Fluorescence nanoscopy by ground-state depletion and single-molecule return. Nat Methods. 5: 943–945.

37. Heilemann, M., S. van de Linde, A. Mukherjee, and M. Sauer. 2009. Super-resolution imaging with small organic fluorophores. Angew Chem Int Ed. 48: 6903–6908.

38. Vogelsang, J., T. Cordes, C. Forthmann, C. Steinhauer, and P. Tinnefeld. 2009. Controlling the fluorescence of ordinary oxazine dyes for single-molecule switching and superresolution microscopy. Proc. Natl. Acad. Sci. 106: 8107–8112.

39. Olivier, N., D. Keller, V.S. Rajan, P. Gönczy, and S. Manley. 2013. Simple buffers for 3D STORM microscopy. Biomed Opt Express. 4: 885.

40. Olivier, N., D. Keller, P. Gönczy, and S. Manley. 2013. Resolution doubling in 3D-STORM imaging through improved buffers. PLoS ONE. 8: e69004.

41. Huang, B., W. Wang, M. Bates, and X. Zhuang. 2008. Three-dimensional super-resolution imaging by stochastic optical reconstruction microscopy. Science. 319: 810–813.

42. McGorty, R., D. Kamiyama, and B. Huang. 2013. Active microscope stabilization in three dimensions using image correlation. Opt Nanoscopy. 2: 3.

43. Smith, J.J., and J.D. Aitchison. 2013. Peroxisomes take shape. Nat Rev Mol Cell Bio. 14: 803–817.

Chapter 3. EXTENDED-DEPTH 3D SUPER-RESOLUTION IMAGING USING PROBE-REFRESH STORM

3.1 PREFACE

There is great interest in expanding the multiplexing tool kit for fluorescence microscopy. This is because cells express a large number of different interacting proteins. Since the functional basis of the cell is the protein, understanding their spatial organization is critical to understanding their function. For example, if many proteins were imaged in a cancerous tissue, the information could be used to phenotype the cancerous cells and design individualized cancer treatment. However, imaging more than five markers is challenging due to limitations of the fluorophores used. If multiplexing is achieved spectrally, it is important to use dyes which have well spectrums in order to avoid cross talk. Typically, this is limited to only 5 from the near infrared to the ultra-violet (750,650, 560, 488,405 nm). Restrictions on multi-plexing are further restricted if practitioners wish to obtain super-resolved images of their samples, because oftentimes these techniques rely on special excited-state properties of the fluorophore and utilize high laser powers which cause rapid photobleaching.

In the case of SMLM, there one dye, Alexa 647, that produces the best images because it has the most ideal photophysical properties compared to all the others. Practically this implies that if another dye is used, resolution and image quality will inevitably be worse compared to Alexa

647. This means that practitioners are forced to make compromises if they want to spectrally multiplex, because only one channel can produce the best possible image.

Additionally, the high laser powers used in SMLM cause rapid photobleaching, and restricts 3-dimensional imaging because focal planes acquired late in the imaging sequence are photobleached before they can be imaged. This makes it challenging to image deep into specimens, while maintaining high image quality for every focal plane. Consequently, most applications of SMLM are near the coverslip surface (< 600 nm).

In this chapter I present a method called probe-refresh STORM (prSTORM) which addresses both of these challenges. Instead of spectrally multiplexing, a single dye is covalently attached to a reporter oligonucleotide, which is complimentary to unique DNA barcodes conjugated to antibodies. In this scheme, the reporter oligonucleotide can hybridize to its corresponding barcode and be imaged. Then the fluorescence can be removed, and the practitioner can choose to image the same set of proteins again (if photobleaching was problematic), or move on to the next protein in the sequence.

We demonstrated the efficacy of prSTORM by imaging the endoplasmic reticulum and mitochondria in three dimensions at depths > 1 um. Next we show that this technique can be used for 3-D multiplexing by acquiring 3-D images of the endoplasmic reticulum, mitochondria, and microtubules in sequence.

I was deeply involved with all aspects of this project. 3-D imaging calibration scripts were originally written by A.R. Halpern, and I extended and refined the scripts for use in this application. I was also deeply involved in sample preparation. I contributed by developing a buffer that prevents non-specific binding, and by optimizing our sample preparation techniques to utilize reporter oligonucleotides and DNA-conjugated antibodies.

The following material in this chapter is reproduced with permission from:

Lin, D., L.A. Gagnon, **M.D. Howard**, A.R. Halpern, and J.C. Vaughan. 2018. Extended-Depth 3D Super-Resolution Imaging Using Probe-Refresh STORM. Biophys. J. 114: 1980–1987

3.2 ABSTRACT

Single-molecule localization microscopy methods for super-resolution fluorescence microscopy, such as STORM (stochastic optical reconstruction microscopy), are generally limited to thin three-dimensional (3D) sections (≤600 nm) due to photobleaching of molecules outside the focal plane. Although multiple focal planes may be imaged prior to photobleaching by focusing progressively deeper within the sample, image quality is compromised in this approach because the total number of measurable localizations is divided between detection planes. Here we solve this problem by developing an imaging method, which we call probe refresh STORM (prSTORM), that allows bleached fluorophores to be straightforwardly replaced with non-bleached fluorophores. We accomplish this by immunostaining the sample with DNA-conjugated antibodies and then reading out their distribution using fluorescently-labeled DNA reporter oligonucleotides that can be fully replaced in successive rounds of imaging. We demonstrate that prSTORM can acquire 3D images over extended depths without sacrificing the density of localizations at any given plane. We also show that prSTORM can be adapted to obtain high-quality, 3D multichannel images with extended depth that would be challenging or impossible to achieve using established probe methods.

3.3 INTRODUCTION

Cells are dense, three-dimensional (3D) collections of molecules which are highly organized on the nanometer scale. Observing this nanoscale organization is crucial to understanding how cells function, but conventional fluorescence microscopy methods are unable to resolve objects closer together than ~250 nm due to the diffraction of light. To overcome this challenge, there has been a sustained interest in the development of super-resolution microscopy techniques that can maintain the high molecular specificity of fluorescence microscopy while allowing researchers to surpass the diffraction limit of visible light (1–4). Among these, single molecule localization microscopy (SMLM) techniques such as stochastic optical reconstruction microscopy (STORM) and photo-activated light microscopy (PALM) in their typical implementations achieve a spatial resolution of ~30 nm laterally and ~60 nm axially (1, 3, 5).

A range of approaches have been developed for 3D SMLM (6–10), but the easiest and most widespread of these uses a cylindrical lens to induce astigmatism in the detection path such that the ellipticity of single-molecule localizations can be used to determine the height of the molecules within the sample (6). However, in typical experiments where high numerical aperture oil immersion objective lenses are used to image into water based samples, substantial spherical aberration is incurred and the distal half of the focal depth in astigmatism imaging has notably poorer spatial resolution (11). While the aberrations can be mitigated by using adaptive optics (5) or index matching solutions (11), these are either costly or can compromise key focus lock systems that require refractive index contrast at the coverglass-water interface to function. Instead, a simple solution is to only accept localizations from the proximal half of the focal depth and to scan this high resolution portion of the focal plane through the sample in order to extend the depth range of imaging (11). Unfortunately, this focal plane scanning process compromises the spatial resolution by dividing up the total localizations achievable among all focal planes (i.e., it lowers the localization density for any given plane), and it particularly degrades the resolution of focal planes imaged later in the process since they are partly photobleached during the imaging of other focal planes. There is thus a need for extended depth 3D SMLM methods which are easily implemented and can overcome the combined challenges of spherical aberration and photobleaching.

A second major challenge in SMLM is a lack of dyes across the visible spectrum which have excellent photoswitching for multichannel imaging. Methods using sequential rounds of staining and bleaching partially circumvent this problem by using the excellent fluorophore Alexa Fluor 647 (or its close structural relatives such as Cy5) multiple times, but full restaining has prohibitively long sample preparation times (12–14). A different sequential imaging strategy termed DNA-PAINT (points accumulation for imaging in nanoscale topography) generates SMLM data from transient binding and unbinding of fluorophore labeled oligonucleotides that are complementary to oligonucleotides decorating the specimen (15, 16). Although DNA-PAINT does not require photoswitching and is therefore compatible with many fluorophores across the visible spectrum, its use of diffusing fluorescent probes creates high background signal unless low probe concentration and very low frame rates (~20 Hz) are used (16–18). More recently, new methods to streamline these processes utilizing DNA exchange probes have been introduced, making multichannel SMLM more accessible (19, 20), although multichannel imaging continues to be a challenge for many SMLM applications.

Here we present a method to refresh fluorescent probes on specimens to enable robust, multilayer 3D STORM over extended depths without compromised performance in any focal plane. We term this approach probe refresh STORM (prSTORM). We further demonstrate that the technique can be extended to multichannel imaging with uniform, high resolution in each channel, by multiple uses of the same fluorophore targeted to different structures. Our technique utilizes refreshable DNA probes to circumvent challenges faced when imaging in three dimensions with SMLM. Importantly, prSTORM can be implemented with common super-resolution microscopes with no modifications, and thus has the potential to benefit the whole community of SMLM researchers.

3.4 RESULTS

We developed prSTORM by utilizing custom antibody conjugates that are covalently bound by several (3 to 4) single-stranded DNA (ssDNA) oligonucleotides (supplementary Table 3-1), each ~20 nucleotides (nt) in length (21–23). After immunostaining the specimen and treating it with a post-fixative, we exposed the specimen to a solution of pre-hybridized adapter and fluorescently-labeled reporter oligonucleotides (**Figure 3.1**). The ~80 nt adapter strand contains a barcode recognition sequence (BRS) that is complementary to the ssDNA-antibody on the specimen as well as three repeats of reporter docking sequence (RDS) that is complementary to the reporter strand (RS). Three repeats of the RDS were included in order to boost signal levels. This design allowed us to modify antibodies with several ~20 nt oligonucleotides rather than several ~60 nt oligonucleotides, in order to minimize any reductions of antibody affinity, while still targeting a sufficient number of fluorophores to each antibody molecule. The modular use of the adapter oligonucleotide was also convenient for multichannel prSTORM as described further, below.

Once labeled, the specimen is imaged in switching buffer (a deoxygenated solution containing a thiol; see methods) using astigmatism-based 3D STORM, the previous round’s adapter/reporter oligonucleotides are completely removed through a brief exposure (<30 sec) to hot water (~90 °C), fresh (unbleached) probes are hybridized (10 min), and the specimen is imaged at a new focal plane. The process is repeated for many cycles, with a period of ~30 minutes. Since our goal was to keep the higher resolution, ~300 nm layer of localizations beneath the focal plane, we advanced the focal plane by moving the objective ~300 nm per cycle (equivalent to ~210 nm in the cell due to focal shift (11)), taking care to ensure that each layer contains overlapping localizations along the axial dimension so that each slice can be properly aligned axially.

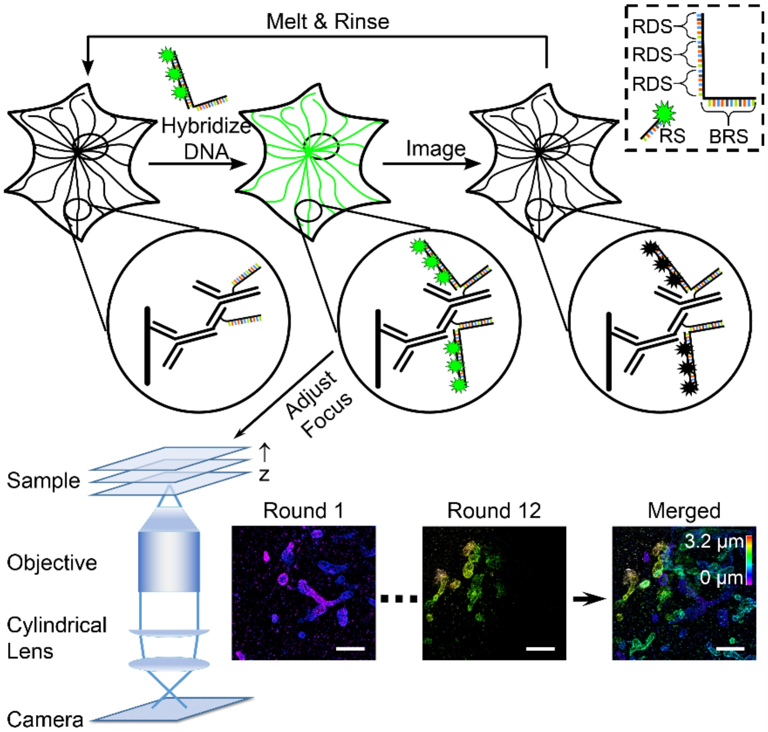

Figure 3.1 Workflow for prSTORM. A specimen immunostained with DNA-labeled secondary antibodies is exposed to a solution of pre-hybridized adapter and fluorescent reporter DNA, imaged by astigmatism 3D STORM, washed with hot water to remove photobleached adapter/reporter DNA, and a new focal plane is selected. This process is repeated many times in order to build up an extended depth 3D STORM image. The adapter oligonucleotide (inset, upper right) contains a barcode recognition sequence (BRS) which binds the antibody oligonucleotide as well as three reporter docking sequences (RDS) which can bind up to three fluorescently labeled reporter strands (RS). Scale bars: 2 μm

After acquiring all layers, we analyzed the separate movies, computationally corrected for spherical-aberration-induced axial localization error (11), extracted the ~300 nm sub-focal layer of localizations from each movie, and aligned all of the sections together to create a single multilayer 3D image. Overall, we found that the DNA labels on the secondary antibodies induced only mild spatial broadening of features compared to antibody labeling alone (**Figure 3.5**), as has also been seen in other recent work using conventional and DNA-conjugated antibodies (24, 25).

To demonstrate the ability of prSTORM to fully refresh the labels on the specimen without perturbation, we imaged the same specimen 10 times, each, with and without refreshing the probes (**Figure 2.2a-c**). The STORM images obtained with refreshed probes maintained the same number of localizations per round, while the non-refreshed specimen decreased substantially in each round due to photobleaching. We took efforts to make the comparison as fair as possible by using 50,000 frames for each round of imaging, by omitting 405 nm activation that may be variable during the acquisition, and by replacing the imaging cocktail switching buffer approximately every 15 minutes to limit potential interference caused by its decomposition over time (26). The difference between refreshed and non-refreshed is even more pronounced with longer movies (data not shown). In a second experiment, we found that even after 20 cycles of hybridization and melting at ~90 °C, there was negligible loss of signal and distortions were minimal (**Figure 3.6**). Together, these show that our procedure is able to efficiently refresh fluorophores, in principle an unlimited number of times, without perturbing the nanoscale structure of the specimen.

We next performed multilayer 3D STORM with and without probe refresh steps on the same sample (**Figure 3.2d-e**). For this comparison, we used gradually increasing 405 nm laser activation to obtain the highest number of localizations possible from our sample before photobleaching.

This “imaging to exhaustion” approach typically lasted ~400,000 frames per movie. In the probe refresh case, each of four layers was imaged to exhaustion with movies of ~400,000 frames, and we were able to reconstruct dense STORM images throughout the ~1.2 μm thickness of the specimen. In the non-refresh case, we divided the ~400,000 measurable frames among the four layers, and as expected the non-refresh sample was substantially sparser than in the refresh case, particularly for regions imaged later in the process since all layers are illuminated in each round of imaging, even those out of the focal plane. Thus, 3D prSTORM is able to substantially boost localization density over extended depths for multilayer imaging without suffering from loss of localization density due to photobleaching.

We extended our use of prSTORM to 1.5 microns of the endoplasmic reticulum (ER), acquiring 200,000 frames per layer (Figure 3), as well as 3.2 microns of the mitochondrial network (Figure S4). Without probe refresh steps we would be severely hindered by photobleaching, having only ~40,000 frames or less available per layer, which severely limits the achievable density of localizations per layer. The 3D view of the red box (**Figure 3.3b**) shows the thickest region of the ER and we see from the x-z and y-z slices that with probe refresh steps we obtain even axial resolution in all layers. We were also able to resolve holes in the “sheet-like” structures **(Figure 3.3c-f**) which are consistent with a recent report that suggests ER sheets are actually dense matrices of tubules (27).

We found that prSTORM was easily adapted for use with multichannel imaging. To do so, we prepared three different antibodies, each functionalized with a unique ssDNA oligonucleotide, and we purchased three different ~80 nt adapter nucleotides with orthogonal BRSs that can hybridize with the three antibody ssDNA oligonucleotides. By using the same RDS on each of these three adapter oligonucleotides, we were able to use the same fluorescently labeled reporter oligonucleotide for all three adapters. This modularity simplified our approach and only required the use of a single reporter oligonucleotide that was labeled with the excellent STORM fluorophore Alexa Fluor 647. Thus, each channel would be imaged with the superior fluorophore Alexa Fluor647 rather than using, for instance, multiple spectrally independent fluorophores which inevitably have one excellent fluorophore (typically Alexa Fluor 647 is used in the channel with the most demanding structure to image at high resolution) and one or more fluorophores with notably poorer performance(28).

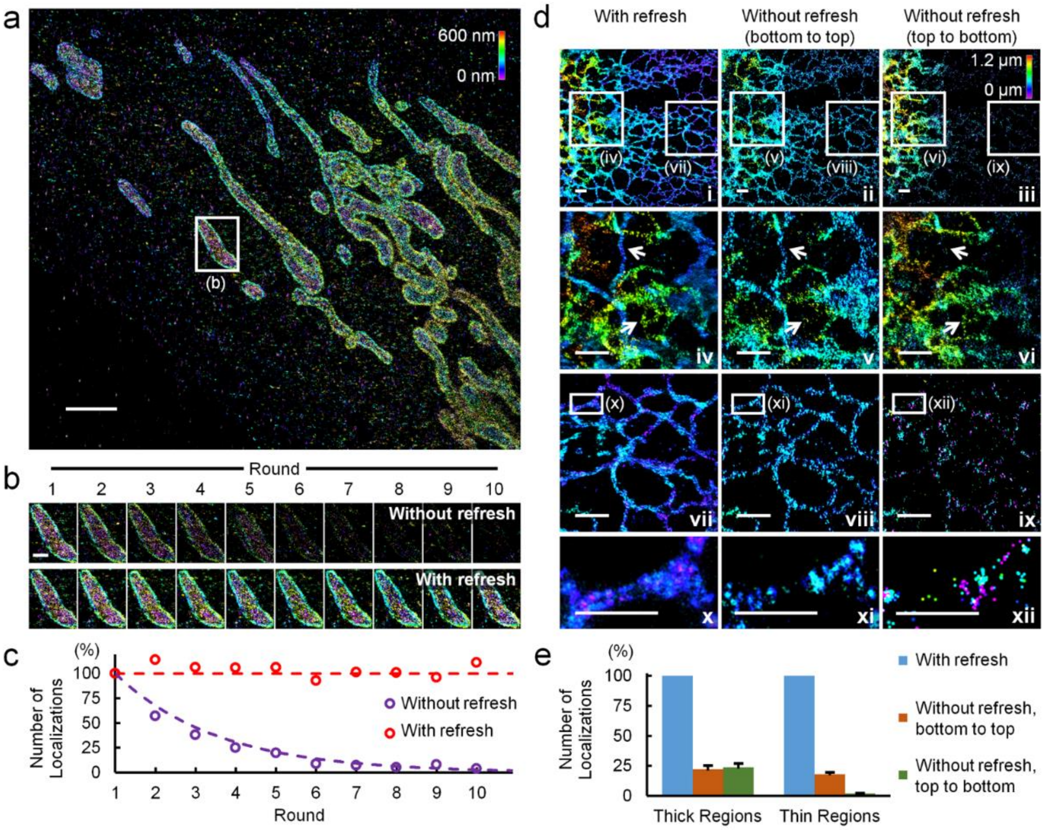

Figure 3.2 Improvement of single-molecule localization density due to probe refresh steps. **a)** 3D STORM image of mitochondria in a BS-C-1 cell immunostained for TOM20 and imaged in a single round (see also **Table S2** for additional details). **b)** Images of the same boxed mitochondrion in **a** across 10 sequential rounds of imaging with and without probe refresh steps and **c)** quantification of localization density across many mitochondria in the same data set (see also **Figure S3a**; the standard error of the mean was <5% of all mean values and was omitted from **c** for the sake of clarity). **d)** Four-layer extended-depth 3D STORM images, with and without probe

refresh steps, of the endoplasmic reticulum (ER) in a BS-C-1 cell expressing sec61β-GFP and immunostained for GFP. A higher number of localizations is achieved with probe refresh steps **i** than without, regardless of the scan direction **ii-iii**. Arrows in **iv-vi** indicate ER tubules at different depths within the cell which are only both visible when using probe refresh steps. Zoomed-in views **x-xii** show hollowness of ER tubules which is most prominent when using probe refresh steps. The contrast for image panels in **d** was adjusted individually to allow visualization of details in the comparably sparse non-refresh images. **e)** Number of localizations (mean ± SEM) for thick and thin regions from **i-iii** showing that probe refresh steps increase the number of localizations (localization numbers were normalized to the refresh data; see also **Figure S3b**). Scale bars: 2 µm (a), 1 µm (d i-ix), 500 nm (b, d x-xii).

The easily refreshable probes also allowed us to label all three targets simultaneously prior to sequential labeling and imaging of each structure, which simplified image registration among multiple channels.

We demonstrate multichannel/multilayer 3D prSTORM imaging of mitochondria, microtubules, and the ER by recording a 200,000 frame movie for each structure in each layer, with 405 nm activation, spanning an axial depth of ~800 nm (Figure 4). A high density of localizations was achieved on each structure over the depth of the specimen, giving high resolution images (Figure 4a-b) and we saw little evidence of crosstalk between the channels (Figure 4c). In a series of control experiments we found that our washing procedure was able to remove ≥98% of fluorescent signal from the specimen (data not shown) and we observed low crosstalk (<2-5%) between any of the channels (**Figure 3.9**). We observed that mitochondria generally localized to regions of the cell with “sheet-like” ER structures and are mostly absent from regions with only sparse ER tubules. In both the x-z and y-z slices we observe hollow mitochondria. Additionally, we are able to ascertain axial relationships among structures which are not easily discernable from the 2D projections, such as microtubules crossing just above and below ER sheets (**Figure 3.4b-c**).

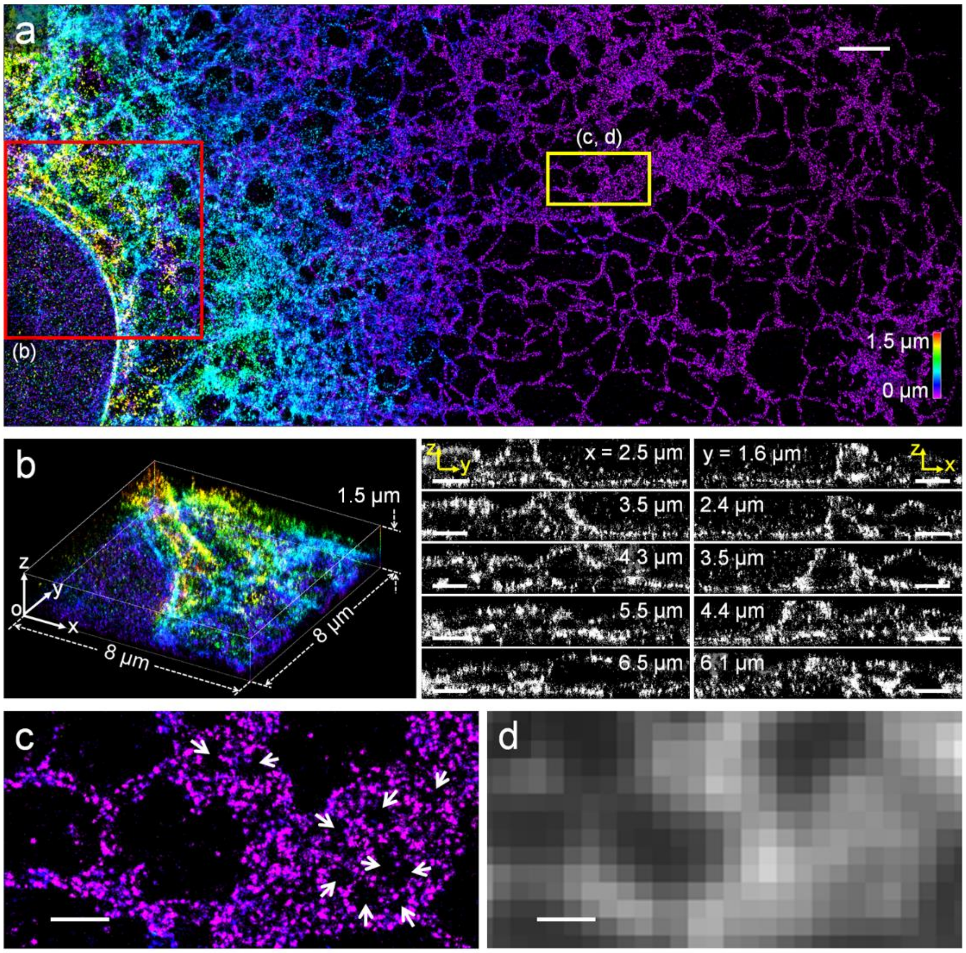

Figure 3.3 Extended depth 3D prSTORM image of the endoplasmic reticulum (ER) in COS-7 cells expressing sec61β-GFP and immunostained for GFP (see also **Table S2** for additional details). **a)** x-y projection colored in z. **b)** 3D rendered perspective view (left panel) of red box in **a**, with associated y-z sections (middle column), and x-z sections (right column). Section thickness: 100 nm. **c)** Zoomed-in view of yellow box in **a**. Arrows indicate gaps in the ER tubule matrices. **d)** Conventional fluorescence image corresponding to **c**. Scale bars: 2 µm (a), 1 µm (b), 500 nm (c-d). Positions are indicated relative to the origin "o" shown in panel **b**

3.5 DISCUSSION

We have described and demonstrated prSTORM, a new approach for extended depth single-molecule localization microscopy which uses probe refresh steps to circumvent limits otherwise caused by photobleaching of fluorophores on the specimen. Our procedure for refreshing the probes is simple to implement and many cycles of melting, hybridization, and washing produced little to no detectable distortions on the sample. We showed that prSTORM extends the depth achievable by 3D STORM without sacrificing the density of localizations. Although we used astigmatism-based axial localization here, together with the collection of only the proximal half of localizations that are of higher spatial resolution (~300 nm range) to measure specimens up to 3.2 µm thick, we note that prSTORM can extend the depth achievable with any axial localization technique (29) by eliminating limitations previously imposed by photobleaching. We also showed that prSTORM extends straightforwardly to multichannel imaging over an extended depth range with excellent performance in each of the channels and low crosstalk.

DNA-PAINT uses transient binding of diffusing probes and can also be performed for very long periods without photobleaching, so it is worth comparing its performance with that of prSTORM. In DNA-PAINT, diffusing fluorescent probes contribute to a substantial background signal unless their concentration is kept relatively low. Because of this, frame rates for DNA-PAINT are generally quite low (~20 Hz), such that in a 30 minute period, a maximum of ~36,000 frames could be recorded. In contrast, photoswitching with Alexa Fluor 647 can be performed with frame rates of 100-1000 Hz. Here, with prSTORM, we recorded ~200,000 frames in ~17 minutes (at 200 Hz) with an additional ~11 minutes for melting, hybridizing probes, and washing, for a total of <30 min/cycle for 5-6 times more frames. Scientific CMOS (complementary metal-oxide-semiconductor) cameras are now routinely used for ~1000 Hz STORM, and would allow the prSTORM cycle time to be shortened to ~15 min for 200,000 frame movies, or would, for instance, allow 200,000 frame movies to be recorded in each of several regions of interest within 30 min. DNA-PAINT with a confocal microscope of whole cells has recently been reported, but only for a modest number of frames per focal plane (10,000-30,000), presumably due to the low frame acquisition rate of ~5 Hz (18). Beyond DNA-PAINT, other methods for sequential multichannel imaging have been demonstrated. In methods based on cyclic immunofluorescence (14), a specimen is immunolabeled against one protein using Alexa Fluor 647, imaged, and the fluorescent signal is removed by photobleaching of fluorophores, chemical bleaching of fluorophores, or removal of the antibodies by salt, heat, etc. (12, 14). After quenching the fluorescence, the specimen is removed from the stage, immunostained against second protein, and imaged. Each round of imaging takes at least an hour because the specimen must be incubated with primary and secondary antibodies, blocked, and quenched again (12, 13). prSTORM and other DNA-barcoding based methods (32) present a distinct advantage because the specimen can be completely labeled with all antibodies at the benchtop and then these can be read out sequentially using rapid DNA hybridization and melting steps performed on the microscope.

While the DNA-conjugated antibodies enable prSTORM, they also face some drawbacks. Preparation of the antibodies, while documented well (19, 20, 33, 34), takes a few days and time to gain familiarity with the reagents. The DNA antibody labels also modestly broaden features (24, 25) slightly beyond the use of secondary antibody labeling alone (**Figure 3.4**).

However, this DNA-induced broadening could be reduced in the future through some combination of the following: using shorter hybridizing sequences (~15 nt); using only two repeats of the reporter docking sequence; using 3’-labeled reporter oligos (with adapters); omitting use of the adapters and using 5’-labeled reporter oligos that bind directly to the antibody-linked oligonucleotide; or conjugating DNA to primary antibodies.

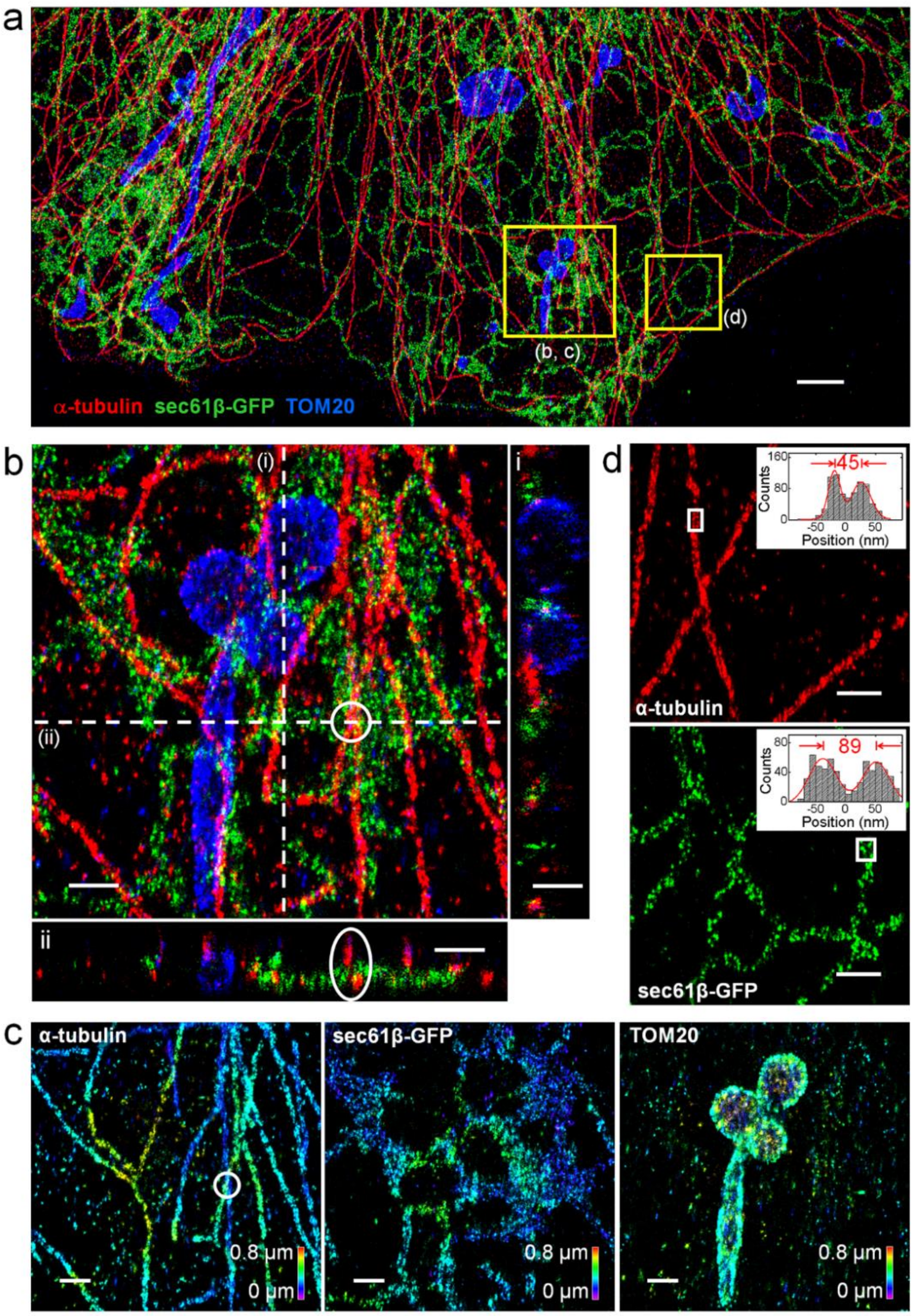

Figure 3.4 Three-channel, extended depth 3D prSTORM images of microtubules, mitochondria, and the endoplasmic reticulum (ER) in COS-7 cells expressing sec61β-GFP that were immunostained for α-tubulin, TOM20, and GFP (see also **Table S2** for additional details). **a)** Three-color x-y projection. **b)** Zoomed-in view of box in **a**, with orthogonal views of the dashed cross (100 nm section thicknesses). **c)** x-y projections colored in z for each structure (tubulin, ER, and mitochondria, respectively). White circle indicates the same sites marked in **b**. **d)** Zoomed-in view of box in **a**. Insets show cross-sectional profiles of the tubulin and ER channels, respectively. Scale bars: 2 μm (a), 500 nm (b-d).

Although it is not necessary, the entire process could be automated using computer-controlled focal plane scanning and a computer-controlled perfusion system for solution exchanges, etc., in order to boost throughput and to reduce human labor.

3.6 CONCLUSION

We have developed and characterized prSTORM which permits extended depth 3D super-resolution microscopy without incurring limitations resulting from photobleaching. We showed that prSTORM enables high resolution imaging throughout multiple layers of a specimen without loss of resolution due to reduced localization density and we also show that prSTORM can be easily extended to multiple channels with low crosstalk. The probe refresh method would potentially also benefit other 3D SMLM techniques, such as 4Pi interferometry, as well as stimulated emission depletion (STED) microscopy or structured illumination microscopy (SIM) so that a superior fluorophore or wavelength range could be used for multiple channels over extended depths.

3.7 AUTHOR CONTRIBUTIONS

L.A.G., M.D.H, D.L., and J.C.V. designed the experiments. L.A.G., M.D.H, and D.L. performed the experiments and analysis. A.R.H provided scripts for 3D calibration. L.A.G., M.D.H, D.L., and J.C.V. wrote the paper and all authors commented on the manuscript. J.C.V. supervised the project.

3.8 ACKNOWLEDGMENTS

This work is partially supported by the University of Washington (J.C.V.), a Burroughs-Welcome Career Award at the Scientific Interface (J.C.V.), NIH grant R01MH115767 (J.C.V), an NSF Graduate Research Fellowship DGE-1256082 (M.D.H.), the National Basic Research Program of China (No. 2015CB352005, D.L.), and the National Natural Science Foundation of China (No. 61775144, D.L.). The authors would like to thank Jonathan Perr (University of Washington, Seattle, WA) for his help with antibody labeling, Linda Wordeman (University of Washington, Seattle, WA) for access to a Lonza 4D X nucleofector system, and Tom Rapoport (Harvard Medical School, Boston, MA) for the Sec61β-GFP plasmid

3.9 SUPPORTING CITATIONS

Reference (35) appears in the Supporting Material.

3.10 SUPPORTING INFORMATION MATERIALS AND METHODS

3.10.1 *Reagents*

N-hydroxysuccinimide (NHS) ester; Alexa Fluor 750 NHS ester; 10× phosphate buffered saline (PBS); sodium chloride (NaCl); ethylene glycol-bis(beta-aminoethyl ether)-N,N,N',N'-tetraacetic acid tetrasodium salt (EGTA); magnesium chloride hexahydrate ($MgCl_2$); saponin; d-glucose anhydrous; 2-(N-morpholino) (MES) buffered saline packs; hydrochloric acid (HCl); sodium hydroxide (NaOH); Zeba spin desalting columns (100 kDa molecular weight cut off); disodium hydrogen phosphate (Na_2HPO_4); and tris base were purchased from Thermo Fisher Scientific (Waltham, MA). Sodium bicarbonate; dimethyl sulfoxide (DMSO); dimethylformamide (DMF); triton X-100; piperazine-N,N’-bis(2-ethanesulfonic acid) sesquisodium salt (PIPES); 2-hydrazinopyridine dihydrochloride (2-HP); sodium borohydride ($NaBH_4$); tRNA from baker’s yeast; 2-mercaptoethanol (BME); glucose oxidase from Asperigillus niger; catalase; and Ultra-0.5 mL centrifugal filters (100 kDa molecular weight cut off) were purchased from MilliporeSigma

(St. Louis, MO). N-succinimidyle 4-formylbenzoate (SFB) was purchased from TCI America (Portland, OR). Succinimidyl 6-hydrazinonicotinate acetone hydrazine (SANH) was purchased from Molecular Targeting Technologies (West Chester, PA). 10x Turbolink™ Catalyst Buffer was purchased from Solulink (San Diego, CA). Bovine serum albumin (BSA) was purchased from Rockland Immunochemicals (Limerick, PA). Aqueous solutions of 32% paraformaldehyde and 50% glutaraldehyde were purchased from Electron Microscopy Sciences (Hatfield, PA). Illustra Nap-5 columns, Sephadex G-25; and Hyclone Fetal Bovine Serum (FBS) were purchased from GE Healthcare (Chicago, IL). Vivaspin 500 centrifugal concentrators (5 kDa molecular weight cut off) were purchased from Vivaproducts (Littleton, MA). Commercially available mouse monoclonal anti-GFP epitope (1:200; IgG_{2a}; clone B-2; Santa Cruz Biotechnology (Dallas, Tx)); rabbit polyclonal anti-Tom20 epitope (1:200; clone FL-145; Santa Cruz Biotechnology); and rat monoclonal anti-alpha tubulin epitope (1:500; clone YL1/2; Thermo Fisher Scientific) were used for immunohistochemistry. Donkey anti-rat IgG (712-005-153); donkey anti-rabbit IgG (711-005-152); and donkey anti-mouse (715-005-151) were purchased from Jackson ImmunoResearch Laboratories (West Grove, PA). Microscope objective lens immersion oil (Laser liquid oil, code 5610) was purchased from Cargille Laboratories (Cedar Grove, NJ). Roswell Park Memorial Institute (RPMI) Medium 1640 [+] L-glutamine; Minimal Essential Medium (MEM) non-essential amino acids (NEAA); penicillin streptomycin; trypsin ethylenediaminetetraacetic acid (EDTA); and Dulbecco’s Modified Eagle Medium (DMEM) [+] 4.5 g/L D-glucose, [+] L-glutamine, and [+] 110 mg/L sodium pyruvate were purchased from Gibco via Thermo Fisher Scientific.

3.10.2 *Secondary Antibody Conjugation to Alexa Fluor 647 for standard immunohistochemistry (no DNA)*

Secondary antibodies for standard immunohistochemistry were labeled with Alexa Fluor 647 NHS ester at a labeling efficiency of 3-4 dyes per antibody according to the following procedure. 80 µL of secondary antibodies (~1.3 mg/mL) were incubated with 10 µL 1 M aqueous sodium bicarbonate (pH ~8.3) and 4-6 µg of Alexa Fluor 647 NHS ester at room temperature for 45 minutes. During the reaction we equilibrated a Nap-5 column with ~10 mL of PBS. After 45 minutes, we loaded the antibody mixture onto the column (~100 µL), we allowed the antibody mixture volume to sink into the frit, flowed 600 µL of PBS through the column (discarding the flow through), added 300 µL of PBS to the column and collected the 300 µL of eluate, which contained the Alexa Fluor 647 modified antibody. We then characterized using a UV-Vis spectrometer. Antibody concentrations and labeling ratios (dyes/protein) were determined using equations 3.1 and 2.2

$$[\text{Antibody}](\text{in mg/mL}) = \text{MW}_{\text{IgG}} \times \frac{A_{280} - (CF_{\text{Dye}} \times A_{\text{max,dye}})}{\varepsilon_{\text{IgG}}} \qquad \text{Eq. 3.1}$$

$${}^{d}/_{p} = \frac{A_{\text{max, dye}} \times \varepsilon_{\text{IgG}}}{\varepsilon_{\text{dye}}(A_{280} - (CF_{\text{dye}} \times A_{\text{max,dye}})} \qquad \text{Eq. 3.2}$$

For all antibody (IgG) labeling, MW_{IgG}=150,000 g/mol, ε_{IgG}=200,000 $M^{-1}cm^{-1}$, and A_{280}=Absorbance at 280 nm. For labeling with Alexa Fluor 647, $A_{\text{max,dye}}$=Absorbance at 650 nm, CF_{dye}=0.03, and ε_{dye}=239,000 M^{-1} cm^{-1}

3.10.3 *Preparation of DNA-Antibody Conjugates*

Secondary antibodies were conjugated to amine-modified DNA sequences using a modified version of a previously published protocol (33, 35) which is also described in detail, below. Overall the procedure consists of functionalizing amino-modified DNA with SFB, functionalizing antibodies with SANH, and coupling the SFB and SANH groups together to produce DNA-antibody conjugates.

Preparation of buffers. 250 mL of Buffer A (150 mM NaCl, 100 mM Na_2HPO_4, pH 7.4) was prepared by combining ~2.2 g NaCl and ~3.5 g Na_2HPO_4 and deionized water to a total volume of 250 mL. Buffer C was prepared using the same recipe and adjusted to pH 6.0. 2× MES, pH 5.0 was prepared by dissolving one packet MES buffered saline in deionized water to a total volume of 250 mL. The pH of buffers were adjusted to the indicated pH values using 10 M HCl or 10 M NaOH.

Modification of amino-oligonucleotide with SFB. DNA sequences containing 5’ amine modifications (5’amino C6) were purchased from IDT (Integrated DNA Technologies) in 0.1-1 µmol synthesis scale. Before opening, IDT tubes were centrifuged briefly to ensure DNA pellet is positioned at the bottom of the tube. After centrifugation, the DNA was dissolved in water at a concentration of 10 mM (10 nmol/µL). This stock was stored at -20 °C for future use. For a 200 nmol synthesis, 20 µL of stock DNA was diluted with 80 µL of Buffer A, yielding a final concentration of 2 mM DNA in Buffer A. ~1 mg SFB was suspended in 40 µL anhydrous DMSO (71.5 mM). 40 µL of the 71.5 mM SFB solution per 200 nmol DNA was suspended in Buffer A.

The solution was vortexed gently and allowed to react at room temperature for 2 hours. We removed excess SFB from the DNA using a Vivaspin 500 centrifugal filter by adding the reaction to the spin filter and bringing the total volume to ~500 µL using Buffer C. The reaction was centrifuged for 10 minutes at 13000 g. The flow-through was discarded and Buffer C was added to a volume of ~500 µL before centrifuging for 10 minutes at 13000 g. This process was repeated 3 additional times. After centrifuging we pipetted out the concentrate (~80 µL) and brought the total volume up to 100 µL using Buffer C, rinsing the filter with the volume of Buffer C we added to the concentrate. Solutions of SFB-modified DNA in Buffer C were stored at 4 °C for up to a year.

We quantified the amount of SFB-modified DNA by measuring the Molar Substitution Ratio (MSR). To do so, we prepared a working solution of 0.5 mM 2-HP in 0.1 M MES buffer, pH 5.0. This working solution is stable when stored at 4 °C and protected from light. Next, we prepared a 2-HP blank solution by adding 2 µL water to 48 µL 2-HP working solution and prepared a SFB-oligo MSR solution by adding 2 µL of purified oligo to 48 µL of 2-HP working solution. These two solutions we then vortexed and incubated at 37 °C for 1 hour. After incubating, there was often some condensation on the inner caps of the tubes, we collected the condensation by centrifuging tubes for ~15 seconds at 15000 g. Next, we added 450 µL water to each tube and briefly vortexed, this dilution brings absorption measurements to <1 on our instrument, it may need to be adjusted accordingly depending on reaction. The reaction with the modified DNA sample forms a hydrazine bond with absorption at 354 nm (molar extinction coefficient = 28,500 $M^{-1}cm^{-1}$). We used a UV-vis to quantify the substitution ratios, blanking the instrument with the prepared 2-HP blank solution. The concentrations of modified oligo and total oligo in solution we calculated using the 354 and 260 nm absorption peaks, respectively. Molar extinction coefficients for DNA sequences are provided by IDT. The ratio of these two concentrations yields the MSR. We typically achieve MSR values of 0.75 and modified DNA concentrations of

~1 mM using this method. The concentration of modified DNA stock is multiplied by 250 in equation 3.4 due to the two dilution steps.

$$\mathrm{MSR}=\frac{[\text{Modified oligo}]}{[\text{Total oligo}]}=\frac{\left[\dfrac{\mathrm{A354}}{28{,}500\frac{\mathrm{mol}}{\mathrm{L*cm}}}\right]}{\left[\dfrac{\mathrm{A260}}{\varepsilon_{\mathrm{oligo}}\frac{\mathrm{mol}}{\mathrm{L*cm}}}\right]} \qquad \text{Eq. 3.3}$$

$$[\text{Modified DNA}]_{\mathrm{Stock}} = \mathrm{MSR}\times\frac{\mathrm{A260}}{\varepsilon_{\mathrm{oligo}}\frac{\mathrm{mol}}{\mathrm{L*cm}}}\times 250 \qquad \text{Eq. 3.4}$$

Modification of antibodies with Alexa Fluor 750. Prior to modifying antibodies with SANH, we found it useful to label them with Alexa Fluor 750 at a d/p ratio of ~0.5 in order to quantify the final DNA-antibody conjugate labeling ratio which may otherwise be confounded by overlapping peaks due to antibody absorption at ~280 nm and DNA absorption at ~260 nm. We used a protocol similar to modification of antibodies with Alexa Fluor 647, described above, but with changes described here. We added ~3 µg of Alexa Fluor 750 NHS ester from a concentrated DMSO stock and 50 µL of freshly made 1 M aqueous sodium bicarbonate (pH ~8.3) to 200 µL of antibody (~1.3 mg/mL antibody in PBS), and incubated the reaction at room temperature (23 °C) for 45 minutes. During the reaction, we equilibrated a Nap-5 column by flowing through ~10 mL of Buffer A. After 45 minutes, we loaded the antibody mixture onto the column (~250 µL), we allowed the antibody mixture volume to sink into the frit, flowed 450 µL of Buffer A through the column (discarding the flow through), added 300 µL of Buffer A to the column and collected the 300 µL of eluate, which contained the Alexa Fluor 750 modified antibody. We characterized the d/p labeling as previously described for Alexa Fluor 647 modification, being sure to blank the UV-vis with Buffer A instead of PBS. For Alexa Fluor 750, $A_{\mathrm{max,dye}}$=Absorbance at 750 nm, CF_{dye}=0.04, and $\varepsilon_{\mathrm{dye}}$=290,000 $M^{-1}cm^{-1}$. This solution was stored at 4 °C for up to a month until ready to proceed with SANH modification. We typically achieved 0.5-1 d/p and an antibody concentration of ~0.0025 mM (0.37 mg/mL).

Modification of antibody with SANH. We dissolved 1 mg of SANH in 350 µL of DMF (9.8 mM) and stored in a desiccator at room temperature (23 °C) for up to 2 weeks. We added ~7.5 µL of the SANH solution to 300 µL of Alexa Fluor 750 modified antibody stored in Buffer A, vortexed, and incubated at room temperature for 2 hours. The molar excess of SANH over IgG can be adjusted to tune the number of DNA strands that bind to the IgG using equations 5 and 6. At a 100 molar excess of SANH (~7.5 µL SANH stock) we typically achieved 3-4 DNA/IgG. We found that higher DNA/IgG ratios could substantially disrupt antibody affinity.

$$[\mathrm{SANH}]_{\mathrm{final}}=[\mathrm{IgG}]\mathrm{mM}\times\mathrm{Molar\ Excess} \qquad \text{Eq. 3.5}$$

$$\mathrm{Volume}_{\mathrm{SANH}}=\frac{[\mathrm{SANH}]_{\mathrm{final}}\times\mathrm{Volume}_{\mathrm{IgG}}}{9.8\ \mathrm{mM}} \qquad \text{Eq. 3.6}$$

We added the appropriate volume of SFB-oligo to SANH-IgG along with $1/9^{th}$ of the total volume of Turbolink Catalyst Buffer (10×), vortexed the solution, and incubated at room temperature for 2 hours at room temperature (~23 °C) or overnight at 4 °C. For purification, we placed an Amicon Ultra 0.5 mL filter in a collection tube and applied the reaction solution to the filter. We added 1× PBS to the filter to make the total volume ~500 µL and centrifuged for 5 minutes at 14000 g. The flow-through was discarded and 1× PBS was added to bringing the total volume back up to ~500 µL and centrifuge again for 5 minutes at 14000 g. We repeated this step an additional three times. After, we pipetted out the concentrate and measured its volume. We brought the total volume up to 100 µL using PBS by first rinsing the filter with the volume to be added to the concentrate. We used the UV-vis to measure the 354 and 750 nm absorbance peaks and determined the DNA/IgG labeling ratio and IgG concentration using equations 9-11.

$$[\text{DNA-IgG}]=\frac{\text{A354}}{29{,}000\frac{\text{mol}}{\text{L*cm}}} \qquad \text{Eq. 3.7}$$

$$[\text{IgG}] = \frac{\text{A750}}{290{,}000\frac{\text{mol}}{\text{L*cm}}} \div \text{d/p} \qquad \text{Eq. 3.8}$$

$$\frac{\text{DNA}}{\text{IgG}}=\frac{[\text{DNA-IgG}]}{[\text{IgG}]} \qquad \text{Eq. 3.9}$$

3.10.4 *Cell Culture and Transfection*

BS-C-1 cells (ATTC CCL-26) were grown in RPMI supplemented with NEAA, penicillin streptomycin, and FBS. COS-7 cells (ATCC CRL-1651) were grown in DMEM supplemented with NEAA, penicillin streptomycin, and FBS. In some cases, COS-7 cells were transfected with Sec61β-GFP fusion plasmid using a Lonza 4D X Nucleofector system. First, COS-7 cells were grown to approximately 90% confluency and approximately 2-4 million were harvested using 0.25% Trypsin EDTA. The cells were mixed with 18 µL of SE cell supplement and 82 µL of SE nucleofection solution from Lonza and 2 µg/million cells of with Sec61β-GFP fusion plasmid. Then the cells were placed in the Lonza 4D nucleofector system and transfected using the DS-120 pulse code. Cells were then recounted and seeded into chambers with ~30,000 cells/well for ibidi 8-well chambers or ~11,000 cells/channel for ibidi µ-Slide VI 0.4 flow channels (~11,000 cells/channel), and incubated overnight.

3.10.5 *Cell Fixation*

All samples were fixed at 37 °C for 10 minutes in PFA/GA fixation solution containing 100 mM aqueous PIPES buffer pH 7, 1 mM EGTA, 1 mM $MgCl_2$, 3.2% paraformaldehyde, 0.1% glutaraldehyde, then reduced for 10 minutes with fresh, 10 mM aqueous sodium borohydride, and rinsed with PBS for 5 minutes. Prior to fixation, some specimens were subjected to a ~20 second extraction step with a solution of 100 mM aqueous PIPES buffer pH 7, 1 mM EGTA, 1 mM $MgCl_2$, which contained either 0.025% saponin or 0.5% triton X-100; see **Table 3-2** for additional details.

3.10.6 *Immunostaining*

All samples were incubated at room temperature for 30 minutes in block/perm solution containing PBS, 3% BSA, and 0.5% triton X-100. All samples were incubated for 30 minutes to overnight in block/perm solution containing primary antibodies. Standard immunohistochemistry samples containing no DNA were incubated for 30 minutes in block/perm solution containing secondary antibodies labeled with Alexa Fluor 647. DNA samples were incubated for 30 minutes with secondary antibody-DNA conjugates in DNA block/perm solution containing PBS, 3% BSA, 0.5% triton X-100 and 1 mg/ml yeast tRNA, and then rinsed for 5 minutes with PBS. All samples were post-fixed for 10 min in a solution containing PBS, and 0.25% glutaraldehyde. Adapter and reporter ssDNA were pre-hybridized for 10 min in DNA block/perm. Samples were incubated with pre-hybridized adapter/reporter solution at room temperature or 37 °C for 5-10 minutes followed by a 3 mL rinse with PBS.

3.10.7 *STORM setup and imaging*

Imaging was performed on a homebuilt STORM system constructed on an inverted microscope (Eclipse Ti-U, Nikon), equipped with a 100X 1.45NA oil objective (CFI Plan Apo λ, Nikon), a motorized stage (MS-2000 Flat-Top, Applied Scientific Instrumentation) and a custom-built focus lock module based on a piezoelectric objective lens nano-positioner (Nano-F100S, Mad City Labs) and an infrared laser diode (LP940-SF30, Thorlabs). The 647 nm illumination laser (2RU-VFL-P, MPB Communication) was controlled using an acousto-optical tunable filter (AOTF, Gooch & Housego). Oblique illumination (near total internal reflection) was employed to enable deep 3D imaging while maintaining a relatively low background. For 3D imaging, a cylindrical lens with a focal length of 1000 mm was introduced into the detection path to create astigmatism for axial localizations. Calibration data were collected before 3D imaging using 100-nm-diameter fluorescent beads (Molecular Probes) while scanning in the z direction. Samples were imaged in a freshly prepared switching buffer containing 10% glucose, 100 mM tris pH 8, 1% BME and 1% GLOX (glucose oxidase/catalase). Image stacks (also termed as “movies”) were captured using an electron-multiplying charge-coupled device camera (iXon+DU897, Andor) via custom acquisition software at 200 Hz for 50,000-400,000 frames with an illumination power density of ~3.5 kW/cm^2. In case of multichannel imaging, an initial reference image of all structures simultaneously labeled with the same dye using their corresponding adapter and reporter DNA oligonucleotides were obtained for registrations among channels. A 405 nm activation laser (OBIS LX, Coherent) was used to enhance the photoactivation rate of Alexa Fluor 647. An aspirator was used to perform on-stage liquid exchanges (see **Figure 3.10**).

3.10.8 *Data Analysis*

STORM images were generated using similar methods as previously described (3). Briefly, for 2D STORM, images of individual molecules were identified and fitted to a 2D Gaussian function to obtain the centroid coordinates (x_0, y_0), which were assigned the positions of the single molecules for reconstructing a STORM image. For 3D STORM, an elliptical Gaussian function was used instead. The lateral coordinates of molecules were determined in the same way using the Gaussian centroid coordinates, and the vertical coordinate (z) was calculated by comparing the Gaussian widths (w_x, w_y) to the calibration curves. Focal shift and spherical aberration corrections were carried out at each focal plane as described previously (4). Lateral and axial drift correction was then applied to the super-resolution image based on cross-correlations of adjacent subsets of localizations. For multilayer 3D images, localizations ~300 nm beneath the focal plane were accepted, while localizations above the focal plane were rejected due to their poorer spatial resolution resulting from spherical aberration correction. Prior to merging all layers together, alignments in three dimensions were carried out using a Fourier transform based cross-correlation method. To register images laterally, all images to be aligned were saved as high resolution x-y projections. Then the 2D cross-correlation between two adjacent layers was calculated and images were then aligned by translating all localizations by the displacement between the position of the cross-correlation peak and the origin. After lateral alignment, identical x-z slices of each movie were saved and x-z alignment was carried out using the same cross-correlation procedure. In some cases, lateral and axial registration processes were iterated to ensure good alignment in all three dimensions. In the case of multichannel registration, an image of all structures served as a reference image for alignment among channels. Here, all targets to be imaged were simultaneously labeled with the same dye using their corresponding adapter and reporter DNA sequences. Images in each channel in the same layer were aligned to the reference image using the same Fourier transform cross-correlation method, followed by multilayer alignment in each channel as in the case of single channel multilayer 3D imaging

3.10.9 *Supporting References*

1. Chen, F., P.W. Tillberg, and E.S. Boyden. 2015. Expansion microscopy. Science. 347: 543–548.

2. Expansion Microscopy. 2017. 22 Nov 2017. http://expansionmicroscopy.org/.

3. Huang, B., W. Wang, M. Bates, and X. Zhuang. 2008. Three-dimensional super-resolution imaging by stochastic optical reconstruction microscopy. Science. 319: 810–813.

4. Huang, B., S.A. Jones, B. Brandenburg, and X. Zhuang. 2008. Whole-cell 3D STORM reveals interactions between cellular structures with nanometer-scale resolution. Nat. Methods. 5: 1047–1052

3.10.10 *Supporting Figures And Tables*

Table 3-1 DNA Sequences

Secondary Antibody and Sequence 5’-3’ 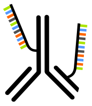	Adapter Sequence 5’-3’ 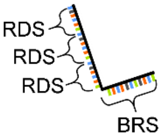	Reporter Sequence 5’-3’ 
Donkey anti Rat min Mouse /5AmMC6/GCATTACAGTCCTCATAAGT (LAG_010)	ACTTATGAGGACTGTAATGCTTAATGATACGGCGACCACCGATTAATGATACGGCGACCACCGATTAATGATACGGCGACCACCGA (LAG_013)	/5Alex647N/TCGGTGGTCGCCGTATCATT (P5A647JV)
Donkey anti Rabbit /5AmMC6/CCGAATACAAAGCATCAACG (LAG_007)	CGTTGATGCTTTGTATTCGGTTAATGATACGGCGACCACCGATTAATGATACGGCGACCACCGATTAATGATACGGCGACCACCGA (LAG_015)	/5Alex647N/TCGGTGGTCGCCGTATCATT (P5A647JV)
Donkey anti Mouse min Rat /5AmMC6/GACTACTGATAACTGGATTG (LAG_017)	CAATCCAGTTATCAGTAGTCTTAATGATACGGCGACCACCGATTAATGATACGGCGACCACCGATTAATGATACGGCGACCACCGA (LAG_016)	/5Alex647N/TCGGTGGTCGCCGTATCATT (P5A647JV)

Notes: Colors of the sequences in adjacent columns indicate complementarity. The code in parentheses below each sequence indicates the sequence name. Each adapter contains space for three reporter strands to bind, and all adapters bind to the same reporter strand. BRS: barcode recognition sequence; RDS: reporter docking sequence; RS: reporter stand; Dye: Alexa Fluor 647.

Table 3-2 Summary of sample preparation and imaging conditions.

Fig.	**Specimen**	**Extraction**	**Primary Ab** all 1-2 μg/mL	**Secondary Ab** all 8-12 μg/mL	**Adapter(s)**	**Rounds**[1]	**Thickness**	**Imaging Conditions**
1	COS-7 cell, wildtype	saponin	Rb x TOM20	D × Rb-LAG_007	LAG_015	13	3.2 μm	200 Hz, 100k frames/round, 100x 1.45 NA oil objective, 405 activation
2a-b	BS-C-1 cell, wildtype	none	Rb × TOM20	D × Rb-LAG_007	LAG_015	10 (b)	600 nm	200 Hz, 50k frames/round, 100x 1.45 NA oil objective
2d	BS-C-1 cell expressing Sec61β-GFP	none	Rb × GFP	D × Rb-LAG_007	LAG_015	4	1.2 μm	200 Hz, exhaustion[4], 100x 1.45 NA oil objective, 405 activation
3	COS-7 cell expressing Sec61β-GFP	saponin	Ms × GFP	D × Ms-LAG_017	LAG_016	9	1.5 μm	200 Hz, 200k frames/round, 100x 1.45 NA oil objective 405 activation
4	COS-7 cell expressing Sec61β-GFP	saponin	Rat × Tub Rb × TOM20 Ms × GFP	D × Rat-LAG_010 D × Rb-LAG_007 D × Ms-LAG_017	LAG_013 LAG_015 LAG_016	4×3 [2]	800 nm	200 Hz, 200k frames/round, 100x 1.45 NA oil objective 405 activation
S1	BS-C-1 cell, wildtype	triton	Rat × Tub	D × Rat-LAG_010	LAG_013	1	~600 nm (2D only)	200 Hz, 200k frames/round, 100x 1.45 NA oil objective 405 activation
S2	BS-C-1 cell, wildtype	triton	Rat × Tub	D × Rat AF647 D × Rat-LAG_010	N/A LAG_013	20	~600 nm (2D only)	500 Hz, 100k frames/round, 60x 1.2NA water objective 405 activation
S3a	BS-C-1 cell, wildtype	none	Rb × TOM20	D × Rb-LAG_007	LAG_015	10	600 nm	200 Hz, 50k frames/round, 100x 1.45 NA oil objective
S3b	BS-C-1 cell expressing Sec61β-GFP	none	Rb × GFP	D × Rb-LAG_007	LAG_015	4	1.2 μm	200 Hz, exhaustion[4], 100x 1.45 NA oil objective, 405 activation
S4	COS-7 cell, wildtype	saponin	Rb x TOM20	D × Rb-LAG_007	LAG_015	13	3.2 μm	200 Hz, 100k frames/round, 100x 1.45 NA oil objective, 405 activation
S5	COS-7 cell, wildtype	saponin	Rat × Tub Rb × TOM20 Ms × aTub	D × Rat-LAG_010 D × Rb-LAG_007 D × Ms-LAG_017	LAG_013 LAG_015 LAG_016 Reporter only	1×12 [3]	~600 nm (2D only)	200 Hz, 50k frames/round, 100x 1.45 oil objective

Notes: [1]Number of rounds, where each round consists of melting, hybridization, and washing steps (**Fig. 1**), but where the first round omits the melting step. [2]In Figure 4, “4×3” means 4 rounds for 3 channels. [3]In Figure 3.9, “1×12” means 1 layer for 12 cases. [4]“Exhaustion” here means imaging until nearly all the dyes were photobleached, typically at ~400,000 frames when gradual 405 nm laser activation was used during imaging.

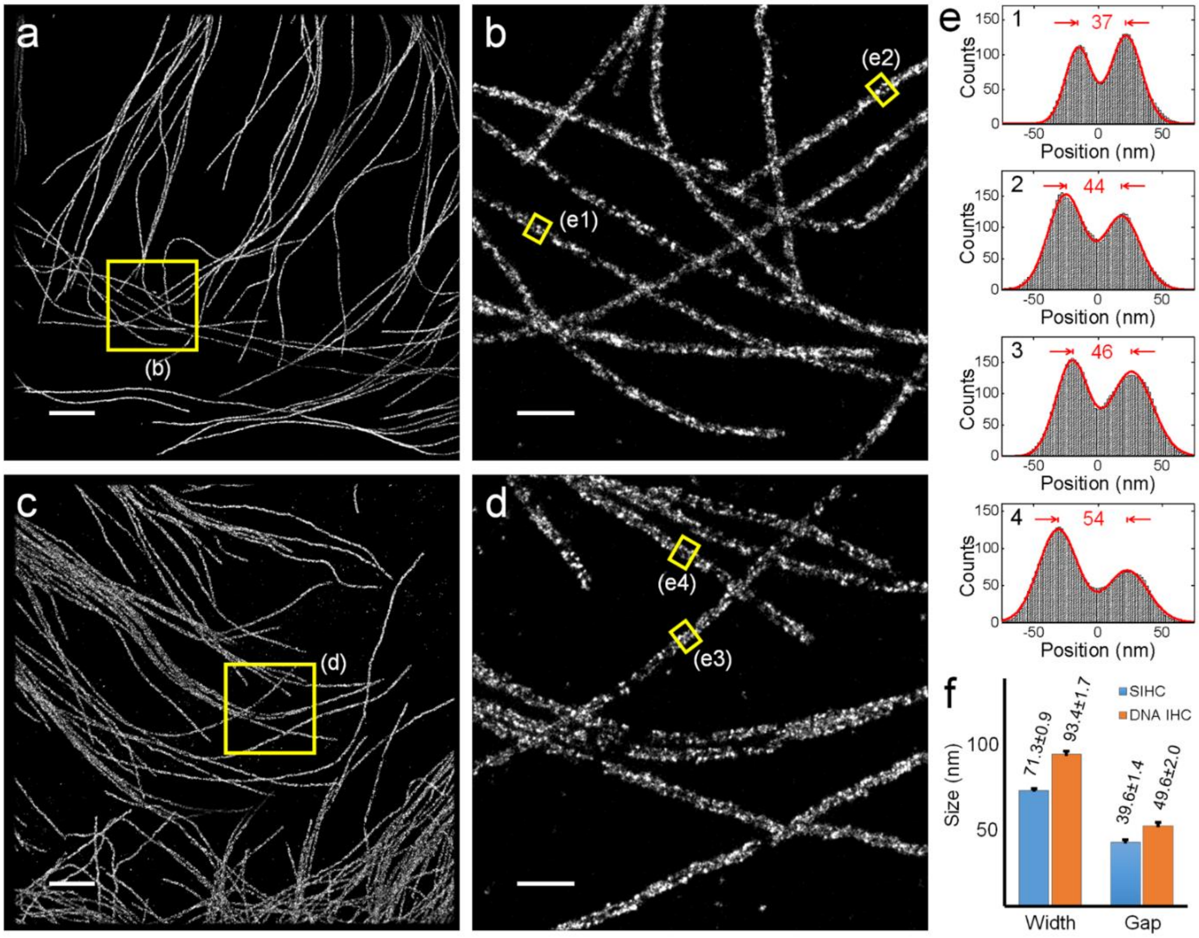

Figure 3.5 Comparison of tubulin immunostains in BS-C-1 cells using either standard fluorescent secondary antibody or DNA-conjugated secondary antibody. **a)** 2D STORM image using a standard fluorescent secondary antibody. **b)** Zoomed-in view of box in **a**. **c)** 2D STORM using a DNA-conjugated secondary antibody. **d)** Zoomed in view of box in **c**. **e)** Examples of histograms of number of localizations in cross-sections of microtubules in both cases for boxed regions in panels **b** and **d**. **f)** Statistical results on 59 cross-sections in **a** and 58 cross-sections in **c**. Data were expressed as mean ± standard error of the mean. Contrast has been adjusted individually in **a-d** for better visualization of the tubule structures; the number of localizations per unit length of microtubules was ~30% larger for standard fluorescent secondary antibodies compared to DNA-conjugated secondary antibodies. Scale bars: 2 µm (a, c), 500 nm (b, d).

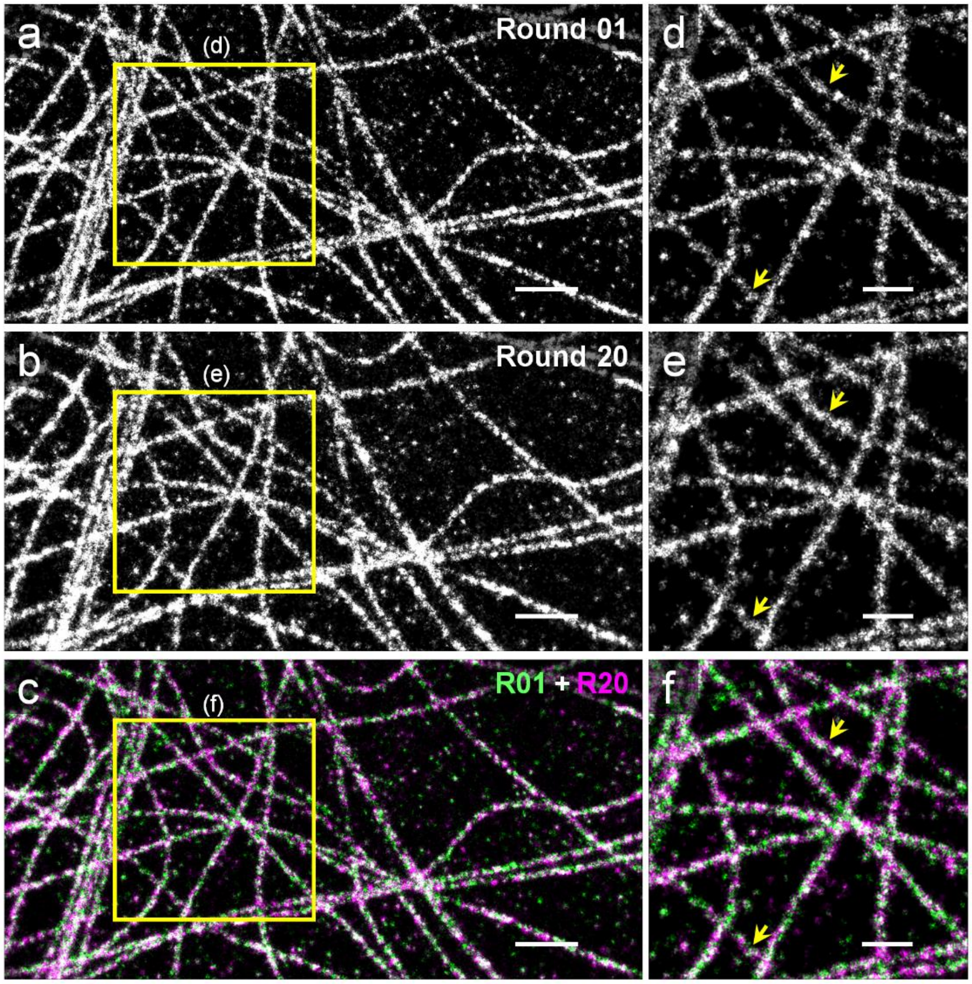

Figure 3.6 Assessment of structural preservation in prSTORM. **a)** 2D STORM image (Round 01) of microtubules in a BS-C-1 cell immunostained for α-tubulin. **b)** 2D STORM image (Round 20) of the same region after repeating 19 additional rounds of melting, hybridization, and washing. **c)** Overlay of panels **a** and **b. d-f)** Zoomed-in views of boxes in **a-c**. Scale bars: 1 µm (a-c), 500 nm (d-f). Arrows indicate two regions showing minor distortions after 20 rounds of melting, hybridization, and washing

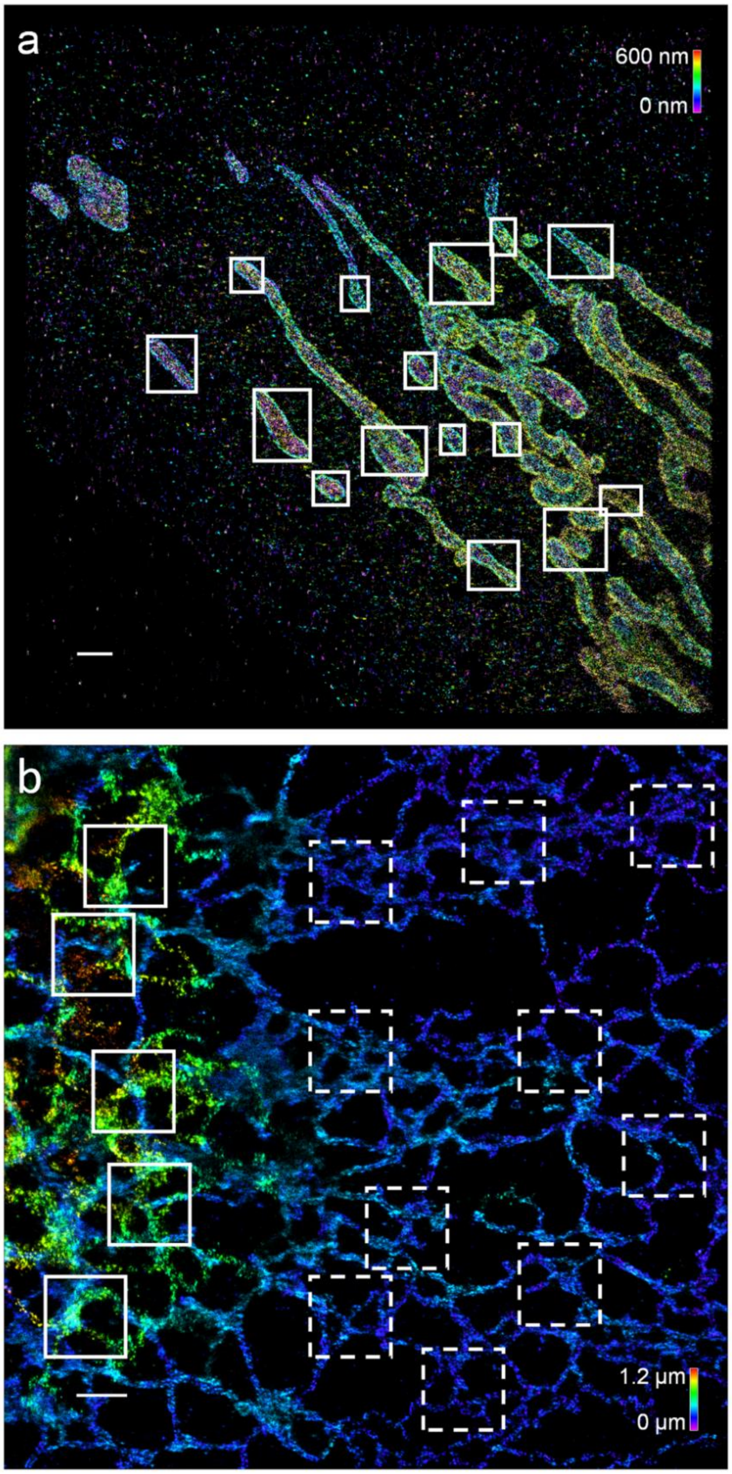

Figure 3.7 Regions of interest selected for statistical analysis shown in **Figure 2**. **a)** Positions and sizes of the 15 random regions for analysis in **Figure 2c**, i.e., in single-layer 3D STORM images of mitochondria with and without probe refresh steps. **b)** Positions and sizes of the 5 thick regions

(solid boxes) and 10 thin regions (dashed boxes) for analysis in **Figure 2e**, i.e., in 4-layer 3D STORM images with and without probe refresh steps. Scale bars: 1 μm

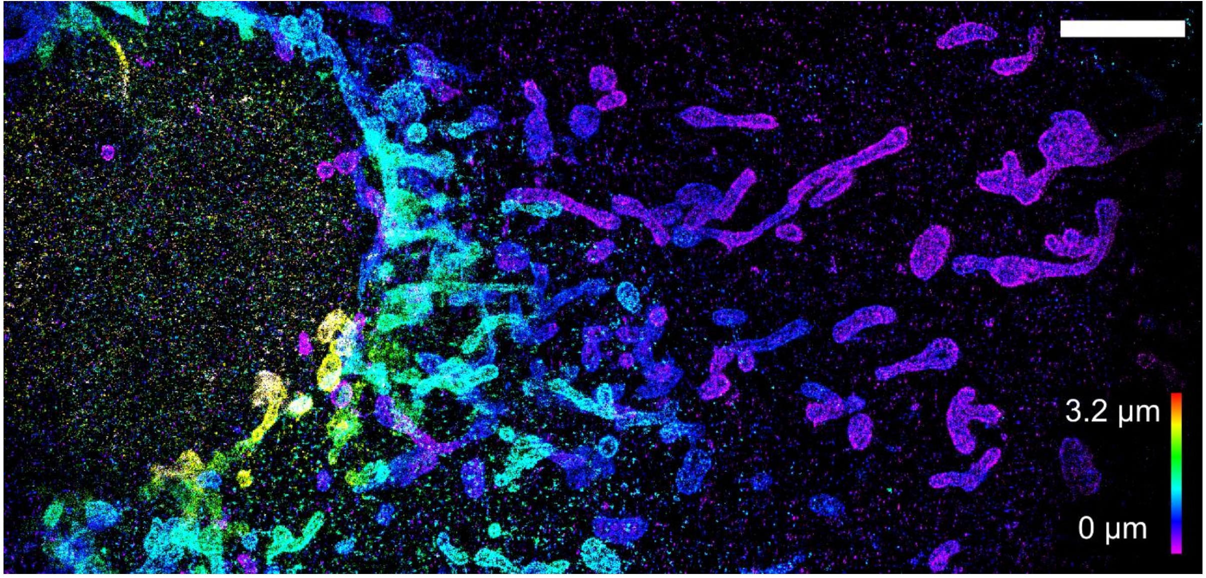

Figure 3.8 Mitochondrial network in a COS-7 cell at a depth of 3.2 microns, with 13 layers and 100K frames per layer using prSTORM. Imaging with conventional immunohistochemistry is limited to ~400K frames, but with prSTORM the fluorescence was refreshed permitting the structure to be densely sampled over an extended depth. Scale bar: 4 μm

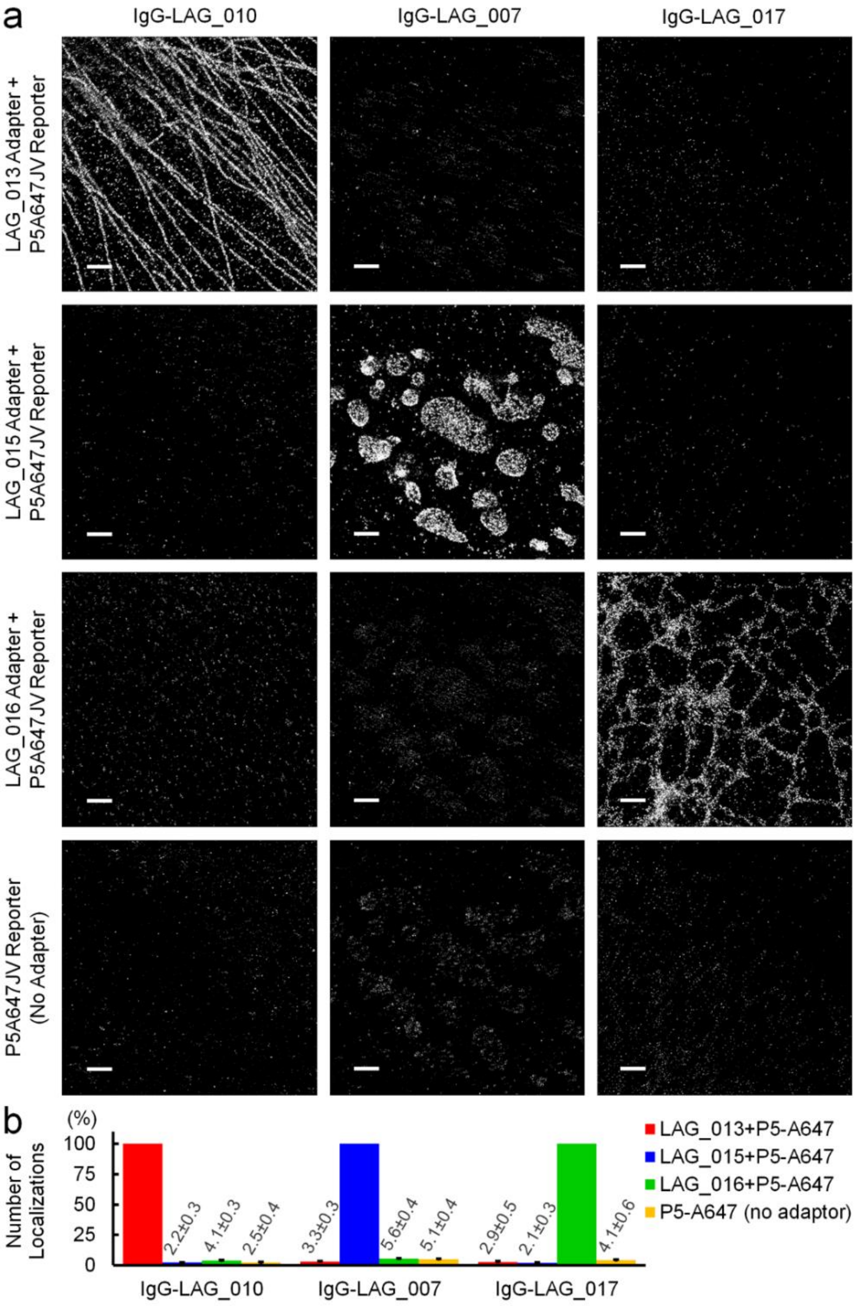

Figure 3.9 Cross-talk analysis for secondary antibodies for prSTORM used in this study. **a)** 2D STORM images, with the left, middle, and right columns showing cells immunostained for α-tubulin, TOM20, and sec61β-GFP, respectively. In successive rows, the specimen has been washed with hot water to remove adapter/reporter oligonucleotides, incubated with the indicated adapter/reporter oligonucleotides, washed, and imaged. Within each column, the same region of each cell is imaged. Scale bars: 1 µm. **b)** Quantitative analysis. The number of localizations was determined for each condition and normalized to the positive (bright) channel in each column. Because this approach counts localizations resulting from nonspecific binding, the crosstalk values

here likely represent an upper bound to the crosstalk. Data were expressed as mean ± standard error of the mean.

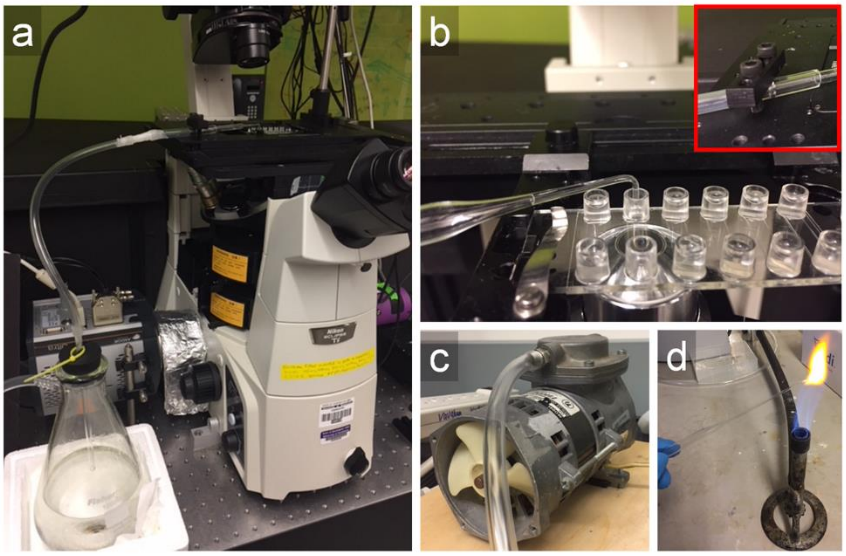

Figure 3.10 Simple stage-top flow channel apparatus for probe refresh STORM. **a)** An aspirator flask is connected to a vacuum pump and a Pasteur pipette that is secured above a flow channel containing fixed and immunostained cells. **b)** Close-up of Pasteur pipette with bent tip. The Pasteur pipette is positioned so that its tip is ~2-3 mm above the bottom of the flow channel without touching any part of the well. The inset shows how the Pasteur pipette is secured to the movable portion of the microscope stage so that it moves with the specimen. The unoccupied well across from the Pasteur pipette is used to deliver liquids into the channel by hand pipetting. When the vacuum pump **c)** is powered on, excess liquid from the flow channel is removed without sucking air bubbles through the channel. The vacuum pump is turned off during liquid incubations and data acquisition. **d)** Heating the tip of a Pasteur pipet over the flame of a Bunsen burner to bend its tip.

3.11 REFERENCES

1. Rust, M.J., M. Bates, and X. Zhuang. 2006. Sub-diffraction-limit imaging by stochastic optical reconstruction microscopy (STORM). Nat Methods. 3: 793–796.

2. Klar, T.A., S. Jakobs, M. Dyba, A. Egner, and S.W. Hell. 2000. Fluorescence microscopy with diffraction resolution barrier broken by stimulated emission. PNAS. 97: 8206–8210.

3. Betzig, E., G.H. Patterson, R. Sougrat, O.W. Lindwasser, S. Olenych, J.S. Bonifacino, M.W. Davidson, J. Lippincott-Schwartz, and H.F. Hess. 2006. Imaging intracellular fluorescent proteins at nanometer resolution. Science. 313: 1642–1645.

4. Gustafsson, M.G. 2000. Surpassing the lateral resolution limit by a factor of two using structured illumination microscopy. J. Microsc. 198: 82–87.

5. Huang, F., G. Sirinakis, E.S. Allgeyer, L.K. Schroeder, W.C. Duim, E.B. Kromann, T. Phan, F.E. Rivera-Molina, J.R. Myers, I. Irnov, M. Lessard, Y. Zhang, M.A. Handel, C. Jacobs-Wagner, C.P. Lusk, J.E. Rothman, D. Toomre, M.J. Booth, and J. Bewersdorf. 2016. Ultra-High Resolution 3D Imaging of Whole Cells. Cell. 166: 1028–1040.

6. Huang, B., W. Wang, M. Bates, and X. Zhuang. 2008. Three-dimensional super-resolution imaging by stochastic optical reconstruction microscopy. Science. 319: 810–813.

7. Juette, M.F., T.J. Gould, M.D. Lessard, M.J. Mlodzianoski, B.S. Nagpure, B.T. Bennett, S.T. Hess, and J. Bewersdorf. 2008. Three-dimensional sub–100 nm resolution fluorescence microscopy of thick samples. Nat. Methods. 5: 527–529.

8. Pavani, S.R.., M.A. Thompson, J.S. Biteen, S.J. Lord, N. Liu, R.J. Twieg, R. Piestun, and W.E. Moerner. 2009. Three-dimensional, single-molecule fluorescence imaging beyond the diffraction limit by using a double-helix point spread function. PNAS. 106: 2995.

9. Shtengel, G., J.A. Galbraith, C.G. Galbraith, J. Lippincott-Schwartz, J.M. Gillette, S. Manley, R. Sougrat, C.M. Waterman, P. Kanchanawong, M.W. Davidson, and others. 2009. Interferometric fluorescent super-resolution microscopy resolves 3D cellular ultrastructure. PNAS. 106: 3125.

10. Jia, S., J.C. Vaughan, and X. Zhuang. 2014. Isotropic three-dimensional super-resolution imaging with a self-bending point spread function. Nature Photonics. 8: 302–306.

11. Huang, B., S.A. Jones, B. Brandenburg, and X. Zhuang. 2008. Whole-cell 3D STORM reveals interactions between cellular structures with nanometer-scale resolution. Nat. Methods. 5: 1047–1052.

12. Tam, J., G.A. Cordier, J.S. Borbely, Á. Sandoval Álvarez, and M. Lakadamyali. 2014. Cross-Talk-Free Multi-Color STORM Imaging Using a Single Fluorophore. PLoS One. 9: e101772.

13. Valley, C.C., S. Liu, D.S. Lidke, and K.A. Lidke. 2015. Sequential Superresolution Imaging of Multiple Targets Using a Single Fluorophore. PLoS One. 10: e0123941.

14. Lin, J.-R., M. Fallahi-Sichani, and P.K. Sorger. 2015. Highly multiplexed imaging of single cells using a high-throughput cyclic immunofluorescence method. Nat. Commun. 6: 8390.

15. Jungmann, R., C. Steinhauer, M. Scheible, A. Kuzyk, P. Tinnefeld, and F.C. Simmel. 2010. Single-Molecule Kinetics and Super-Resolution Microscopy by Fluorescence Imaging of Transient Binding on DNA Origami. Nano Lett. 10: 4756–4761.

16. Jungmann, R., M.S. Avendaño, J.B. Woehrstein, M. Dai, W.M. Shih, and P. Yin. 2014. Multiplexed 3D cellular super-resolution imaging with DNA-PAINT and Exchange-PAINT. Nature Methods. 11: 313–318.

17. Legant, W.R., L. Shao, J.B. Grimm, T.A. Brown, D.E. Milkie, B.B. Avants, L.D. Lavis, and E. Betzig. 2016. High-density three-dimensional localization microscopy across large volumes. Nat. Methods. 13: 359–365.

18. Schueder, F., J. Lara-Gutiérrez, B.J. Beliveau, S.K. Saka, H.M. Sasaki, J.B. Woehrstein, M.T. Strauss, H. Grabmayr, P. Yin, and R. Jungmann. 2017. Multiplexed 3D super-resolution imaging of whole cells using spinning disk confocal microscopy and DNA-PAINT. Nat. Commun. 8: 2090.

19. Schueder, F., M.T. Strauss, D. Hoerl, J. Schnitzbauer, T. Schlichthaerle, S. Strauss, P. Yin, H. Harz, H. Leonhardt, and R. Jungmann. 2017. Universal Super-Resolution Multiplexing by DNA Exchange. Angew. Chem. Int. Ed. 56: 4052–4055.

20. Wang, Y., J.B. Woehrstein, N. Donoghue, M. Dai, M.S. Avendaño, R.C.J. Schackmann, J.J. Zoeller, S.S.H. Wang, P.W. Tillberg, D. Park, S.W. Lapan, E.S. Boyden, J.S. Brugge, P.S. Kaeser, G.M. Church, S.S. Agasti, R. Jungmann, and P. Yin. 2017. Rapid Sequential in Situ Multiplexing with DNA Exchange Imaging in Neuronal Cells and Tissues. Nano Lett. 17: 6131–6139.

21. Sano, T., C. Smith, and C. Cantor. 1992. Immuno-PCR: very sensitive antigen detection by means of specific antibody-DNA conjugates. Science. 258: 120–122.

22. Hendrickson, E.R., T.M.H. Truby, R.D. Joerger, W.R. Majarian, and R.C. Ebersole. 1995. High sensitivity multianalyte immunoassay using covalent DNA-labeled antibodies and polymerase chain reaction. Nucleic Acids Res. 23: 522–529.

23. Dezfouli, M., S. Vickovic, M.J. Iglesias, J.M. Schwenk, and A. Ahmadian. 2014. Parallel barcoding of antibodies for DNA-assisted proteomics. Proteomics. 14: 2432–2436.

24. Mikhaylova, M., B.M.C. Cloin, K. Finan, R. van den Berg, J. Teeuw, M.M. Kijanka, M. Sokolowski, E.A. Katrukha, M. Maidorn, F. Opazo, S. Moutel, M. Vantard, F. Perez, P.M.P. van Bergen en Henegouwen, C.C. Hoogenraad, H. Ewers, and L.C. Kapitein. 2015. Resolving bundled microtubules using anti-tubulin nanobodies. Nat. Commun. 6: 7933.

25. Chang, J.-B., F. Chen, Y.-G. Yoon, E.E. Jung, H. Babcock, J.S. Kang, S. Asano, H.-J. Suk, N. Pak, P.W. Tillberg, A.T. Wassie, D. Cai, and E.S. Boyden. 2017. Iterative expansion microscopy. Nat. Methods. 14: 593–599.

26. Shi, X., J. Lim, and T. Ha. 2010. Acidification of the Oxygen Scavenging System in Single-Molecule Fluorescence Studies: In Situ Sensing with a Ratiometric Dual-Emission Probe. Anal Chem. 82: 6132–6138.

27. Nixon-Abell, J., C.J. Obara, A.V. Weigel, D. Li, W.R. Legant, C.S. Xu, H.A. Pasolli, K. Harvey, H.F. Hess, E. Betzig, C. Blackstone, and J. Lippincott-Schwartz. 2016. Increased spatiotemporal resolution reveals highly dynamic dense tubular matrices in the peripheral ER. Science. 354: aaf3928.

28. Dempsey, G.T., J.C. Vaughan, K.H. Chen, M. Bates, and X. Zhuang. 2011. Evaluation of fluorophores for optimal performance in localization-based super-resolution imaging. Nat. Methods. 8: 1027–1036.

29. von Diezmann, A., Y. Shechtman, and W.E. Moerner. 2017. Three-Dimensional Localization of Single Molecules for Super-Resolution Imaging and Single-Particle Tracking. Chem. Rev. 117: 7244–7275.

30. Auer, A., M.T. Strauss, T. Schlichthaerle, and R. Jungmann. 2017. Fast, Background-Free DNA-PAINT Imaging Using FRET-Based Probes. Nano Letters. 17: 6428–6434.

31. Iinuma, R., Y. Ke, R. Jungmann, T. Schlichthaerle, J.B. Woehrstein, and P. Yin. 2014. Polyhedra self-assembled from DNA tripods and characterized with 3D DNA-PAINT. Science. 344: 65–69.

32. Beater, S., P. Holzmeister, B. Lalkens, and P. Tinnefeld. 2015. Simple and aberration-free 4color-STED - multiplexing by transient binding. Opt. Express. 23: 8630.

33. Expansion Microscopy. 2017. 22 Nov 2017. http://expansionmicroscopy.org/.

34. Agasti, S.S., Y. Wang, F. Schueder, A. Sukumar, R. Jungmann, and P. Yin. 2017. DNA-barcoded labeling probes for highly multiplexed Exchange-PAINT imaging. Chem. Sci. 8: 3080–3091.

35. Chen, F., P.W. Tillberg, and E.S. Boyden. 2015. Expansion microscopy. Science. 347: 543–548.

Chapter 4. HARDWARE FOR MICROSCOPY

4.1 PREFACE

Fluorescence microscopy is enabled, in part, by having a well-tuned optical system which can reproduce the image of a specimen with high fidelity. Consequently, technological developments in microscopy are intimately tied to developments in optics, light sources and detectors. High numerical aperture lenses which are aberration-corrected, enable high resolution images to be created by collecting a large cone of light. These lenses have been crucial for observing and studying the dim fluorescence of single fluorescent molecules. Laser technology has provided microscopy with highly coherent light sources which are ideal for exciting fluorescent probes with high power and narrow bandwidth. Lasers beams are also easily shaped, and interesting illumination schemes have been used to simply reject background light (1) or break the diffraction-limit(2). Finally, ultra-sensitive and fast (~1000 Hz) CCDs enabled cellular dynamics to be imaged with high spatial and temporal resolution, even though genetically-encoded probes are dim.

It is now possible to purchase these components off-the-shelf in order to create custom microscopy solutions to push the technological envelope or image new kinds of samples. For example, Eric Betzig and colleagues created the lattice light sheet microscope which has enabled fast-cellular dynamics to be captured while delivering an order of magnitude lower light dose (3). In another example, McGorty et al. have created an innovative single plane illumination microscope setup which is compatible with samples that would normally be used in conventional, Epi-fluorescence (EPI) (4).

In this chapter I will describe how I designed and characterized three different custom microscopy setups. Each of these setups relies on two different illumination and detection schemes: total internal reflection (TIR) and confocal. In **Section 4.1.1 and Section 4.2.1** I will develop the principles of total internal reflection fluorescence microscopy (TIRFM) and confocal microscopy respectively.

In **Section 4.1.2** I will describe a total internal reflection fluorescence microscope (TIRFM) which I helped design and build for the group of our collaborator, Prof. Daniel Chiu. I built the microscope to study single semiconducting polymer dots at the coverslip. Consequently, I selected to use a total internal reflection (TIR) geometry, in order to maximize signal to background levels. I characterized the microscope by measuring the power density at the sample plane and obtained images that demonstrate TIR illumination. In **Section 4.1.3** I describe an existing TIRFM setup I modified to include a 3-electode potentiostat, in which the voltage potentials are synchronized with the camera readouts. Once again, I selected the TIR geometry because I wanted to study single molecule events at the surface of an optically clear electrode. In **Section 4.2.2** I describe how I characterized the point spread function of a home-built spinning-disc confocal microscope. The home-built design is substantially less expensive, and much more customizable than commercial versions, so I measured the effect of pinhole size on the microscope's Point Spread Function (PSF).

4.2 TOTAL INTERNAL REFLECTION MICROSCOPY (TIRFM)

4.2.1 *Principles of TIRFM*

Total internal reflection (TIR) occurs when light within a medium of higher index of refraction is incident at a sufficiently large angle upon an interface with a medium of lower index of refraction as predicted by Snell's law, $n_1 \sin\Theta_1 = n_2 \sin\Theta_2$. At angles larger than the critical angle, the incident light beam completely reflects at the interface, and it creates an evanescent wave which propagates parallel to the surface, and decays exponentially perpendicular to the surface.

The evanescent wave generated by TIR can be used for microscopy to excite fluorophores near interface while only exciting very few molecules in the bulk solution because it decays within ~100-200 nm of the surface. This illumination geometry is advantageous for specimens located near the surface because it avoids intense background fluorescence in thick samples, and because it enables detailed analysis of the specimen at the interface. In its first implementation, Ambrose et al. used a mercury arc lamp for illumination, and a prism to achieve TIR, and they studied light scattered off the specimen to study movements of filamentous mould (1). Later the technique was extended to incorporate lasers, fluorescent dyes, and illumination with high-numerical aperture (NA) objective lenses rather than a prism in order to achieve TIR (5). For instance, Axelrod et al. demonstrated they could effectively study fluorescently labeled red blood cells with extremely low background – showing the efficacy of prisimless TIRF combined with laser illumination(5).

Objective-Based TIR Principles:

If we consider light rays incident upon the specimen, one can rearrange Snell's law to find the critical angle, θ_c, necessary for TIR.

$$\theta_c = \sin^{-1}\left(\frac{n_1}{n_2}\right) \qquad \text{Eq. 4.1}$$

Here, n_1 and n_2 represent the indices of refraction of the materials at the interface. In a typical TIRFM experiment the specimen is in an aqueous environment ($n_1 = n_w = 1.33$) and it is placed on a glass slide ($n_2 = n_g = 1.52$). This implies that the critical angle necessary to achieve TIR, θ_c , is 61.4°. If we want to use the objective lens to achieve TIR, this means that the objective needs to have a high enough NA in order to bend the light to the critical angle. The NA of the lens is defined as

$$NA = n_i \sin\theta_o \qquad \text{Eq. 4.2}$$

where NA is the numerical aperture of the lens, n_i ,is the index of refraction and θ_o is the maximum angle of light that the objective can detect. For example, if a 1.45 NA lens is used, the maximum angle that can be made with the interface is 72° which is sufficient to achieve TIR. In general, any objective can be used to achieve TIR as long as this condition holds, although in practice only oil-immersion lenses of NA ≥ 1.4 are regularly used for TIR:

$$NA > n_w \qquad \text{Eq. 4.3}$$

In TIR geometry the penetration depth of the evanescent wave is given by

$$I_z = I_o\, Exp[-z/d] \qquad \text{Eq. 4.4}$$

where I_o is the intensity of the incident wave, z is the depth into the sample, and the penetration depth term d depends on the wavelength, illumination angle with respect to surface normal, and the indices of refraction:

$$d = \frac{\lambda}{4\pi}\left(n_2^2 \sin^2\theta - n_1^2\right)^{-1/2} \qquad \text{Eq. 4.5}$$

where λ is the wavelength of the light, n_1 and n_2 are the indices of refraction, and θ is angle of the beam. For example if we use 650 nm light, a 1.45 objective, and a 72° angle, the penetration depth is 91 nm. Taken together, equation 4 and equation 5 indicate that only objects near the interface will be detected (5, 6) **(Figure 4.1)**. The angle the light makes as it exits the objective lens is dependent upon the radial position of beam at the back focal plane of the objective.

Therefore it is easy to switch between epi illumination and TIR illumination by translating the excitation beam from the center to the edge of the objective's back focal plane.

4.2.2 *Construction of a TIRF Microscope*

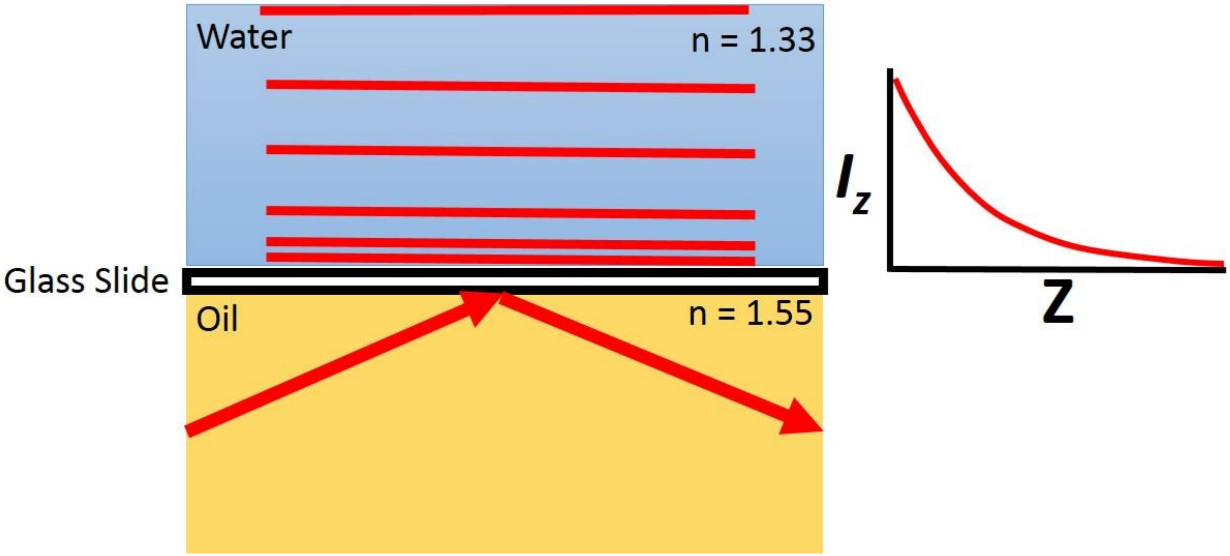

Figure 4.1 An example of total internal reflection using a high NA oil-immersion lens. The excitation light is incident on a glass slide at or above the critical angle. This results in an evanescent wave whose intensity decays exponentially perpendicular to the surface. The plot on the right gives an example decay curve for the evanescent wave, where the intensity at axial position *Z* (I_z) falls of exponentially as Z increases.

While I was working on my PhD I had the opportunity to build a TIRF microscope for the research group of Dr. Daniel Chiu which is now being used to study semiconducting polymer dots at the single particle level. The microscope was designed around a commercial Nikon microscope chassis with two independent homebuilt modules, the beam combination module and the TIRF module. The beam combination module is used to collimate each beam, make them the same size, and ensure they are all co-linear. Two lenses (L1 and L2 in **Figure 4.2**) are placed in front of the 405 nm laser to expand the beam to match the size of the 640 nm and 488 nm beams.

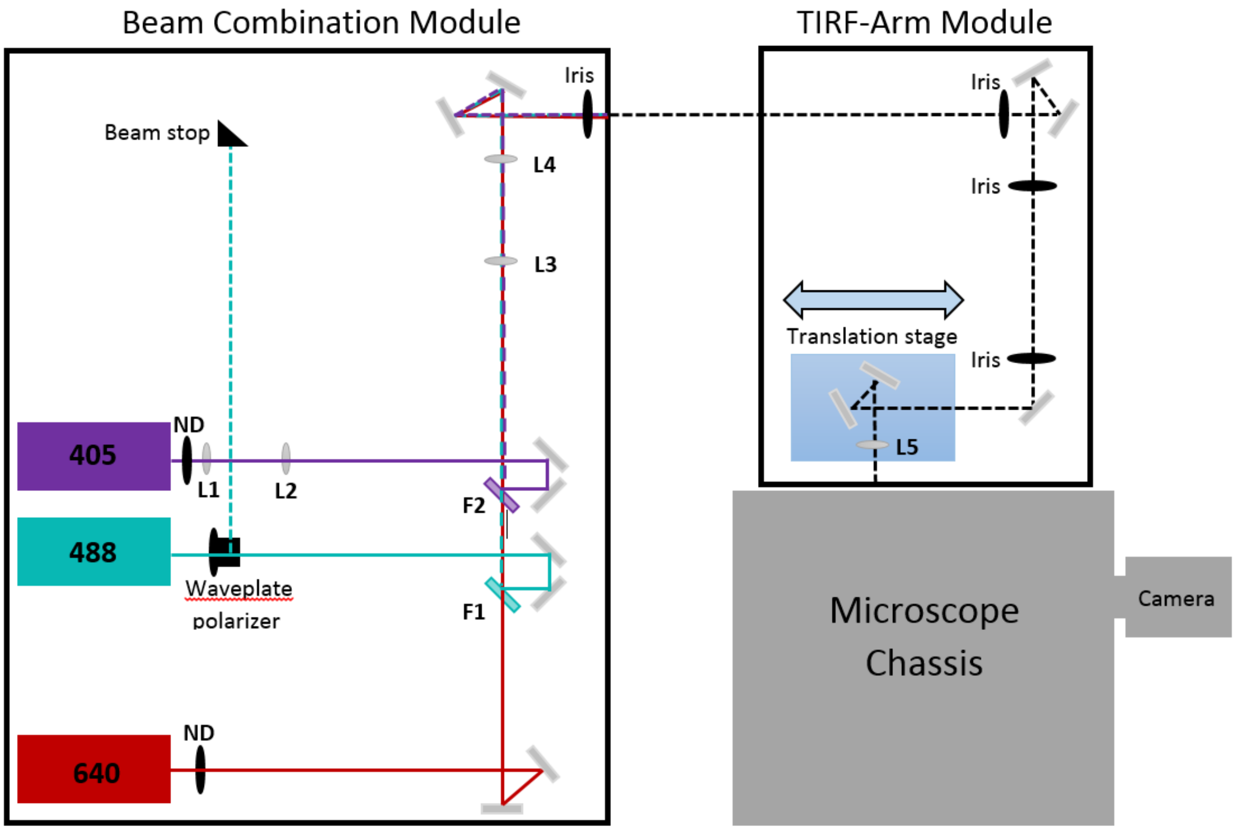

Figure 4.2 Diagram of a TIRF microscope. The microscope contains two modules, a beam combination module and a TIRF-arm module. The beam combination module collimates a 640 nm, 488 nm, and 405 nm laser and ensures they are all co-linear and the same size. A waveplate polarizer was placed in front of the 488 nm laser in order to control its intensity. Each laser line uses two mirrors which can be used to align all the beams independently. Once the beams are all combined, a final set of mirrors are used to direct the beams into the TIRF module. Inside the TIRF module, two mirrors and a lens are used to focus the beam onto the edge of the objective's back focal plane – achieving TIR. The neutral density filter (ND) and waveplate polarizer are placed in front of the lasers to attenuate their power, and the filters F1 and F2 are used to allow beams earlier in the illumination path to pass, while reflecting the next beam into the illumination path. The irises are placed to allow facile alignment between modules and into the microscope.

Microscope Characterization:

The first step in characterizing the TIRF microscope is measuring the power density. This is achieved by placing a fluorescent specimen on the stage, and illuminating a known area in epi-fluorescence. Typically a specimen is imaged on the camera, and the area is measured from that image. Then a power meter is used to measure the power of the beam out of the objective. The power density is calculated by dividing the power measured by the area illuminated. (**Figure 4.3**) After the power density was measured, images of cells at each of the wavelengths both in epi and TIR illumination were taken. To test the 405 nm and 488 nm channels, the nuclei of cells were stained with the fluorescent DNA-binding dyes Hoechest and Propidium Iodide and imaged in EPI and TIR geometries. Both images exhibited greatly reduced background and depth of focus in TIR compared to EPI. To test the 640 nm channel, cellular microtubules were immunostained with Alexa 647. In this case, the background reduction is not as evident because microtubules are optically thin compared to the nucleus (**Figure 4.4**). However one can observe the approximately 3-4× power enhancement which is a characteristic of the TIR geometry (**Figure 4.4**). Finally, the ability of the microscope to induce single molecule photoswitching was tested, and we found that the central part of the illumination had intensities sufficient to cause molecules to switch between a fluorescent and non-fluorescent state (~3 kW/cm^2).

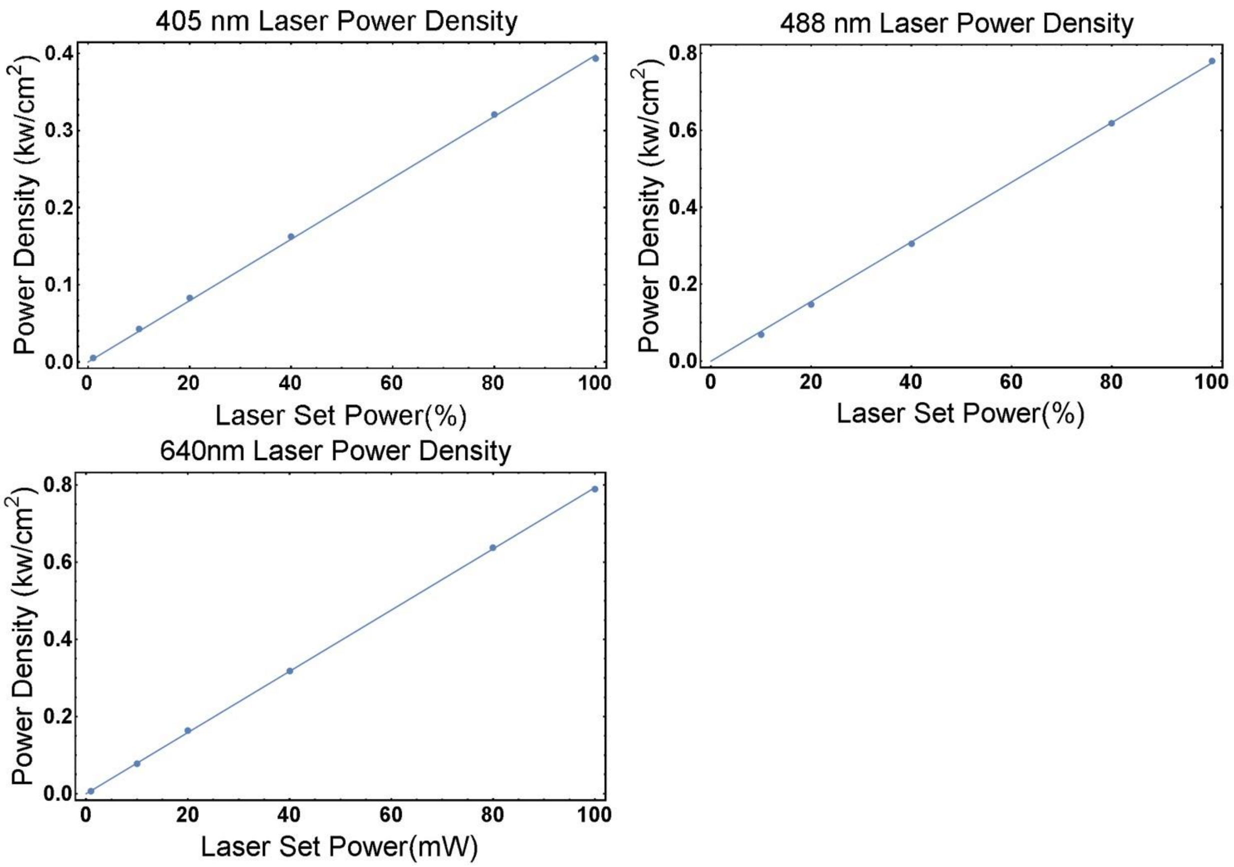

Figure 4.3 Measurement of the power density as a function of the laser set power for the 405, 488 and 640 nm lasers.

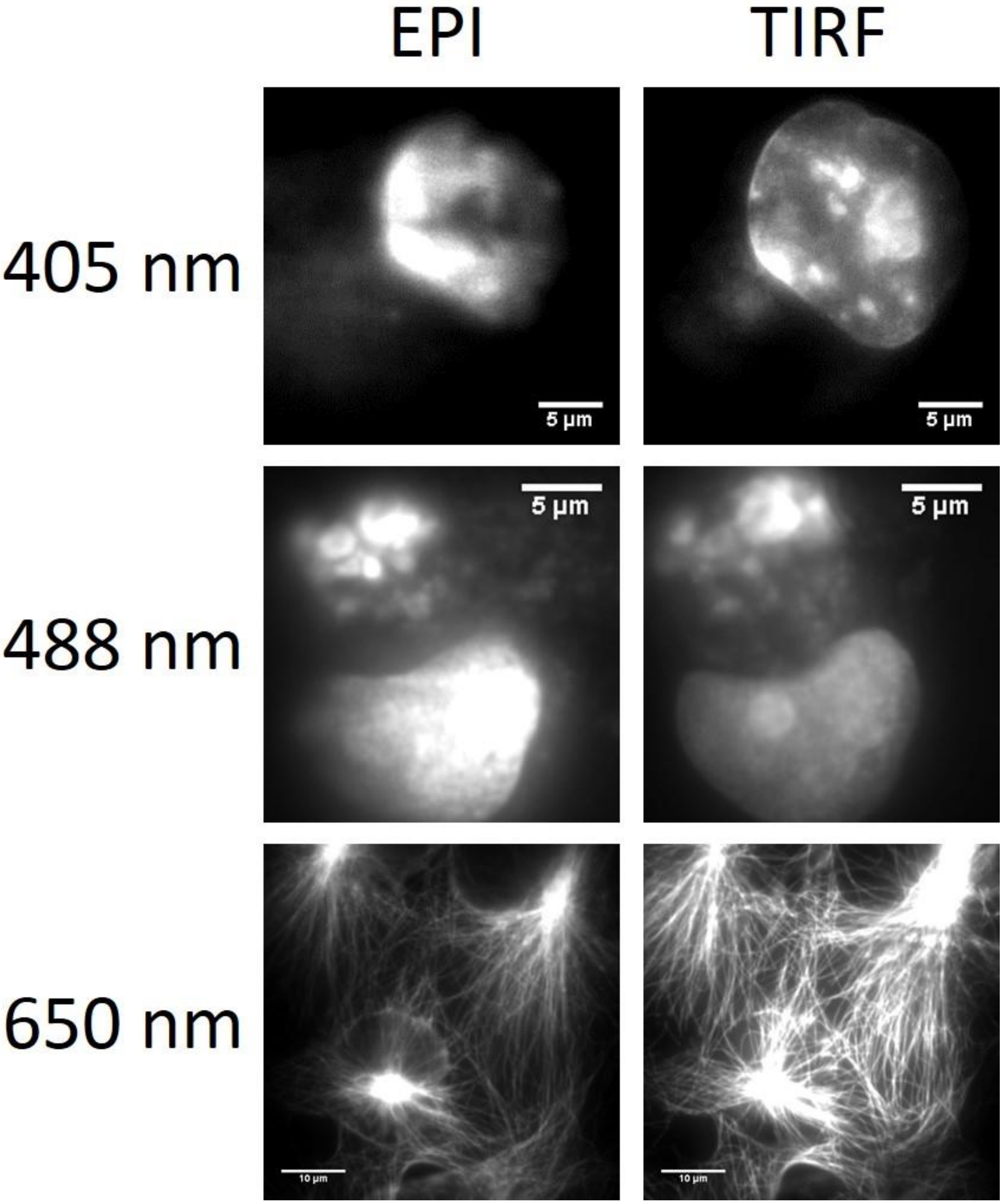

Figure 4.4 Epi and TIR Images obtained using the 405, 488, and 647 nm lasers. The 405 and 488 nm lasers were used to image cell nuclei that were stained Hoechst and Propidium Iodide. Observe that the TIR images exhibit lower background than their EPI counterparts. The 640 nm laser was used to image microtubules stained with Alexa 647. Notice that the TIR image is brighter due to the 3x TIR power enhancement

4.2.3 *Use of TIR for Observing Single-Molecule Redox Events*

There is great interest in understating the early stages of electrochemical reactions in order to optimize the electrodes and catalysts of the future. Single-molecule fluorescence microscopy is well suited for this, because it can detect single redox events with high spatial and temporal resolution—permitting researchers to gain detailed understanding of the electrochemical interface. These experiments can be conducted at hundreds of Hz, and automated synchronization between the optical and electrochemical components is critical. Here I present a useful scheme I used to synchronize data acquisition on an optically clear indium tin oxide (ITO) electrode.

In two independent experiments I had the opportunity to work with Dr. Bo Zhang's lab in order to study redox events at the single molecule level by utilizing TIRFM. I contributed by imaging their samples on an existing home-built TIRF microscope. In these experiments, the ITO serves as the working electrode of a 3 electrode potetiostat. The potential of the working electrode changes in time, and redox events at the surface are read out optically. We selected fluorescent resorufin, which can reversibly cycle between non-fluorescent dihydroresorufin upon 2 electron oxidation or reduction, in order to optically detect each redox event.

Utilizing fluorescence to interrogate redox events is particularly notable because it gives the ultimate single redox event sensitivity. When utilizing resorufin, this means that every turn–on event represents exactly 2 electrons being transferred to one molecule while emitting hundreds or thousands of photons. This is remarkable, because it allows practitioners to observe distinct electrochemical events well before a current would be measurable in a traditional cyclic voltammetry experiment. We conducted two different kinds of experiments with this setup which resulted in publications the Proceedings of the National Academy of Sciences (PNAS) and the

Journal of the American Chemical Society (JACS): The first was studying the diffusion of resorufin inside of nano-porous silica channels deposited on the ITO surface. And The second was to observe the early stages of hydrogen nucleation on an electrode (7, 8).

Experiment Automation and Setup

In this experimental setup, redox events are detected by recording fluorescence on a camera, and the sample illuminated by a laser as the potential of the ITO electrode changes in time. Therefore, it was important to synchronize the illumination, the camera, and the electrode potential. I achieved this by timing everything off a transistor-transistor logic (TTL) pulse (camera fire signal) the camera output every time it took a frame.

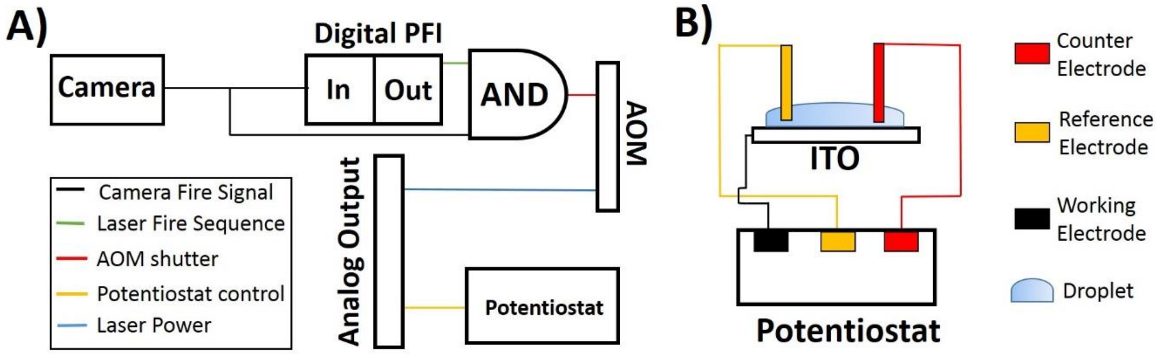

Figure 4.5 (A) Wiring diagram for synchronizing the camera, lasers, and applied potential. The camera sends out a TTL pulse (camera fire) into an NI-DAQ digital input. The digital output holds a buffered laser fire sequence, which outputs one element per TTL pulse. Both the camera and the laser fire sequence are wired to the AND gate in order to shutter the AOM. This is done in order to not illuminate the specimen during the CCD transfer time. The laser power and potentiostat control voltages are also timed to the camera via a connection internal to the DAQ.
(B) The potentiostat is connected externally to the imaging setup. Which includes an optically clear working (ITO), reference (Ag/AgCl), and counter electrode (Pt). The droplet contains dilute (nm) concentrations of resorufin which undergoes a redox reaction as the potential of the ITO changes in time

The TTL pulse is connected to a National Instruments Data Acquisition (NI-DAQ) card, and it serves as the clock for the experiment. (**Figure 4.5**) Before starting the experiment, a laser fire sequence, laser power control sequence, and potentiostat control sequence are all buffered in the NI-DAQ. When the experiment begins, the information flows out of the buffers all timed on the camera TTL pulse. Each time the pulse is high, one element from each sequence is sent out of the digital and analog outs. The AND gate goes high, when both the laser fire sequence and camera fire sequence are high. The signal from the AND gate connects to the AOM, and is used as a shutter for the laser. When the AOM receives a signal, it diffracts light into the illumination path proportional the analog signal it received. Otherwise no light passes through the illumination path of the microscope. Consequently this causes the specimen to be illuminated when the camera shutter is open, and dark during the CCD transfer time. The DAQ has two analog outputs which are timed to the camera fire signal: One sends a voltage to control the laser power, and the other sends a voltage to control the potentiostat. These two connections ensure the laser power and potential are set deterministically during the experiment.

4.3 CONFOCAL MICROSCOPY

4.3.1 *Introduction to Confocal Microscopy*

Confocal Microscopy is another technique used to minimize background fluorescence from out of focus emitters (9, 10). In confocal microscopy, light is focused to a small volume within the sample. In contrast, objective TIRF utilizes a highly angled and collimated beam that typically reflects off the glass-water interface. In this geometry, the whole specimen is bathed in light rather than a thin region at the coverslip—causing out of focus fluorophores to emit light. The out of focus light increases the background fluorescence and degrades image quality. This can be remedied by placing a pinhole at the detector’s image plane, which is conjugate to the sample plane, and raster scanning the laser beam over the specimen. In principle, the pinhole causes rays of light originating from the defocused volume to be blocked—only permitting light from the focal plane to be recorded on the detector (**Figure 4.6)** (11). This innovation has revolutionized microscopy and life-sciences because it enabled the facile collection of high-fidelity 3D images with resolution a >250 nm. Confocal microscopy is usually performed in one of two principal modalities: confocal laser scanning microscopy (CLSM) and spinning disc confocal microscopy (SDCM) (12, 13). In CLSM a single pinhole is used, and motorized mirrors are used to raster scan a laser beam across the specimen—illuminating the specimen point-by-point (12). The fluorescence emitted from each point on the specimen is recorded on a photomultiplier tube and an image is created once per scan. In SDCM, the pinhole is replaced by an array of pinholes on a spinning disc that are illuminated by a laser. This causes the specimen to be illuminated by an array of beamlets in parallel, allowing the entire specimen to be illuminated much more quickly than in CLSM (9, 13, 14). The light coming from the sample passes back through the array of pinholes and is recorded on a CCD (9), and the out of focus light is blocked—just like in CLSM.

Each type of confocal microscopy has its own set of tradeoffs. In CLSM the resolution is slightly better, the rejection of out of focus light is better (for thick samples), and the power density achievable is substantially higher than in SDCM. However, in CLSM the frame rates tend to be slow because the beam has to be raster scanned across the sample, and the fluorescence is recorded in serial—point-by-point (12). On the other hand, SDCM can achieve frame rates on the order of hundreds frames per second (fps), because the beamlets are scanned and the image is recorded all in parallel across the sample (13).

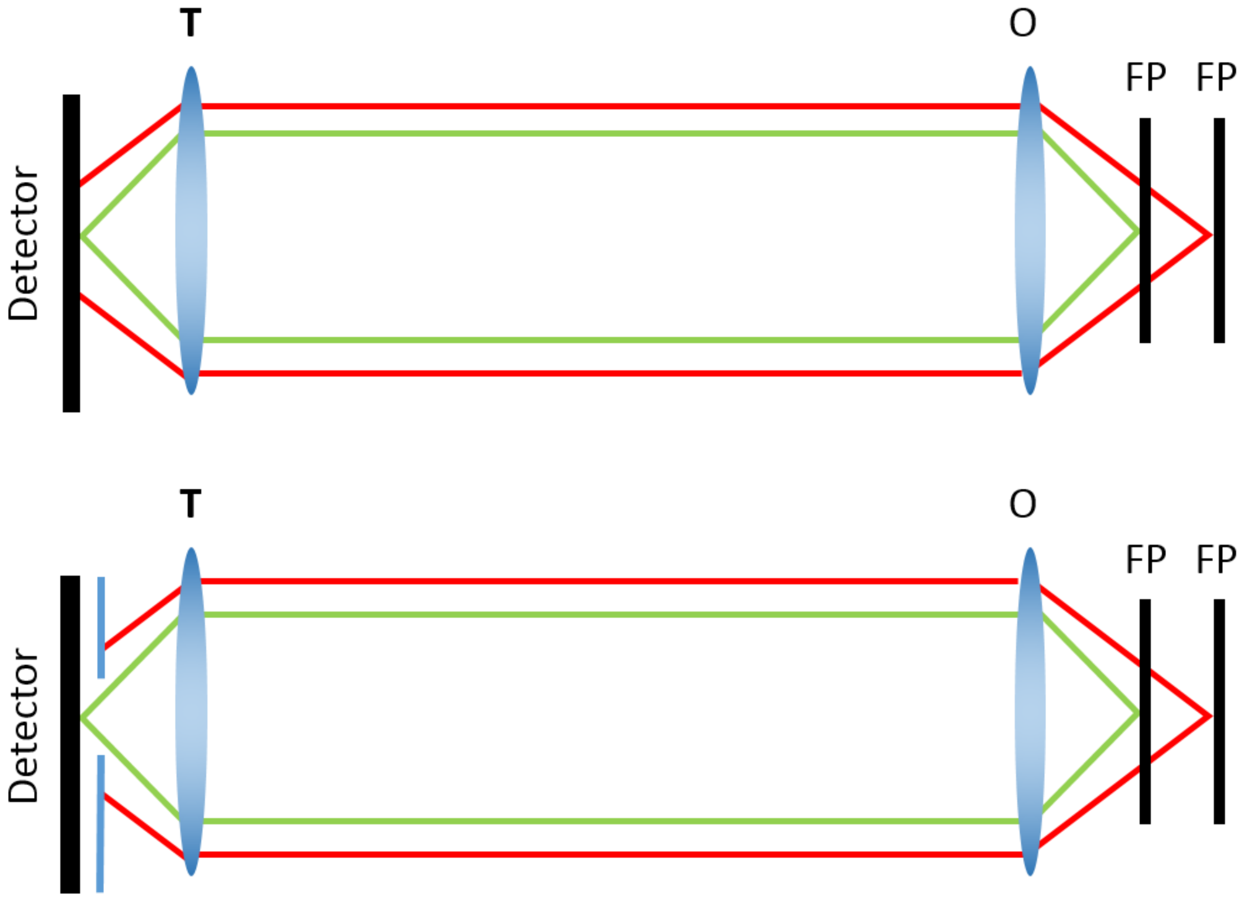

Figure 4.6 (top)Figure showing a typical epi-fluorescence emission path. Rays radiate from a focal plane (FP), where they pass through an objective lens (O) and are focused onto a detector by a tube lens (T). Observe how the light originating from the focal plane conjugate with the detector (green) are brought into focus, but how light originating from other focal planes (red) reach the detector.(bottom): In order to block out of focus light, a pinhole is placed in front of the detector. This prevents out of focus light from reaching the detector, which increases the contrast by reducing background fluorescence.

This feature is particularly attractive for studying live specimens because the fast frame rates allow rapid cellular dynamics to be captured, and the lower power densities reduce photoxicity. Despite being slower and more phototoxic, CLSM is still commonly used because it typically features a single adjustable pinhole which renders it compatible larger set of objectives, wavelengths, and specimens than SDCM (15, 16). A CLSM setup can image specimens of an arbitrary thickness, because there is only one pinhole, and there is no need to worry about neighboring pinholes interacting which occurs in SCDM (9). In contrast, SDCM discs tend to have a fixed pinhole size and spacing which limits their use to a narrow range of objectives, sample thicknesses. CLSMs also have much higher transmission efficiencies of the excitation light compared to SDCMs because the pinhole is placed at the detection plane and the illumination does not pass through the pinhole. On the other hand, SDCMs tend to have low transmission efficiencies because the excitation light passes through an array of pinholes which reduces the transmission to ~1-4%. One can overcome this by using a more powerful laser to achieve the desired power densities the sample, or one can improve the transmission efficiency by utilizing a two disc system pioneered by the Yokogawa Corporation (17). In the two-disc system, the transmission efficiency is improved by using a first disc containing a micro lens array that focuses the illumination light through the pinhole array of the second disc, for an excitation transmission efficiency of >50%. One drawback of this two disc system is that the dichroic beamsplitter must be inserted in the narrow space between the microlens array disc and the pinhole array disc. The details concerning transmission efficiency, pinhole spacing, and pinhole size as they relate to SDCM are covered in more detail below. Although slits can be used rather than pinholes with a gain in transmission efficiency while sacrificing z-resolution, the discussion here will be limited to pinholes (18). This is because the disc we designed utilizes pinholes rather than slits due to improved axial sectioning capability compared to slits (19).

4.3.2 *Principles of SDCM*

As alluded to in the previous section, transmission efficiency, pinhole spacing, and pinhole size are all intertwined—determining the types of samples that can be imaged and the overall performance of the disc.

Fill Factor and Transmission Efficiency

Among the most important parameters concerning SDCM is the transmission efficiency of incident laser light on the disc. The transmission efficiency along with the laser determines how intensely the specimen can be illuminated, and a well-illuminated specimen that is also labeled well will emit bright fluorescence which can be captured on a detector with short integration times. If the transmission efficiency is low, then it is necessary to acquire images at low frame rates, on par with CLSM. Therefore, in some sense, it is the goal of SDCM to maximize transmission efficiency while continuing to block fluorescence originating outside the focal plane. The transmission efficiency is given by the ratio of the diameter of the individual pinholes (*D)*, to the spacing between the pinholes (*S*).

$$T = \left(\frac{D}{S}\right) \qquad \text{Eq. 4.6}$$

By inspection one can see that at the limit of a large pinhole or very narrow spacing, the transmission efficiency can be increased. However as the pinhole grows or the spacing shrinks, the benefits of background rejection and improved resolution are lost as discussed below (18).

Selection of an optimal pinhole size:

The wavelength of light, the NA of the objective lens, and the size of the pinhole determines the PSF size, and therefore the maximum resolution of the optical system. Ideally the pinhole size is chosen to match the size of the PSF given a particular wavelength and NA. In fact, most CLSM feature adjustable pinhole sizes which is one reason they exhibit slightly improved resolution compared to SDCMs. However in SDCM's the pinhole has a fixed size, which typically is 40 or 50 μm. This pinhole sizing is well-matched with typical 60x and 100x high NA immersion objective lenses and wavelengths spanning the visible spectrum (405 nm – 650 nm), while affording an acceptable compromise in background rejection and resolution. The optimal pinhole size D_{opt} for a SDCM that achieves this goal is given by (18)

$$D_{opt} = \frac{0.5\, M\, \lambda}{NA} \qquad \text{Eq. 4.7}$$

where M is the magnification of the objective lens, λ is the wavelength, and NA is the numerical aperture of the objective lens. When D is optimal, the resolution is maximized because the objective's back focal plane gets filled by light diffracting through the pinhole. If the pinhole is very large, then the diffraction pattern will not exhibit the desired high frequency components at the back focal plane—resulting in a larger spot at the sample plane. On the other hand, if the pinhole is very small, then the transmission efficiency decreases rapidly, with minimal gain in resolution. On the illumination side, an overly small pinhole is not desirable because it allows less light the reach the specimen resulting in less fluorescence. And on the detection side, a small pinhole rejects more of the signal than necessary—degrading the signal to noise ratio at the detector. Therefore the pinhole size needs to be carefully considered depending on the needs of the end user (18).

The best-case possible axial resolution for a given pinhole size is given by (18):

$$d = K \frac{\lambda}{\left[1 - \sqrt{1 - \left(\frac{NA}{n}\right)^2}\right]} \qquad \text{Eq. 4.8}$$

where λ is the wavelength n is the index of refraction, NA is the numerical aperture of the lens, and K is a scalar correction factor (for a pinhole $K = 0.67$). Importantly, this equation is a limiting case because it does not include the fact that out of focus light may pass through neighboring pinholes when the sample is thick and the background is high. This best-case can be observed by scanning the focal plane and obtaining image stacks of fluorescent beads, and measuring the axial PSF size. However, in practice thick samples can lead to pinhole crosstalk and cause artifacts in the image. Therefore it is important to select a pinhole spacing that is well matched to a typical specimen's thickness, so that the specimen is as clearly resolved as possible(18).

4.3.3 *Home-Built SDCM Characterization*

My final project in the lab was to characterize a homebuilt confocal microscope, with a custom spinning disc design. The microscope is divided into two modules. The beam combination module and the confocal module. In the beam combination module, two lenses are placed in front of each laser line (647 nm, 561 nm, 488 nm, 405 nm, and 750 nm) in order to collimate and make all the beams the same size. Each laser line bounces off of two mirrors, which are used to align each beam independently, so that they are all co-linear as they enter the acousto-optic modulator (AOM). A dichroic mirror is placed where each beam combines, and it is selected to transmit the combined beam, and to reflect the next laser line into the illumination path—combining each of the beams. The 405 nm and 750 nm lasers do not pass through the AOM because the model used in this setup only works for 488 nm – 647 nm light The light leaving the beam combination module is all co-linear, equally sized, and collimated. The combined beams then enter the confocal module, where a pair of lenses are used to expand beam to fill the objective's back focal plane. A dichroic mirror is inserted in between these two lenses in order to allow the emitted light to reach the camera, while reflecting the excitation light. After the beam is expanded, it is incident upon the disc which is placed conjugate to the focal plane. When the light strikes the disc, it diffracts and enters the side port of the microscope where the tube and objective lens focus the light on the specimen.

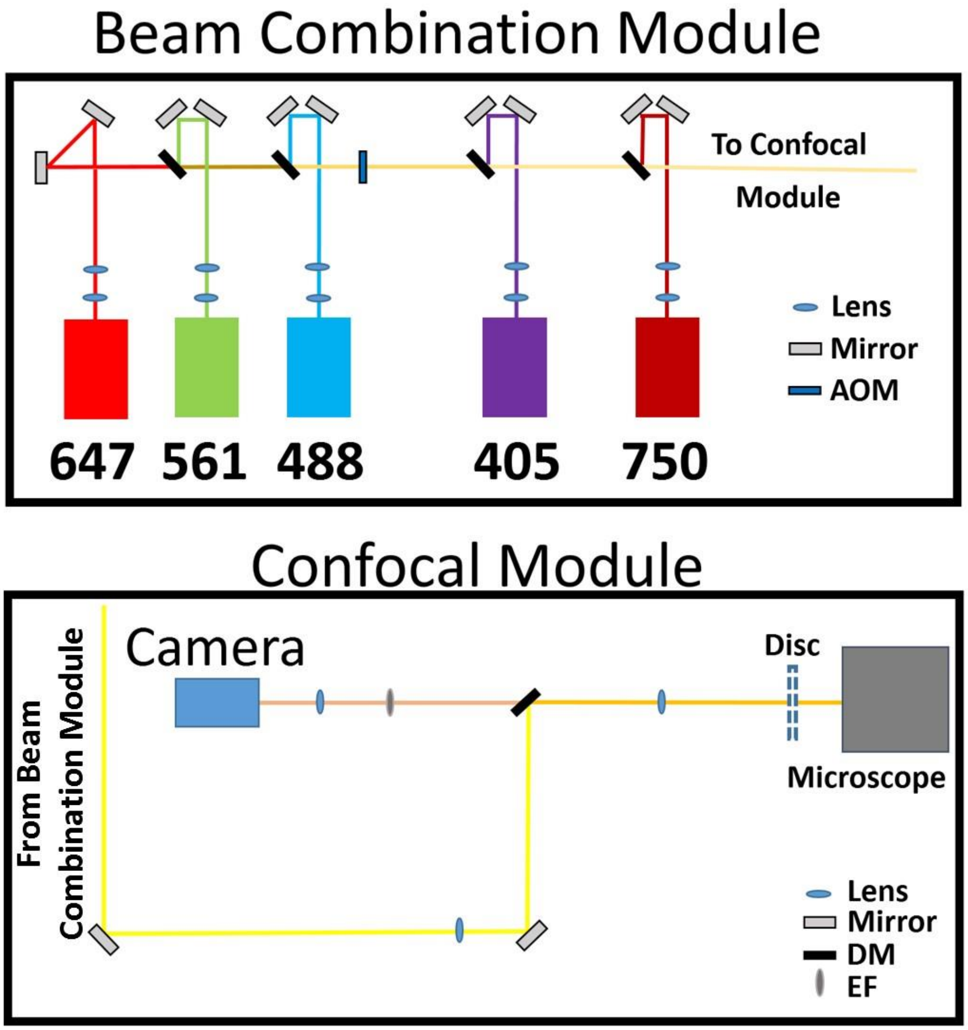

Figure 4.7 The microscope design is composed of two modules. The beam combination module (top) and the confocal module (bottom). The beam combination module utilizes pairs of lenses to collimate and shape each of the laser beams and an AOM to control how much power goes into the confocal module. A series of dichroic mirrors (DMs) are used to combine each wavelength of light be allowing more red light to pass, while reflecting a shorter wavelength beam to be co-linear with the red light passing through the filter. The 750 nm laser is an exception to this, and it is setup in a reverse pass configuration since it is a longer wavelength than 405 nm. In the confocal module, the collimated beam is expanded by a pair of lenses where it is incident upon confocal spinning disc. The light then enters the side port of the microscope where it is focused on the specimen. The image is then relayed through an emission filter to remove any of the excitation light and focused onto a camera.

4.3.4 *Disc Design*

Most commercial confocal spinning disc units cost between $50 and $100 thousand dollars. In part because of mechanical complexity required to have a pair perfectly synchronized spinning discs. The first disc has a microlens array, which focuses light down onto a second confocal disc in order to improve transmission efficiency. Our design utilizes a single glass disc which can be easily printed from a computer assisted design file, and mounted on a hard drive enclosure motor to make it spin. The hard drive enclosure is has a small window machined into the corner for the laser to illuminate the disc. Since our microscope is already equipped with powerful lasers (200-2000 mW across five laser lines, 405nm, 488nm, 561nm, 647nm, 750nm), we can combat the poor transmission efficiency of a single disc, by just using a powerful laser beam.

We wanted to investigate the effect of pinhole size and wavelength, so the disc I characterized was printed with a few different sectors, each containing different sized pinholes spaced at the 5 times pinhole's diameter. The pinholes are arranged on the disc in a spiral of constant pitch (Archimedean Spiral) in order to reduce striping artifacts that can occur if the disc is not perfectly centered on its axis of rotation.

4.3.5 *Measurement of Confocal PSF Size*

The confocal PSF is the principle determinant of image quality. Therefore it is important to characterize and measure the microscope's PSF. This was done by diluting 100-nm Tetraspeck beads in ethanol, and drying a droplet of the solution on a #1.5 coverslip. The beads were imaged on the microscope in 3D by scanning the focal plane through the sample in steps of 50-100 nm. The beads were segmented out of the images by gradient based segmentation. Then beads with overlapping PSFs, and excessively large/bright beads were filtered out of the data. This was done because overlapping PSFs hinder Gaussian fitting because light coming from neighboring beads contaminates the signal. The remaining beads were fit with 3-dimensional Gaussian functions in order to model the PSF as Gaussian according this equation:

$$G(x,y,z) = A\ Exp\left[-\frac{(x-\mu x)^2}{(2\sigma_x)} - \frac{(y-\mu y)^2}{(2\sigma_y)} - \frac{(z-\mu z)^2}{(2\sigma_z)}\right] \qquad \text{Eq. 4.9}$$

I measured the beads both with the disc (confocal) and without the disc (epi), and took care to measure exactly the same field of beads each time. The image acquisitions were automated, and the laser was used at a low enough power that photobleaching did not contribute significantly to the results. I obtained bead measurements were for each pinhole size, and 3 different wavelengths (647 nm, 561 nm, 488 nm) and I compared the lateral and axial PSF sizes.

I observed the lateral and axial the sizes of the PSF follow the predicted trend: that bluer wavelengths produce smaller PSFs than redder wavelengths. This holds true for both the EPI and the disc PSFs. The effect of the disc can be observed by examining the PSF distributions with the disc in place. By inspection, one can see that the disc has a minimal effect on the size of the lateral PSF, however it has a significant effect on the size of the axial PSF. At the small pinhole limit (20 µm), the out of focus aberrations are blocked by the pinhole which gives notably smaller axial PSFs compared to epi measurements. As the pinhole gets larger, its effect becomes less apparent because it is no longer blocking light originating from outside the focal plane, and it approaches the limit where no disc is in place.

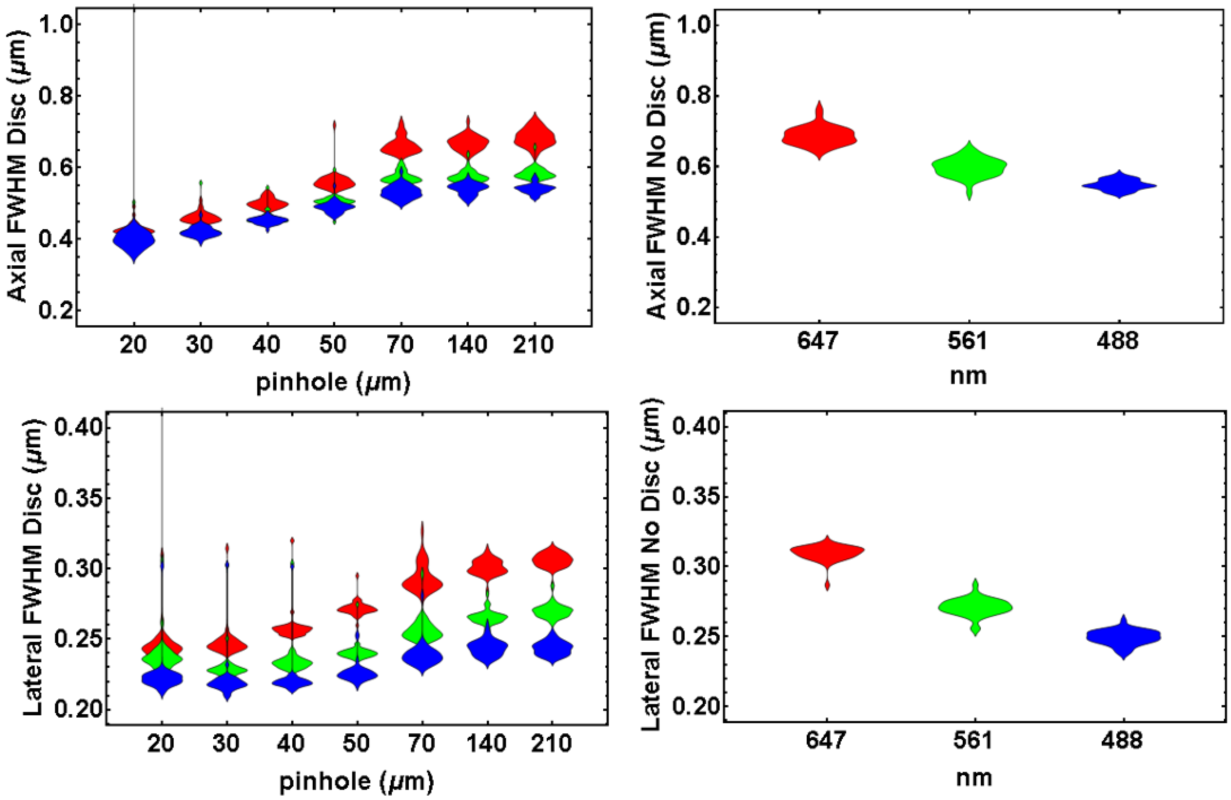

Figure 4.8 Size distribution of bead images with (left) and without the disc (right). The red, green and blue distributions represent the same field of beads imaged with a 647, 561 and 488 nm laser respectively. Once can observe the sizes of the PSFs with no disc (right) decrease as wavelength decreases both with and without the disc. Also, the effect of the pinhole is especially pronounced in the axial direction compared to the lateral direction.

4.3.6 *Future Outlook*

This disc is notable because of how inexpensively an existing microscope setup can be modified to include SDCM. Many epi fluorescence microscopes already utilize CCDs as detectors, and have a sufficiently powerful laser source that can be used for illumination. We have shown that by using a printed disc and hard drive enclosure, one can create a confocal spinning disc for about $1000 USD, with high quality PSFs. Furthermore, the printability and low price make it possible to customize the disc according to the user’s need which is not possible with commercial units.

The main drawback of the disc is its low transmission efficiency (1%-4%). This hinders imaging both on the detection and emission pathways, and reduces the frame rates one can operate at. Compared to commercial versions, the printable disc has a slow framerate, and is less suited for imaging fast cellular dynamics. Therefore, if an investigator desires blazing fast frame rates, I would recommend they purchase a commercial unit. However, if they desire to incorporate confocal imaging on a microscope which already has a laser and CCD this homemade disc is an ideal solution.

The homemade disc allows the researcher to easily exploit confocal optical sectioning to obtain 3D images, while minimally modifying their existing setup. Before now, previous options were either to buy an expensive commercial spinning disc unit, or to purchase scanning mirrors and a PMT to build a CLSM. It is my hope this disc design hits the sweet spot by appealing to researchers who want a versatile, inexpensive confocal imaging system that can operate at frame rates on par with CLSM.

4.4 REFERENCES

1. Ambrose, E.J. 1956. A Surface Contact Microscope for the study of Cell Movements. Nature. 178: 1194–1194.

2. Gustafsson, M.G. 2000. Surpassing the lateral resolution limit by a factor of two using structured illumination microscopy. J. Microsc. 198: 82–87.

3. Chen, B.-C., W.R. Legant, K. Wang, L. Shao, D.E. Milkie, M.W. Davidson, C. Janetopoulos, X.S. Wu, J.A. Hammer, Z. Liu, B.P. English, Y. Mimori-Kiyosue, D.P. Romero, A.T. Ritter, J. Lippincott-Schwartz, L. Fritz-Laylin, R.D. Mullins, D.M. Mitchell, J.N. Bembenek, A.-C. Reymann, R. Bohme, S.W. Grill, J.T. Wang, G. Seydoux, U.S. Tulu, D.P. Kiehart, and E. Betzig. 2014. Lattice light-sheet microscopy: Imaging molecules to embryos at high spatiotemporal resolution. Science. 346: 1257998–1257998.

4. McGorty, R., H. Liu, D. Kamiyama, Z. Dong, S. Guo, and B. Huang. 2015. Open-top selective plane illumination microscope for conventionally mounted specimens. Opt. Express, OE. 23: 16142–16153.

5. Stout, A.L., and D. Axelrod. 1989. Evanescent field excitation of fluorescence by epi-illumination microscopy. Applied optics. 28: 5237–5242.

6. Axelrod, D. 2001. Total internal reflection fluorescence microscopy in cell biology. Traffic. 2: 764–774.

7. Hao, R., Y. Fan, M.D. Howard, J.C. Vaughan, and B. Zhang. 2018. Imaging nanobubble nucleation and hydrogen spillover during electrocatalytic water splitting. Proceedings of the National Academy of Sciences. 115: 5878–5883.

8. Lu, J., Y. Fan, M.D. Howard, J.C. Vaughan, and B. Zhang. 2017. Single-Molecule Electrochemistry on a Porous Silica-Coated Electrode. Journal of the American Chemical Society. 139: 2964–2971.

9. Sheppard, C.J.R., and T. Wilson. 1981. The theory of the direct-view confocal microscope. Journal of Microscopy. 124: 107–117.

10. Cox, I.J., C.J.R. Sheppard, and T. Wilson. 1982. Improvement in resolution by nearly confocal microscopy. Applied Optics. 21: 778.

11. Minsky, M. 1988. Memoir on inventing the confocal scanning microscope. Scanning. 10: 128–138.

12. Sheppard, C.J.R. 1986. Scanned imagery. J. Phys. D: Appl. Phys. 19: 2077–2084.

13. Oreopoulos, J., R. Berman, and M. Browne. 2014. Spinning-disk confocal microscopy. In: Methods in Cell Biology. Elsevier. pp. 153–175.

14. McAllister, R.G., D.R. Sisan, and J.S. Urbach. 2008. Design and optimization of a high-speed, high-sensitivity, spinning disk confocal microscopy system. Journal of Biomedical Optics. 13: 054058.

15. Sandison, D.R., and W.W. Webb. 1994. Background rejection and signal-to-noise optimization in confocal and alternative fluorescence microscopes. Applied Optics. 33: 603.

16. Kimura, S., and T. Wilson. 1993. Effect of axial pinhole displacement in confocal microscopes. Applied Optics. 32: 2257.

17. Isozaki, K., K. Mikuriya, Y. c/o Y.E.C. Sugiyama, and T. Tanaami. 2005. Confocal microscope.

18. 2006. Handbook of biological confocal microscopy. 3rd ed. New York, NY: Springer.

19. McCabe, E.M., D.T. Fewer, A.C. Ottewill, S.J. Hewlett, and J. Hegarty. 1996. Direct-view microscopy: optical sectioning strength for finite-sized, multiple-pinhole arrays. Journal of Microscopy. 184: 95–105.

VITA

Marco Howard is an Ecuadorian immigrant, United States Air Force Veteran, and National Science Foundation Graduate Research Fellow. He moved to the United States when he turned 18 and his first job was working in strawberry fields in Ohio. Next, he joined the United States Air Force where he flew on board the world's most advanced reconnaissance platform (RC-135 V/W) as an intelligence analyst and cryptologic linguist. Finally he attended university and obtained a Bachelor's of Science in Chemistry from the University of Texas at Austin, and was awarded his PhD in Chemistry from the University of Washington. Marco currently resides in Seattle WA and enjoys hikes in the summer sun and cuddling with his cat MIDI on rainy days.